AquaContam: machine-learning models of drinking-water contamination learn who is monitored as much as where contamination occurs

Tyler J. Newton
Independent Researcher
ORCID: 0000-0002-1560-6553
Email: tyler.j.newton@gmail.com

Peer-review status statement

This manuscript is a non-peer-reviewed preprint submitted to EarthArXiv. It is being submitted to Nature Water for peer review.

Data and code availability

The compiled dataset and a code snapshot are archived on Zenodo at https://doi.org/10.5281/zenodo.22073200 (compiled data CC BY 4.0; code Apache-2.0). The source repository, including the deterministic verification gate that re-derives the benchmark artifacts from the frozen results archive, is at https://github.com/tjnewton/aquacontam.

AquaContam: machine-learning models of drinking-water contamination learn who is monitored as much as where contamination occurs

Tyler J. Newton (ORCID: 0000-0002-1560-6553)

Independent Researcher

Corresponding author: Tyler J. Newton (tyler.j.newton@gmail.com)

Abstract

Machine learning informs drinking-water monitoring, yet administrative data record the monitoring process as much as the contamination. Using AquaContam (over 4 million samples from 95,223 U.S. water systems and ambient monitoring locations), we find provenance proxies dominate feature attributions, and an apparent lead-model AUROC of 0.962 is largely a target-leakage artifact (corrected skill 0.699, 0.550 without provenance). A provenance-reduced PFAS signal survives (in-region AUROC 0.785) but transports modestly (AUROC 0.691, 95% CI 0.615–0.769), and spatial leakage separately inflates baseline-feature AUROC 0.699 → 0.869. Monitoring is itself inequitable: communities of color are sampled 1.85× more intensively (attenuated but significant under source adjustment), with heterogeneous detection burden (1.48, 95% CI 1.24–1.88; significant in 3 of 10 regions under a spatially-aware null), whereas low-income communities are under-sampled (0.78×). Although the group false-negative gap (0.50 versus 0.44) is not significant, the model is worse-calibrated for high-people-of-color systems (calibration error 0.18 versus 0.06). AquaContam provides a reproducible two-confound protocol with one converged detection task and documented boundary tasks.

Introduction

Drinking water contamination is a pervasive U.S. public health challenge. More than 200 million Americans are estimated to be served by systems with per- and polyfluoroalkyl substances (PFAS) at or above 1 ng/L (a modeled estimate predating UCMR5)[1]. Lead service lines (exemplified by the Flint, Michigan crisis[2]) deliver unsafe heavy-metal concentrations to millions of households[3]. PFAS exposure is linked to cancer, thyroid disease, and immune suppression[4,5], and chronic lead exposure causes irreversible neurodevelopmental damage[6]. In April 2024 the EPA established the first enforceable maximum contaminant levels for PFAS, five individual limits plus a Hazard Index for mixtures[7]. These limits intensify demand for predictive models that can prioritize monitoring resources across the nation's more than 150,000 public water systems[8].

Machine learning models are increasingly used to predict contamination risk from environmental and geospatial features, with results directly informing regulatory decisions. Spatial regression has linked PFAS detection to industrial sites, military fire training areas, and wastewater treatment plants[9]; gradient-boosted models predict PFAS in private wells from groundwater geochemistry[10]; and tree-based models on state drinking-water data report AUROC (the probability a model ranks a detected system above a non-detected one) >0.90 under random cross-validation[11]. PFAS occurrence in groundwater-sourced drinking water has been characterized across the eastern United States[12]. Extended Data Table 3 summarizes these and other prior ML approaches, none of which uses a geographic holdout. These studies share an under-examined property of their training data: contamination records are generated by an administrative monitoring process that decides which systems are sampled, how often, with what detection limits, and which results are reported. A model trained on such data can achieve

high apparent skill by learning the monitoring process (who is monitored) rather than the environmental drivers of where contamination occurs.

Two distinct confounds follow. First, random train-test splits allow geographically proximate systems to appear in both training and test sets: a form of spatial leakage, documented in ecology and species distribution modeling[13,14,15,16,17,18], in which nearby systems share confounders (land use, aquifer type, industrial proximity) that inflate apparent generalization. Second, ascertainment confounding: monitoring intensity, detection limits, reporting practices, and data-source provenance differ systematically across systems, and these signatures predict recorded detection outcomes without any environmental information. This confound is long recognized as sample-selection bias in presence-only species-distribution modeling[19,20] and as surveillance bias in epidemiology[21]. We translate this known confound to administratively generated drinking-water data rather than claim it as new. Published performance estimates inform EPA monitoring prioritization and state regulatory decisions; estimates inflated by either confound will fail precisely where the models are most needed: in unmonitored or newly monitored systems and regions. Despite this risk, no standardized benchmark enforces evaluation that controls for either confound. Domain-specific ML benchmarks (GEO-Bench[22] for Earth observation, SustainBench[23] for sustainability, ClimateBench[24] for climate science) have accelerated progress in their respective fields. No equivalent exists for water quality, where extreme class imbalance (97% censoring), spatial autocorrelation, and left-censored measurements (concentrations known only to lie below a laboratory reporting limit) create unique challenges.

Here we introduce AquaContam, an open benchmark that addresses this gap. By integrating fifteen federal and state data sources into over 4 million water quality samples from 95,223 systems (87,450 geocoded) and enforcing geographic stratification by EPA region, we demonstrate four things.

First, two compounding confounds inflate reported skill. Spatial leakage raises AUPRC by up to 58% (0.723 vs. 0.457 for logistic regression with the full feature set; 40% for the benchmark gradient-boosted configuration). Ascertainment signatures account for part of the remainder on monitoring-sensitive tasks (corrected lead action-level AUROC 0.699 → 0.550 without provenance features, after a target-leakage artifact inflating the apparent skill to 0.962 is removed). Second, models learn the monitoring process: data-source provenance proxies dominate SHAP attributions, and a monitoring-invariant predictor quantifies the genuinely environmental signal (out-of-region AUROC 0.691, 95% block-bootstrap CI 0.615–0.769, for the provenance-reduced model).

Third, monitoring effort is itself inequitably allocated across demographic lines (systems serving communities of color sampled 1.85-fold more intensively, attenuating under data-source adjustment; low-income systems sampled less), so differential ascertainment biases both contamination estimates and the equity conclusions drawn from them (national detection-burden ratio 1.48, regional maximum 2.57). Fourth, seven benchmark tasks, 20 model families (29 model classes), reproducible pipelines, and a public leaderboard provide a reproducible evaluation protocol and task suite for water contamination prediction. Unlike prior bespoke single-source water-quality models, AquaContam standardizes the tasks, retains censoring-aware targets, and adds a two-confound evaluation protocol.

Substantive evidence is concentrated in the detection task (T1); several models do not converge on the sparser transfer and multilabel tasks (T3/T5/T7), which we report with explicit non-convergence annotations rather than as a populated leaderboard. No new learning method is introduced: the advance is the rigorous quantification and decomposition of these confounds,

the monitoring-inequity finding, and the reproducibility apparatus, at a moment of acute regulatory relevance.

Results

National-scale data integration (Fig. 1, Table 1)

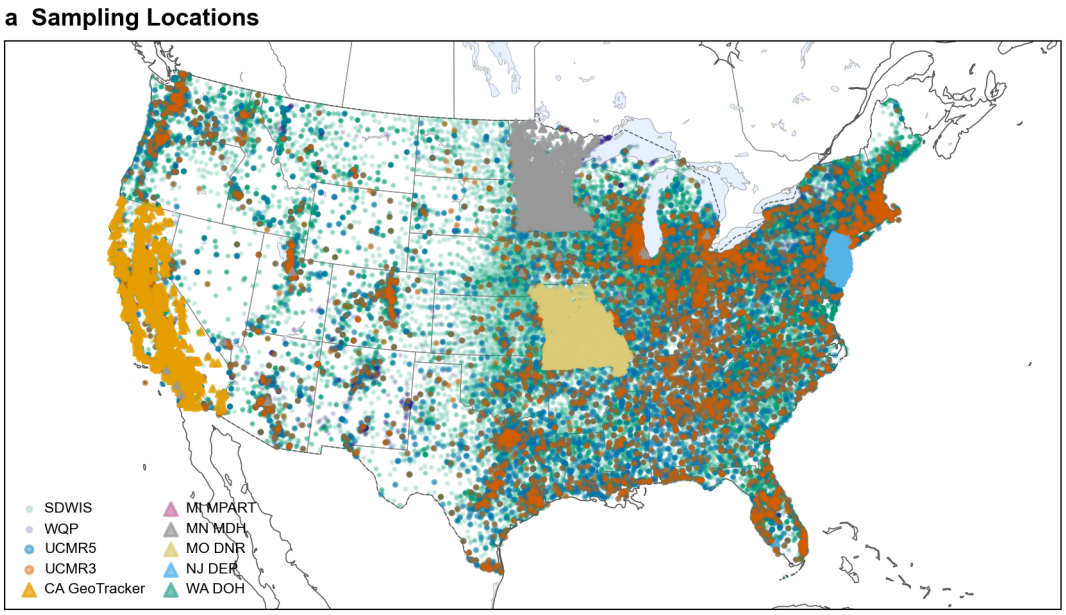

Fig. 1: National-scale data integration

Table 1

Source	Records	Analytes	Period	Censoring Rate	Status
UCMR5	1,928,117	29 PFAS + Li	2023	97.1%	Available
UCMR3	1,069,174	6 PFAS + 32	2013-2015	76.4%	Available
SDWIS	916,899	Pb/Cu	2016-2022	0.3%§	Available
MI MPART	5,640	5 PFAS	2019-2023	0%†	Available
CA GeoTrackerǁ	324,254	29 PFAS	2019-2023	83.1%	Available
OH EPA	26,554	6 PFAS	2020-2024	0%†	Excluded‡
WA DOH	9,251	14 PFAS	2023-2024	0%†	Available
NJ DEP	248,107	25 PFAS	2019-2023	~80%	Available

Source	Records	Analytes	Period	Censoring Rate	Status
NC DEQ	1,953	5 PFAS	2020-2023	~80%	Unavailable
WQP‖	35,528	13 PFAS	2020-2024	~39%	Available
MO DNR	75,971	29 PFAS	2020-2023	~99%	Available
MN MDH	247,230	27 PFAS	2005-2026	~92%	Available
NJ Private Wells*	~10K	PFAS + metals	2020-2023	~75%	Unavailable
EJScreen*	~220K	Demographics	2023	N/A	Available (GDB)

*Auxiliary source: provides private-well measurements (NJ Private Wells) or demographic covariates (EJScreen) rather than public-water-system compliance monitoring; not part of the primary benchmark population count. †Detection-only reporting: source data includes only detected samples; non-detects are not available. §SDWIS reports Lead and Copper Rule 90th-percentile compliance values, which are genuine quantitative measurements that are only rarely left-censored; the 0% censoring reflects this measurement mechanism, not detection-only reporting. ‡Excluded from analysis: zero unique PWSIDs after deduplication with national sources. ‖Ambient environmental monitoring (groundwater/surface water), a different population from public-water-system finished water; reserved for external validation, not included in the main benchmark train/validation/test splits.

AquaContam integrates fifteen federal and state data sources (thirteen contributing data, one excluded, one unavailable) into a harmonized water quality dataset. All are public records; all but Minnesota MDH are directly downloadable, Minnesota being obtained by written request under the state records act and redistributed only with the agency's permission (Data Availability). The two primary federal sources, UCMR5 (2023) and UCMR3 (2013–2015), contribute 1,928,117 and 1,069,174 analytical records respectively, covering 30 PFAS/lithium analytes and 38 contaminants including 6 PFAS. SDWIS[25] adds lead and copper compliance monitoring (916,899 records).

Six state databases (Michigan, California, Washington, Missouri, New Jersey, Minnesota) and the USGS/EPA Water Quality Portal (35,528 PFAS records across 49 CONUS states) provide complementary regional coverage; Ohio EPA (26,554 records) was excluded because its PWSIDs overlap SDWIS and it reports only detected samples. Minnesota MDH (Table 1) adds a dense state compliance program to the in-split public-water-system population. It spans the 3M east-metro contamination plume, among the most intensively monitored PFAS landscapes in the country, and supplies authoritative detection labels for the many Minnesota systems that federal monitoring cycles sample only sparsely. Under leave-region-5-out cross-validation, where the model trains on no Minnesota system, it predicts Minnesota detection at AUROC 0.797 (AUPRC 0.256), generalizing to this monitoring-confounded landscape without overfitting the plume. The paper's central claims, the monitoring-confound decomposition and the inequity analysis, rest on the federal UCMR and SDWIS records and do not depend on Minnesota. The

Minnesota MDH data serve as a dense-monitoring corroboration, so the thesis stands if that source cannot be redistributed.

All sources are harmonized to a common schema with standardized identifiers, units in micrograms per liter, and left-censored non-detects retained with explicit flags, critical given that 97.1% of UCMR5 samples fall below detection limits. ZIP-code geocoding via Census ZCTA centroids[26] places 87,450 systems for geospatial feature extraction (Extended Data Fig. 1), robust to geocoding imprecision (5-km noise: ΔAUROC −0.007; Supplementary S7b).

Predictions transfer across data sources. Cross-source validation on two independent state databases within validation-region geography confirms this: NJ DEP (Region 2, AUROC 0.789, n = 1,310) and MO DNR (Region 7, AUROC 0.829, n = 1,208) (Extended Data Table 5). These databases share regional geography with training data but use independent sampling and reporting pipelines, testing data-source generalization rather than geographic generalization. The only geographically external test, CA GeoTracker (Region 9, test partition, AUROC 0.813, n = 1,421), monitors groundwater sites rather than public water systems; on this larger sample the model now performs above chance (DeLong $p < 0.001$). Its monitoring domain differs structurally from the public water systems the benchmark targets, so geographic generalization to unseen regions with structurally different monitoring domains remains undemonstrated. The remaining state databases preclude AUROC computation in our modeling set: MI MPART and WA DOH are effectively single-class (near-complete detection after coordinate backfill and aggregation), while NC DEQ and OH EPA lack usable in-split data.

Two compounding confounds inflate reported skill (Fig. 2, Extended Data Table 4)

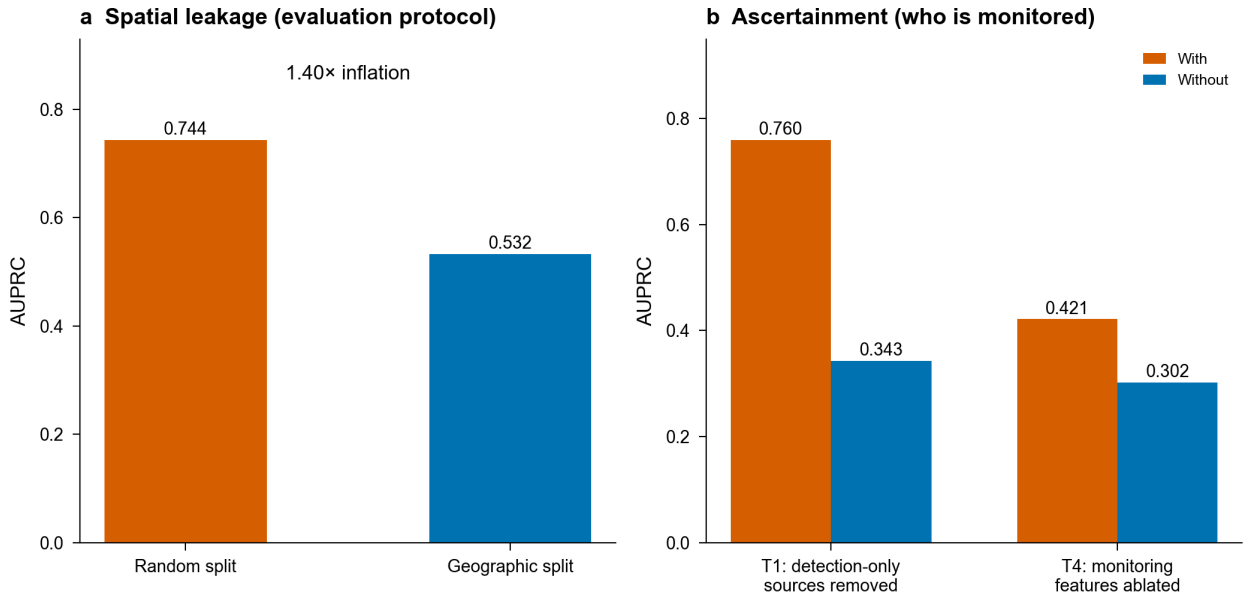

Fig. 2: Two compounding confounds inflate reported skill

The first confound is spatial leakage. A controlled 3-model × 3-feature-set comparison (14,405 systems) reveals AUPRC inflation of up to 58% under random versus geographic splitting (Extended Data Table 4). The largest inflation occurs for logistic regression with the full feature set (0.723 random vs. 0.457 geographic, 58%); the benchmark XGBoost configuration on the baseline feature set inflates by 40% (0.744 vs. 0.532). The inflation is not a training-set-size artifact: a size-matched control (random cross-validation with each fold's training set subsampled to the geographic training-set size) preserves comparable inflation across the same cells (Supplementary Table 1). The inflation arises because geospatially proximate systems

share confounders (land use, aquifer type, industrial proximity) that models exploit under random splitting; Moran's I analysis confirms significant spatial autocorrelation in model residuals ($I > 0$, $p < 0.01$; Supplementary S9). On a baseline proximity/demographic feature set representative of prior feature-based prediction studies[9,10,11], XGBoost drops from AUPRC 0.744 (random) to 0.532 (geographic; Fig. 2a). Leave-one-region-out (LORO) cross-validation, which trains on nine EPA regions and tests on the tenth in turn, yields mean AUROC 0.782 (s.d. 0.102) across 10 EPA regions, confirming that geographic heterogeneity rather than a single split choice drives this pattern.

The second confound is ascertainment: the monitoring process leaves signatures (which source reported a system, how often it was sampled, at what detection limits) that predict recorded detection outcomes without environmental information. Excluding systems observed only through detection-only data sources (n = 256) lowers T1 XGBoost AUPRC from 0.760 to 0.343, and the prevalence-independent AUROC also falls (0.838 to 0.714; Fig. 2b, Supplementary S21). On T4, ablating monitoring-intensity features lowers lead action-level AUPRC from 0.421 to 0.302 (ΔAUPRC = −0.119, $p_{FDR} < 0.001$; Fig. 2b, Extended Data Table 1), once a target-leakage artifact that had inflated the T4 baseline to 0.902 is removed (see T4 below). The two confounds compound: spatial leakage inflates the evaluation, ascertainment inflates what the model can learn. The sections below decompose how much skill survives once both are removed.

Benchmark performance under geographic evaluation (Table 2, Extended Data Fig. 5)

Table 2

Model	LORO AUROC (mean, 95% CI)	Fixed-split AUROC (95% CI)	LORO folds
CatBoost	0.790 [0.717-0.862]	0.845 [0.823-0.867]	10/10
Voting	0.784 [0.707-0.861]	0.850 [0.828-0.871]	10/10
XGBoost	0.782 [0.706-0.859]	0.864 [0.842-0.885]	10/10
Random Forest	0.771 [0.693-0.848]	0.850 [0.828-0.872]	10/10
LightGBM	0.766 [0.684-0.848]	0.847 [0.825-0.868]	10/10
TabPFN	0.758 [0.678-0.838]	0.856 [0.835-0.879]	10/10
ICP	0.713 [0.623-0.804]	0.731 [0.703-0.761]	10/10
Stacking	0.711 [0.585-0.837]	0.849 [0.828-0.871]	10/10
Deep Tobit	0.707 [0.611-0.802]	0.602 [0.574-0.629]	10/10
Logistic Reg.	0.705 [0.607-0.802]	0.753 [0.725-0.781]	10/10
MLP	0.704 [0.608-0.800]	0.716 [0.687-0.748]	10/10
GCN (linear fallback)	0.683 [0.594-0.772]	0.642 [0.615-0.669]	10/10
CNN1D	0.670 [0.561-0.779]	0.787 [0.762-0.812]	10/10
GraphSAGE (linear fallback)	0.652 [0.559-0.745]	0.482 [0.456-0.505]	10/10

Under geographically stratified evaluation, AquaContam defines seven benchmark tasks across 20 model families (Table 2 ranks the converged T1 detection task by its primary, leakage-resistant protocol; complete multi-task results in Supplementary Table 9). These are the numbers a careful study would report after controlling the first confound (spatial leakage) but not the second (ascertainment); the sections below show how much of this skill the monitoring process accounts for.

T1: PFAS binary detection. Under the leakage-resistant LORO protocol by which Table 2 ranks the families, the tree and ensemble models cluster tightly at a mean AUROC of 0.782 (CatBoost 0.790; XGBoost 0.782), and the transportable, provenance-reduced signal is more modest still (out-of-region AUROC 0.691). On the single fixed West-only split, XGBoost attains a higher test AUROC of 0.864 (seed 42, with a 5-seed mean of 0.864 ± 0.003 on the same headline harness) and the primary metric AUPRC (0.781), with LightGBM and Random Forest close behind. That split's test set contains region 10, the highest-prevalence (detection rate 0.433) and most separable (held-out AUROC 0.971) region, so 0.864 is the optimistic upper end of the paper's T1 estimates rather than the deployment-relevant figure. DeLong tests with FDR correction confirm that the top models significantly outperform most individual models, though differences among the top tree models are not significant, consistent with the broader finding that tree-based models still outperform deep learning on tabular data[27,28]. The headline is seed-stable: the five-seed spread on its own harness is a few thousandths of a point, so it is not a favorable-seed artifact. Several T1 AUROC figures recur in this paper. They come from different harnesses, meaning different combinations of feature set, system population, and splitting protocol, and are not conflicting estimates of one quantity (Methods, Supplementary S11).

The single geographic split is one draw, and its i.i.d. bootstrap confidence intervals are anti-conservative under the residual spatial autocorrelation documented in the Supplementary Information. Table 2 ranks the T1 families by their leave-one-region-out (LORO) mean AUROC across the ten EPA regions, the leakage-resistant protocol, and shows the fixed West-only geographic split alongside as a transparent secondary comparison. The ranking flips under LORO: CatBoost leads at 0.790, followed by the voting ensemble at 0.784, while the fixed-split leader XGBoost falls to third (0.782). The top tree and ensemble families are statistically comparable at the top (the benchmark is underpowered to separate the leading two, Supplementary S19), so the benchmark's value is the honest, reproducible protocol rather than a single winner: tree ensembles are the strong baseline to beat.

All fourteen families ran the full leave-one-region-out protocol. The two graph networks sit at the bottom because the geographic split leaves their test regions with no graph edges to training nodes, so no message passes between them and their inductive inference reduces to node-wise linear transforms. TabPFN ran under its 3,000-sample stratified subsample on every fold. Table 2 reports default-configuration seed-42 results for reproducibility.

T4: Heavy metal prediction (a target-leakage cautionary case). Lead action-level exceedance appeared to yield the strongest nominal performance of any task (tree models reaching AUROC 0.962), but this was almost entirely an artifact of target leakage. For SDWIS, the sole T4 source, the Lead and Copper Rule reports 90th-percentile compliance results that are essentially never left-censored, so the per-system mean reporting limit equals the mean measured lead concentration; filed among the monitoring-intensity features, it leaked the action-level target (Methods). Recomputing the reporting limit as missing for detected samples and re-running T4 reduces XGBoost to AUROC 0.699 (95% CI: 0.690–0.708) with AUPRC 0.387. Of the skill that remains, monitoring intensity still contributes: ablating it lowers AUPRC from 0.421 to 0.302 (ΔAUPRC = −0.119, $p_{FDR} < 0.001$; Fig. 2b, Extended Data Table 1), the provenance-reduced model reaches AUROC 0.550 (Table 3), and the monitoring-invariant ICP model 0.587. Lead sampling intensity is, however, only partly a confound: under the Lead and Copper Rule,

systems that exceed the action level must sample more sites on stricter schedules (40 CFR 141.86), so sample count is mechanistically coupled to genuine elevated risk as well as to ascertainment. T4 thus illustrates two hazards of administrative water-quality records, target leakage and ascertainment confounding, rather than geographic generalization.

Table 3

Approach	Task	AUROC	AUPRC	Notes
Full model (XGBoost)	T1	0.864	0.781	All features
Full model (XGBoost)	T4	0.699	0.387	All features
Provenance-free (XGBoost)	T1	0.785	0.698	Provenance features dropped (environment-only)
Provenance-free (XGBoost)	T4	0.55	0.244	Provenance features dropped (environment-only)
ICP	T1	0.731	0.672	Adversarially invariant
ICP	T4	0.587	0.270	Adversarially invariant
DML adjusted	T1	0.729	—	Post-hoc adjusted association

T2: Concentration regression (negative result). All models yield R^2 near or below zero on the linear concentration scale, including censoring-aware architectures (Tobit, AFT, Hurdle; Supplementary S25). We interpret this cautiously: on a heavily right-skewed, mostly censored target the linear-scale R^2 is a demanding metric, and rank-based concordance is likewise weak (Hurdle concordance near chance). Within the limits of these features and scales, system-level geospatial features show little ability to predict PFAS concentration magnitude given detection. Concentration variability is likely governed by within-system factors (wellhead depth, treatment technology, source water hydrochemistry) absent from the feature set. T2 documents a prediction boundary rather than an open challenge: resolving it requires fundamentally different data, not better models.

Other tasks. Multi-PFAS profiling (T3) achieves micro-AUROC 0.765, cross-contaminant transfer (T5) AUROC 0.715 (monitoring-mediated; Supplementary Fig. 1), and temporal prediction (T7) AUROC 0.664 with significant feature distribution shifts between UCMR3 and UCMR5 eras (Supplementary S24).

Feature importance and adjusted association analysis (Fig. 3, Extended Data Fig. 2, Extended Data Table 1)

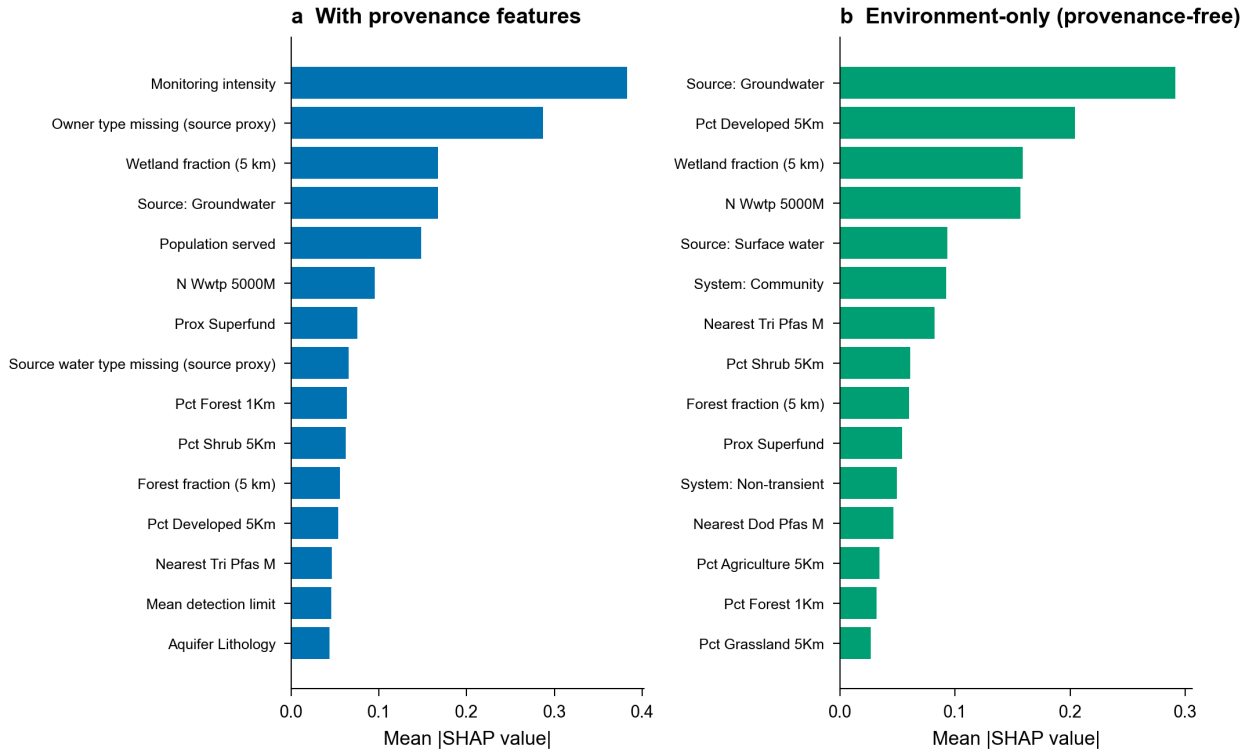

Fig. 3: Models learn the monitoring process (SHAP)

SHAP analysis[29] of the T1 XGBoost model shows directly that the model learns the monitoring process (Fig. 3a). The two highest-magnitude features are monitoring proxies: the number of samples per system, a monitoring-intensity measure (mean |SHAP| = 0.383), and the owner-type missingness indicator, which encodes which database reported a system, a data-source provenance proxy (0.287). Environmental and source-water features follow (wetland fraction, ground-water source type, population served), and the mean detection limit contributes only 0.045. When the ten provenance and monitoring features are removed, attributions shift to substantive predictors: system type, source water type, wetland fraction, land use, and aquifer lithology (Fig. 3b); these are the environmental drivers the field intends these models to learn. Drop-one-category ablation with train-only imputation and paired bootstrap testing (n = 1,000; Benjamini-Hochberg FDR correction across categories) confirms a task-dependent monitoring dependence pattern: removing monitoring-intensity features reduces AUPRC on both tasks, with a substantially larger and more robust effect for T4 (Fig. 2b, Extended Data Table 1) that persists even after the leakage artifact is removed. The strongest evidence of T1 ascertainment is therefore the removal of detection-only sources (AUPRC 0.760 → 0.343) and the provenance-reduced LORO drop (below), not feature ablation. Among environmental features, proximity to Superfund sites and WWTP count rank highest, consistent with known PFAS sources[30].

To separate confounded from adjusted associations, we apply double machine learning (DML)[31] with standardized (per 1-s.d.) coefficients to the T1 feature set. DML re-estimates each feature's association with detection after using machine learning to residualize out the monitoring and system-size confounders. Adjusted AUROC drops from 0.835 to 0.729, indicating that a substantial share of discrimination arises from feature confounding.

The aggregate rank correlation between DML and SHAP orderings is modest but significant (Spearman ρ = 0.24, p = 0.032, over the n = 80 features ranked in both orderings; DML coefficients are estimated for all 130 features), and a grouped permutation test finds no feature category with significantly larger mean rank displacement than chance (Supplementary S14). Individual features nonetheless reorder substantially: 69 of 130 FDR-corrected coefficients are significant (p_FDR < 0.05), of which 3 carry no evidential weight: residualizing out the monitoring confounders leaves them almost no variation, so their adjusted associations are not identified under the overlap assumption (Supplementary S14). The largest displacements are environmental rather than demographic.

Among demographics the adjustment moves the two flagged groups in opposite directions. pct_people_of_color is the most-upranked demographic (from SHAP rank 51 to DML rank 12) and retains a significant adjusted association (standardized effect +0.022, p_FDR < 0.001) that is robust through Rosenbaum Γ = 3.0. pct_low_income attenuates and no longer carries a significant adjusted association (p_FDR = 0.54), consistent with its apparent correlational signal being largely monitoring-mediated. We read this as absence of evidence, not evidence of absence. The coefficient is also the most fragile in the sensitivity analysis, tipping at Rosenbaum Γ* = 1.0, where Γ indexes how strong an unmeasured confounder would have to be to overturn a result. It concerns the detection *model's* feature attribution, not the population-level contamination disparity, which is separately estimated by the burden ratio below and is robust to monitoring-propensity adjustment. Industrial-proximity features and Superfund proximity retain the strongest adjusted associations (industrial facility counts and prox_superfund, p_FDR < 0.001), with airport, landfill, and WWTP distances also significant (p_FDR < 0.05), supporting mechanistic relevance (Extended Data Fig. 4, Supplementary Table 3).

These DML estimates are adjusted associations, not causal effects, and are substantively fragile. 54 of 130 coefficients remain significant through Γ = 3.0 on a Rosenbaum-style sensitivity index, a large-sample effect. That index is an adaptation computed on the regression scale without a matched design, so it is a heuristic robustness screen rather than the original bounded test (Methods and S20). All E-values are nonetheless uniformly small, so a weak unmeasured confounder could explain individual point estimates, and pct_low_income is the most fragile, tipping at Γ* = 1.0 (Supplementary Table 16, S20).

A third route penalizes the model during training for encoding who did the monitoring. Our Invariant Contamination Predictor (ICP) keeps all features but is trained so that a competing adversary network cannot recover the monitoring confounders from its internal representation; the adversary's gradients are reversed, so the encoder is pushed to hide exactly what the adversary seeks (Extended Data Fig. 4, Supplementary Table 13). We name it by analogy to invariance-based learning; it is distinct from the Invariant Causal Prediction framework[32]. Trained to convergence, the ICP attains T1 AUROC 0.731, about five points below the 0.785 of provenance-feature dropping (Table 3), a deliberate accuracy cost paid for monitoring invariance. The invariance is substantial but partial: a held-out probe recovers data-source provenance from the ICP representation at only AUROC 0.64, below the 0.79 obtainable from the raw features (Supplementary S17). The representation therefore carries less monitoring information than the inputs themselves, even though those inputs remain entangled with retained features such as population served or system type (adversarial, not a formal guarantee). Feature ablation removes monitoring signal by discarding features; DML adjusts post-hoc; ICP penalizes it at the representation level (Supplementary S17).

The monitoring-invariant environmental signal is modest (Table 3)

Table 3 decomposes how much predictive skill survives when monitoring information is removed, by three complementary routes. Under the geographic holdout, dropping the ten provenance and monitoring features costs T1 XGBoost about seven points of AUROC (0.864 →

0.785) and also lowers the primary metric AUPRC (0.781 → 0.698). The same removal reduces the corrected T4 model much further, from 0.699 to 0.550 (its apparent 0.962 was a target-leakage artifact). The contrast quantifies how differently the two tasks depend on the monitoring process. The representation-level ICP attains T1 AUROC 0.731 (adversarially suppressing the targeted monitoring-intensity confounders; the recoverability probe in Supplementary S17 confirms the representation hides data-source provenance, 0.64 vs 0.79 from raw features), and post-hoc DML adjustment yields 0.729. The decisive test is out-of-region transport. Under LORO cross-validation, and using the same system-count-weighted estimator for both models, the with-provenance T1 model transports at AUROC 0.785 (unweighted fold mean 0.782; 95% region-block-bootstrap CI 0.705–0.860) and the provenance-reduced model at 0.691 (95% region-block CI 0.615–0.769). The two intervals overlap, so the with-versus-without transport difference is not itself significant at the region level.

These region-block-bootstrap intervals resample only ten EPA-region clusters and are anti-conservative. The honest cluster-robust t(9) recalibration (Supplementary S17) widens the provenance-reduced interval to 0.606–0.783, which still excludes chance, so we read the interval as indicative. Because the provenance-reduced feature set retains a small documented re-encoding channel (Supplementary S17), we read 0.691 as an upper-bound estimate of the transportable environmental signal. The monitoring-invariant ICP gives a comparable out-of-region estimate (leave-one-region-out AUROC 0.713, close to its 0.731 in-region value), so the two honest estimators broadly agree rather than one being decisively stricter.

This mean conceals wide regional variation. The provenance-reduced model is weak in the held-out regions where it is most challenged (AUROC as low as 0.57, only marginally above chance though formally significant given the large per-region samples), yet it reaches up to 0.96 in the strongest region (Supplementary S9). The transportable signal is therefore real on average but not uniformly available. For T4, once the target-leakage artifact is removed, the out-of-region contrast is modest: 0.676 ± 0.041 with provenance versus 0.543 without, far below the leakage-inflated value the uncorrected model had reported. Physically this is the expected outcome: lead and copper action-level exceedances arise largely from corrosion control and premise plumbing rather than source-water quality, so near-chance skill from source-water environmental features is anticipated on mechanistic grounds.

Modest discrimination can still carry deployment value. The monitoring-free T1 model concentrates 3.0-fold more detections in its top risk decile than the test-set prevalence (Supplementary Table 10). The prioritization also survives the out-of-region deployment scenario: scoring every system with the LORO model that held out its region yields a pooled out-of-fold top-decile lift of 2.97 (system-count-weighted within-region lift 2.72; frozen loro_lift.json). That is enough to usefully prioritize monitoring within the monitored population, provided that its limits, including the near-chance regions above, are stated honestly. These lift figures score the detection target; the regulatorily-actionable target is MCL exceedance, which is harder to predict. On a matched fixed-split harness the exceedance model reaches AUROC 0.719 and AUPRC 0.515 and concentrates 2.68-fold more exceedances in its top decile, versus AUROC 0.807 and a 3.06-fold lift for detection, a nine-point AUROC gap (frozen mcl_lift.json), so detection-based scores are a weaker but still useful proxy for exceedance risk.

Inequitable monitoring is an environmental justice issue (Fig. 4, Extended Data Table 2)

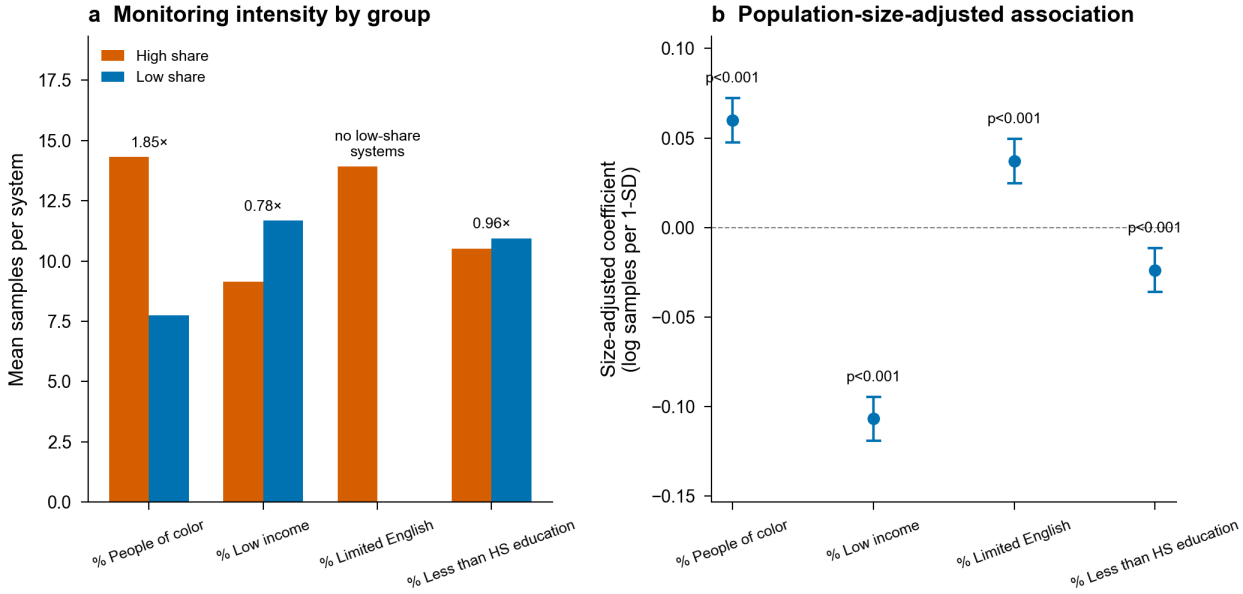

Fig. 4: Inequitable monitoring

Nationally, the PFAS detection burden along the percent-people-of-color dimension is 1.48 (95% block-bootstrap CI 1.24–1.88; system-count-weighted mean across all 10 EPA regions). That national mean conceals substantial regional variation: the western test region yields 1.34 (n_high = 437, n_ref = 1,080) and the regional maximum is 2.57 (region 7), itself marginally FDR-significant (p_FDR ≈ 0.05; Supplementary Table 20). Because multiple-comparison control is applied within each demographic family but not across the per-region maxima, this single-region extremum is exploratory.

How many regions reach significance depends on the null distribution used. 5 of 10 regions are FDR-significant under a label-shuffle null but 3 under a spatially-aware rotation null on a common assembly, so the naive per-region test is mildly anti-conservative. The national people-of-color monitoring-intensity disparity itself remains significant under a stratified-by-region permutation ($p < 0.001$, Supplementary S14). The test-set high-versus-low contrast is also robust to the cutpoint choice: re-deriving the people-of-color burden ratio under a symmetric median split and an interquartile split spans 1.72–1.91 around the published 80th-versus-50th estimate, with the direction unchanged in every scheme (frozen cutpoint_sensitivity.json).

Adjusting for who gets monitored does not eliminate the disparity. Across the geographic test set, inverse-propensity weighting (IPW) attenuates the people-of-color burden from 1.88 to 1.62 (still significant, $p < 0.001$). That adjustment covers observed monitoring confounders; it does not necessarily account for unobserved selection under the missing-not-at-random (MNAR) assumption (Methods). The disparity is also stable to the spatial scale of demographic attribution: population-weighted areal apportionment over all block groups within a service-area buffer of each system leaves it qualitatively unchanged (1.88 single-nearest versus 1.69 and 1.59 at 5-km and 10-km buffers; Supplementary Table 26), so the single-block-group attribution does not drive the result. Disparity direction is region-dependent: income and education burden ratios are elevated in the west but sit near parity nationally, a pattern single-region analyses miss. In the geographically held-out test set the per-group discrimination is similar across groups (per-group AUROC 0.799 vs 0.750 for high versus low share; Extended Data Table 2). This equity analysis excludes the 692 test systems (18.3% of the test set) whose demographics

could not be attributed; the model is unusually accurate on that group (AUROC 0.984), consistent with those being better-recorded systems, so excluding them is conservative for the disparity estimates. The deployment-relevant error profile still disfavors high-people-of-color systems: at the operating threshold the model leaves more contaminated high-share systems unflagged (false-negative rate 0.50 vs 0.44) and is more poorly calibrated for them (expected calibration error 0.18 vs 0.06; Supplementary Table 25).

These gaps must be read against markedly different group base rates (detection prevalence 0.36 versus 0.19). When base rates differ, no single operating threshold can equalize error rates and calibration at the same time[33,34]. Part of the gap therefore reflects that impossibility rather than remediable model bias alone. It remains a fairness concern specific to this dimension and region that warrants deployment caution, consistent with longstanding environmental justice concerns[35,36] and with documented sociodemographic disparities in PFAS exposure and pollution burden[37,38,39] and in public drinking-water arsenic and uranium[40].

The monitoring process is itself inequitably allocated (Fig. 4). Among monitored systems, those serving high shares of people of color are sampled 1.85-fold more intensively than low-share systems (14.3 vs 7.7 samples per system, permutation $p < 0.001$), and the association persists after adjusting for system size (+0.060 log-samples per 1-s.d., $p < 0.001$). Low-income communities are under-sampled (0.78-fold) while low-education sampling is near parity (0.96-fold), with size-adjusted coefficients (−0.107 and −0.024 per 1-s.d.). Surveillance is thus unevenly distributed along multiple demographic axes simultaneously, and in opposite directions; because recorded detections scale with sampling effort, this differential ascertainment biases both contamination estimates and the equity conclusions drawn from them. Monitoring allocation, not only contamination, is an environmental justice outcome.

Generality beyond PFAS and deployment under honest uncertainty

The confound decomposition generalizes beyond PFAS. On a geogenic contaminant, arsenic in the USGS National Groundwater Aggregation, geographic stratification reduces exceedance AUROC by up to 0.25 relative to random splitting (0.86 vs 0.61, random forest). Zero-shot transfer from public-supply to domestic wells (AUROC up to 0.72) matches the in-distribution geographic holdout for every model (Supplementary Table 24). For the 43 million Americans on unmonitored domestic wells, cross-region generalization is therefore the limiting factor.

For deployment, the trained models generate national PFOS and lead risk surfaces with conformal prediction sets, which are built to contain the true outcome a specified fraction of the time. Their observed marginal conformal coverage is 0.910 at $\alpha = 0.05$, modestly below the nominal target and reported as observed coverage rather than a delivered guarantee (Supplementary S6).

Discussion

The dominant learnable signal in U.S. drinking-water contamination records is the monitoring process itself. Two compounding confounds produce this. The first is spatial leakage in evaluation (AUPRC inflation of up to 58% under random splitting, persisting under a size-matched control; Extended Data Table 4). The second is ascertainment in the data-generating process (detection-only sources, monitoring intensity, and data-source provenance collapse T1 AUPRC from 0.760 to 0.343 and T4 from 0.421 to 0.302 when removed, the apparent 0.902 T4 baseline having been a target-leakage artifact).

The decomposition in Table 3 separates the two: controlling geography but not ascertainment yields T1 AUROC 0.864; additionally removing provenance yields 0.785 in-region but only 0.691 (95% CI 0.615–0.769) out-of-region, the upper-bound estimate of the transportable environmental signal. That figure sits well below both prior reports of >0.90 under random cross-

validation and our own with-provenance LORO mean of 0.782 (95% CI 0.705–0.860). This reframes spatial leakage findings from ecology[13]: in administratively generated environmental data, honest evaluation must control not only where the test systems are, but who chose to monitor them. Spatial cross-validation can be conservative for probability-sample designs[41], but the monitoring process here is precisely the non-random design we diagnose, so leakage-aware evaluation remains appropriate.

These results are constructive, not merely cautionary. The benchmark supplies the tools to evaluate honestly: geographic stratification, provenance-reduced feature sets, a monitoring-invariant model, and verification of every reported number against archived results. Modest discrimination retains policy value: the monitoring-free model concentrates 3.0-fold more detections in its top risk decile than in-sample prevalence (Supplementary Table 10), enough to prioritize monitoring under honest uncertainty, with marginal conformal coverage of 91.0% at $\alpha = 0.05$ (per-region coverage varies and per-region guarantees are not claimed; Extended Data Fig. 3, Supplementary S6). This value is regionally non-uniform: the out-of-region signal is near-chance in several EPA regions (per-region provenance-reduced AUROC as low as 0.57), so a deployer cannot assume uniform utility. We claim no predictive or deployment advance over existing practice: the contribution is diagnostic and methodological, quantifying and controlling two confounds and surfacing the monitoring-inequity finding, not a better contamination predictor.

For deployment to unmonitored systems we recommend the ICP when the feature set entangles monitoring with population or system-type variables. It trades about five AUROC points for substantial though partial monitoring invariance (0.731 vs 0.785 in-region), with a held-out probe recovering data-source provenance from its representation at only 0.64, below the 0.79 obtainable from raw features (Supplementary S17).

The group error profile warrants care rather than alarm. High-people-of-color systems in fact have somewhat higher discrimination (per-group AUROC 0.799 vs 0.750, gap $p = 0.060$) and better conformal coverage (0.919 vs 0.886, gap $p = 0.007$ in their favor) than low-share systems, and their elevated single-threshold false-negative rate (0.50 vs 0.44) is not individually significant ($p = 0.16$).

Two caveats keep this from being reassuring. First, the one group disparity that is both robust and unfavorable is calibration: high-people-of-color systems are more poorly calibrated (expected calibration error 0.18 vs 0.06, non-overlapping bootstrap confidence intervals), and it is this gap, not the non-significant error-rate gaps, that the per-group recalibration we recommend must target. Second, the favorable coverage gap rests on a different demographic partition (a validation-set median split) than the percentile split used for the discrimination, error-rate, and calibration analyses, and its significance would not survive correction across the nine group comparisons, so we do not lean on it.

Under one global operating threshold and markedly unequal base rates (detection prevalence 0.36 vs 0.19), error-rate and calibration parity cannot hold jointly, so the residual error-rate gap reflects a thresholding artifact remediable by group-aware thresholding or recalibration rather than a discrimination deficit. A prior California study audits a drinking-water-quality model for exactly such demographic error disparities[42]; our contribution is to trace the disparity upstream to the inequitable monitoring process that generates the labels. Any prioritization use should nonetheless be paired with a per-group error audit and must not divert oversight away from high-burden systems. Adjusted-association analysis confirms environmental signal persists (DML-adjusted AUROC 0.729) but is substantively small: all standardized E-values are uniformly small, so these are adjusted associations, not causal effects (Supplementary S20).

For environmental justice, the monitoring confound cuts twice. Measured disparities depend on where and how intensively agencies sample: the people-of-color burden ratio is 1.34 in the western test region but 1.48 nationally (Supplementary Table 20), so single-region, ascertainment-naive estimates understate the national picture (though inverse-propensity weighting shows the western disparity survives adjustment for observed monitoring propensity). These are distinct estimands rather than conflicting values: the national summary (system-count-weighted across all ten regions), the geographic deployment split (unadjusted, and after inverse-propensity adjustment), and the single western test region; we defend the national summary as the headline estimate and read the single-region and deployment-split figures as context for it.

Surveillance itself is also inequitably allocated (Fig. 4): high people-of-color-share systems are sampled 1.85-fold more intensively while low-income and low-education systems are sampled less, all robust to system size. The two equity signals differ sharply in robustness. The national monitoring-intensity disparity is significant under a stratified-by-region permutation and survives data-source adjustment. Adding data-source fixed effects attenuates the size-adjusted association from 0.060 to 0.043 log-samples per standard deviation ($p < 0.001$). Restricting to systems monitored predominantly under a single federal program (UCMR5) lowers the ratio from 1.85× to 1.37× (size-adjusted coefficient 0.021, $p < 0.001$). The pooled 1.85× therefore partly reflects that communities of color are over-represented in dense state monitoring programs rather than allocation within a single program, though a within-source disparity persists. The regional detection-burden disparity is more fragile, reaching significance in only a minority of regions under a spatially-aware null; we therefore rest the equity claim on the source-adjusted monitoring-intensity finding and read the regional detection-burden pattern as suggestive. Both contamination and the attention paid to it are environmental justice outcomes, and equity analyses on administrative monitoring data must model the allocation process or risk reporting artifacts of it.

Several limitations bound these conclusions. Extreme censoring (97.1%) renders concentration regression near-intractable (T2). ZCTA-centroid geocoding is imprecise, though results are robust to 5-km perturbation (Supplementary S7b). UCMR5's design (a census of systems serving >3,300 people plus a mandatory EPA-selected representative sample of smaller systems) makes the included population a non-random sample of all systems and creates MNAR selection that IPW may not fully address. DML assumes no unmeasured confounders. Detection-only sources preclude external validation (Supplementary S21).

Geographic generalization to genuinely unseen regions remains only partly demonstrated: the only geographically external test (CA GeoTracker) reaches AUROC 0.813 (DeLong $p < 0.001$) on a structurally different domain, but this transfer is carried by provenance features rather than environment (Supplementary S17). A matched experiment attributes a modest share of the holdout-to-LORO gap to validation-set reuse (early stopping on the external validation regions), with the remainder driven by regional heterogeneity (Supplementary S26). T6 transfer performance is modest because our features target anthropogenic rather than geogenic contamination. The per-system risk predictions that support utility-level screening are distributed with the archived dataset (Code Availability).

Machine-learning predictions of U.S. drinking-water contamination, as currently trained and evaluated, encode who is monitored as much as where contamination occurs. Once spatial leakage and monitoring ascertainment are both controlled, the transportable environmental signal is modest (out-of-region AUROC 0.691, 95% CI 0.615–0.769), and the same ascertainment process that inflates predictive skill distorts equity estimates while being inequitably allocated itself. By providing standardized tasks, two-confound evaluation protocols, monitoring-invariant baselines, reproducible pipelines, and a leave-one-region-out leaderboard,

AquaContam brings to administratively generated environmental data the kind of shared, leakage-aware evaluation that domain benchmarks such as GEO-Bench[22] established for Earth observation. Unlike general-purpose benchmarks built on curated, near-i.i.d. splits (for example ImageNet[43] or GLUE[44]), its central point is methodological: in surveillance-generated data the evaluation protocol itself, not the model architecture, is where most reported skill is won or lost. We urge adoption of geographic stratification and explicit ascertainment controls as the minimum evaluation standard for spatial environmental ML.

Methods

Data collection and preprocessing

AquaContam aggregates data from fifteen federal and state sources (all public records; see Data Availability for the two non-self-serve access routes). UCMR5 occurrence data[45] (29 PFAS + lithium, ~1.9M records) and UCMR3 data[46] (38 contaminants including 6 PFAS, ~1.1M records) were downloaded from the EPA's Compliance Monitoring Data portal as Latin-1 encoded text files within ZIP archives. SDWIS Lead and Copper Rule[47] (LCR) sampling results and system metadata were obtained from the EPA ECHO system, covering lead and copper compliance monitoring (916,899 records across lead and copper analytes; zero-measure rows are retained as non-detects. An earlier parse that excluded them, 694,419 records, backed pre-revision analyses and is preserved in repository history). State-level databases were accessed through their respective portals: Michigan MPART via ArcGIS REST API (5 PFAS), California GeoTracker GAMA program (PFAS monitoring CSV), Washington DOH PFAS monitoring results (9,251 records via direct CSV download), Missouri DNR PFAS sampling data via ArcGIS REST API (29 PFAS, 75,971 records), New Jersey DEP WaterViewer (25 PFAS, 248,107 records; headed-browser collection, see Data Availability), and Minnesota MDH compliance monitoring (obtained by written request under the Minnesota Government Data Practices Act; see Data Availability). North Carolina DEQ (5 PFAS) was pursued but its data were unavailable for bulk download. Ohio EPA (26,554 records via ArcGIS REST API) was evaluated but excluded because all PWSIDs overlap with SDWIS and only detected samples are reported. The USGS/EPA Water Quality Portal provided PFAS monitoring results across 49 CONUS states (13 PFAS analytes, 35,528 records via REST API). The EPA Facility Registry Service (FRS)[48] provided geolocated facility records filtered for PFAS-related industrial activity (40,828 sites). The EPA Toxics Release Inventory (TRI) provided PFAS release quantities from reporting facilities, and the EPA PFAS Analytic Tools database provided 761 federal sites (724 DoD/military) with known or suspected PFAS contamination, both used as auxiliary feature sources for proximity feature engineering.

All data sources undergo schema harmonization upon ingestion. Public Water System Identifiers (PWSID) are standardized to 9-character strings (e.g., "CA0101001") with leading zeros preserved. Concentration values are converted to micrograms per liter (ug/L) from source-specific units (parts per trillion, milligrams per liter, picograms per liter). Left-censored non-detect values, reported as below the method detection limit, are retained with an explicit censored boolean column (never silently dropped); this preserves the censoring structure for downstream methods that model it directly. The pooled T2 concentration target treats non-detect samples as zero when taking per-system maxima, so its RMSE mixes detection and quantification; the censoring-aware models receive the flags instead. Detection limits are recorded alongside each measurement. Duplicate samples (same PWSID, analyte, and sample date) are resolved by retaining the maximum concentration value.

Feature engineering

Four categories of geospatial features are extracted for each water system, identified by its ZCTA (ZIP Code Tabulation Area) centroid coordinates.

Category	Source	Features	Description
Proximity	EPA FRS, TRI, DoD	~25	Min distance and counts within 5/10/25 km to industrial, military, WWTP, airport, and landfill facilities; TRI release-weighted proximity; DoD PFAS site distance
Land use	NLCD 2021[49]	~15	Categorical land cover fractions (developed, agricultural, forested, wetland) within 5-km buffer via zonal statistics
Hydrogeology	USGS Principal Aquifers[50]	~10	Aquifer name and rock-type lithology (one-hot encoded) via spatial join; the USGS release carries no confinement attribute
Demographics	EPA EJScreen[51]	~8	Percent people of color, low income, education attainment, linguistic isolation, and composite EJ indices via block-group spatial join

All distances are computed in EPSG:5070 (CONUS Albers) using cKDTree spatial indexing.

Features with more than half their values missing are dropped prior to model training. Remaining missing values are imputed with column medians. Target leakage columns, aggregation statistics derived from monitoring results (detection rates, maximum concentrations), are automatically excluded from the feature matrix.

Benchmark task design

AquaContam defines seven benchmark tasks spanning the major water contamination prediction challenges:

- **T1 (Binary PFAS detection)**: Predict whether a given PFAS compound (default: PFOS) is detected above the method detection limit at a water system. Binary classification; primary metric: AUPRC. This label is monitoring-defined: reporting limits are heterogeneous across programs (UCMR3's limit is roughly an order of magnitude coarser than UCMR5's), so a system's detection status depends partly on who monitored it and at what sensitivity. Re-censoring every detection to a common reporting limit lowers T1 AUROC by about five points and collapses AUPRC (Supplementary Information, common-reporting-limit sensitivity), so the ranking signal is robust but the label itself carries the monitoring dependence this paper documents.

- **T2 (Concentration regression)**: Predict the concentration (ug/L) of a detected PFAS compound. Regression on detected-only samples; primary metric: RMSE. Included as a documented negative result establishing system-level prediction boundaries (Supplementary S25).

- **T3 (Multi-PFAS profiling)**: Simultaneously predict detection of five PFAS compounds (PFOS, PFOA, PFBS, PFHxS, HFPO-DA) at a water system. Multilabel classification using MultiOutputClassifier wrappers; primary metric: macro AUPRC.

- **T4 (Heavy metal prediction)**: Predict lead action-level exceedance (the Lead and Copper Rule 90th-percentile sampled lead concentration exceeding the 15 µg/L action level) at a water system from SDWIS compliance monitoring. Binary classification; primary metric: AUPRC.

- **T5 (Cross-contaminant transfer)**: Train on source contaminant (default: lead) and evaluate zero-shot prediction on target contaminant (default: PFOS). Evaluates cross-domain generalization of geospatial features. Primary metric: AUPRC.

- **T7 (Temporal prediction)**: Train on UCMR3 (2013–2015) and predict UCMR5 (2023) detection outcomes, with separate evaluation on persistent systems (monitored in both periods) and newly monitored systems. Primary metric: AUPRC.

T6 (Private-well risk extrapolation): Train on public-supply groundwater wells and predict EPA arsenic maximum-contaminant-level exceedance (≥10 µg/L) zero-shot on independent **domestic** (private) wells. Measured arsenic for 110,682 wells comes from the USGS National Groundwater Aggregation (Erickson et al. 2020; CC0 public domain), whose per-well water-use code distinguishes domestic (n = 12,561 with arsenic) from public-supply (n = 26,769) wells. We use arsenic because it is geogenic (governed by aquifer geochemistry rather than point sources), so non-domestic wells are not contamination-biased (the NGA release is an openly reproducible substitute for the now-confidential New Jersey Private Well Testing Act data). Models train on environmental features only (monitoring-intensity columns excluded); the domestic wells are a fully held-out zero-shot evaluation set. Primary metric: AUPRC.

All tasks use geographic stratification by EPA region for train/validation/test splits (60/15/25 ratio). The 10 EPA regions partition the United States into geographically contiguous blocks, ensuring that no geographic region appears in both training and test sets. This prevents spatial data leakage: the tendency for models to exploit shared geospatial confounders between nearby training and test locations rather than learning generalizable contamination predictors.

Model implementations

Twenty model families (29 model classes) are evaluated, ranging from trivial (class prior) to foundation models and ensembles; the task-specific censored regressors for T2 (Hurdle, XGBoost-AFT, Zero-Inflated Tobit) carry additional diagnostics in Supplementary S25:

Dummy Classifier (class prior): Predicts the training-set class distribution without using any features. Establishes the minimum performance floor expected by chance.

Logistic Regression: L2-regularized logistic regression with standardized features and balanced class weights. Establishes the performance achievable by a linear model on the same feature set.

XGBoost[52] (gradient-boosted decision trees): 500 estimators, max depth 6, learning rate 0.05, scale_pos_weight set to the inverse class ratio for imbalanced binary tasks. Early stopping on validation loss with patience of 50 rounds.

Random Forest[53]: 500 estimators, class_weight="balanced" for classification tasks, max features set to square root of the feature count.

MLP (multi-layer perceptron): 3-layer network (128-64-32) with dropout (0.3), AdamW optimizer, and early stopping; details in Supplementary S2.

LightGBM[54]: 500 estimators, 63 leaves, learning rate 0.05, with class-weighted binary tasks and early stopping (patience 50).

CatBoost[55]: 500 iterations, depth 6, learning rate 0.05, with balanced class weights and ordered boosting.

CNN1D: 1D convolutional network on tabular features; architecture and ordering sensitivity analysis in Supplementary S4.

Deep Tobit: Censoring-aware MLP trained with Tobit likelihood loss, predicting latent concentration from which P(detected) is derived (Supplementary S13).

TabPFN[56,57]: Pretrained foundation model performing in-context learning on tabular data. On CPU it stratified-subsamples the training set to 3,000 samples; all reported TabPFN results use this 3,000-sample subsample. Training sets above the 10,000-sample cap are otherwise rejected; for the leave-one-region-out leaderboard the oversized folds were run under the same 3,000-sample subsample rather than skipped (Supplementary S2).

GCN and GraphSAGE: Degrade to at-chance under geographic stratification due to disjoint test-region graphs (no edges to training nodes).

Hurdle and Zero-Inflated Tobit[58]: two-part censored regressors for the zero-inflated T2 concentration target, a detection (zero-versus-positive) stage feeding a positive-part Tobit regression, addressing the ~97% non-detect mass that defeats a single-stage model (T2).

XGBoost-AFT: gradient-boosted accelerated-failure-time model treating non-detect observations as left-censored survival times; also combined with the hurdle stage in a Hurdle-AFT ensemble (T2).

Voting Ensemble: Soft-voting ensemble of four tree-based classifiers (XGBoost, Random Forest, LightGBM, CatBoost), averaging predicted probabilities.

Stacking Ensemble: Two-level stacking ensemble using the same four tree-based classifiers as base learners with logistic regression as the meta-learner, trained via 5-fold cross-validation on base model predictions.

Invariant Contamination Predictor (ICP): Neural network with a shared encoder feeding two heads: a contamination predictor and a gradient-reversed monitoring adversary. The gradient reversal layer (GRL)[59] negates adversary gradients during backpropagation, forcing the encoder to learn representations from which monitoring intensity cannot be predicted, an objective related to invariant risk minimization[60]. Training uses IPW reweighting via logistic-regression propensity scores and Group DRO[61] with exponentiated gradient updates across EPA regions. The regressor variant uses Tobit NLL for censoring-aware regression. See Supplementary S17 for architecture details.

For T3 multilabel classification, PyTorch[62]-based models (MLP, CNN1D, Deep Tobit) are replaced with scikit-learn[63] MLPClassifier wrappers to enable MultiOutputClassifier integration, training independent binary classifiers per label.

Hyperparameter selection

Table 2 reports fixed default configurations (specified in configs/experiment.yaml) at seed 42, for reproducibility and to avoid validation-set overfitting. To verify this choice is not unfair to any model family, all tunable families additionally underwent symmetric grid search (12–18 configurations per model) plus Bayesian optimization (Optuna TPE sampler) on the T1

validation set, optimizing AUPRC. Tuning does not improve the geographic-holdout benchmark (it reorders T1 and collapses the Stacking ensemble below its own base learners, a validation-overfitting signature), and Supplementary Table 11 reports the tuned-vs-default comparison. Neural networks use early stopping on validation loss, matching the eval-set stopping used by tree-based models, with one exception: the adversarial ICP runs its full gradient-reversal schedule without early stopping, and the Voting and Stacking ensembles use fixed default base-learner configurations rather than inheriting tuned hyperparameters. Because of these asymmetries and the validation-overfitting seen under tuning, we de-emphasize fine-grained architecture rankings and report default-configuration results. Complete search spaces and final hyperparameter values are in Supplementary S2 and configs/experiment.yaml.

Evaluation metrics

Classification tasks (T1, T3, T4, T5): We report AUROC (area under the receiver operating characteristic curve), AUPRC (area under the precision-recall curve, preferred for imbalanced data), F1 score, precision, recall, accuracy, and balanced accuracy. AUPRC is the primary ranking metric for the leaderboard, as it is more informative than AUROC under severe class imbalance[64].

Regression tasks (T2): RMSE (root mean squared error), MAE (mean absolute error), R^2 (coefficient of determination), explained variance, and median absolute error. RMSE is the primary metric.

Multilabel tasks (T3): In addition to per-label metrics, we compute subset accuracy (exact match), hamming loss, macro and micro AUROC/AUPRC, and label ranking average precision.

All metrics are computed on the geographically held-out test set. Split-level metrics (train, validation, test) are reported to enable overfitting diagnosis. We report 95% bootstrap confidence intervals (1,000 iterations) for all classification metrics on the test set.

We use a single geographic split rather than k-fold cross-validation. Spatial k-fold approaches (e.g., leave-one-region-out) are possible but yield only 10 folds with highly variable fold sizes, making fold-level metrics unstable. Our fixed geographic split (train: regions 1,3,4,5,6; validation: 2,7; test: 8,9,10) provides a single, interpretable evaluation on a geographically distinct test partition, with bootstrap resampling providing confidence intervals. As a robustness check, we also report leave-one-region-out (LORO) cross-validation results (10 folds, one per EPA region) using XGBoost on T1. The ambient monitoring sources (CA GeoTracker, WQP) are reserved for external validation and excluded from the fixed-split benchmark, but they are retained in the LORO and split-comparison harnesses. Those two harnesses therefore operate on a modestly larger, ambient-inclusive population (16,281 versus 14,335 systems). Because the ambient sources are a harder, structurally distinct population, this asymmetry makes the LORO and split-comparison comparators more conservative rather than inflating the fixed-split headline.

Several T1 AUROC figures therefore recur in this paper, each produced by a different harness rather than being a conflicting estimate of one quantity: the 0.864 headline (full-feature geographic holdout), 0.809 on the streamlined single-model robustness harness (which drops ~605 geocoded systems and uses a reduced feature set, so it underestimates rather than inflates the full pipeline), 0.790 for the full-feature model under the split-comparison harness, and the leave-one-region-out mean of 0.782 (Supplementary Table 2, Supplementary S11).

The validation set (EPA Regions 2, 7) serves three roles: hyperparameter selection, early stopping, and threshold optimization. Because AUROC is threshold-independent, only early stopping can introduce val-reuse bias in AUROC. A matched experiment isolating this effect finds it accounts for a modest share of the holdout-to-LORO gap, with the remainder attributable

to regional heterogeneity (Supplementary S26). LORO CV (mean AUROC 0.782, 95% CI 0.705–0.860, with the full feature set; 0.691, 95% CI 0.615–0.769, provenance-reduced) serves as an independent robustness check.

Model calibration

For classification tasks, we compute the Expected Calibration Error (ECE) and Brier score to assess whether predicted probabilities match observed detection frequencies. Post-hoc calibration (isotonic regression, Platt scaling, and temperature scaling) and split conformal prediction[65] at significance levels alpha in {0.05, 0.10, 0.20} provide calibrated uncertainty quantification. Conformal coverage is reported as marginal over the pooled test set; because calibration data come from the validation regions, per-region coverage on test regions varies (0.878–0.967 at $\alpha = 0.05$) and per-region distribution-free guarantees are not claimed (Supplementary S6). Details are reported in Supplementary Information.

Statistics and reproducibility

Sample sizes were determined by complete data availability from federal and state monitoring programs (no a priori power analysis; observational study design). Two-sided DeLong tests were used for pairwise AUROC comparisons with Benjamini-Hochberg FDR correction for multiple testing. Confidence intervals are labeled by method throughout: per-model test-set intervals are i.i.d. bootstraps (1,000 iterations, percentile method) over spatially clustered systems and are therefore anti-conservative in the presence of the residual spatial autocorrelation we report; region-level (LORO) intervals are region-block bootstraps over the ten EPA-region folds; the national burden interval is a spatial block bootstrap. Permutation tests (10,000 permutations) assessed statistical significance of burden ratios in the environmental justice analysis. Moran's I with randomization inference (999 permutations) tested residual spatial autocorrelation. All experiments used a fixed random seed (42); software versions are recorded in software_versions.json alongside results. No monitoring records were discarded on outcome-related grounds, but several technical exclusions apply: 7,773 systems lacking geocodable coordinates are dropped from geospatial feature extraction; systems observed only through single-class detection-only sources cannot contribute to AUROC where noted; and EPA regions with fewer than 30 matched systems are excluded from per-region statistics. Blinding was not applicable (observational study of administrative data). Experiments were not randomized (observational study design using complete population data from EPA monitoring programs).

Spatial autocorrelation diagnostics

Moran's I analysis on model residuals (inverse-distance weights over the $k = 10$ nearest neighbors, multi-threshold at 25–200 km) confirms residual spatial autocorrelation ($I > 0$, $p < 0.05$), expected given genuine spatial structure in contamination. Residual Moran's I is positive across the benchmarked models and declines with distance (for the headline XGBoost model, 0.212 at 50 km and 0.077 at 200 km, consistent with Supplementary S9); this residual structure means the i.i.d. bootstrap confidence intervals reported throughout are approximate, and we corroborate the headline intervals with a region-block bootstrap (Supplementary S9). Geographic stratification prevents exploitation of this structure during evaluation. Full details are in Supplementary S9.

Environmental justice analysis

Environmental justice analysis employs burden ratios[66] to quantify contamination disparities across demographic groups. For a given demographic indicator *d* and contamination metric *c*, the burden ratio *B* is defined as:

$$B = c(\text{high-burden group}) / c(\text{reference group})$$

where high-burden is defined as communities above the 80th percentile of the demographic indicator and reference as communities below the 50th percentile. Test-set burden ratios are computed on the geographically stratified test set (EPA Regions 8, 9, 10; n = 3,780 systems) to ensure that disparity estimates are not confounded by spatial leakage; national estimates are system-count-weighted means of per-region burden ratios from LORO cross-validation, with a region-block-bootstrap 95% confidence interval (Supplementary S23). Demographic groups are defined using EJScreen block-group indicators: percent people of color, percent low income, and education attainment. Linguistic isolation was excluded from the test-set analysis because no test-set systems fell below the 50th percentile (an empty reference group), precluding burden ratio computation. Statistical significance is assessed via permutation testing (10,000 permutations), with Benjamini-Hochberg FDR correction for multiple comparisons across the three evaluable demographic dimensions.

To adjust detection disparities for differential monitoring, we compute a monitoring-adjusted burden ratio: stabilized inverse-propensity-of-monitoring weights (logistic-regression propensity scores estimated from environmental and proximity features only, the same machinery used by the ICP) reweight the high-burden and reference detection rates, and significance is assessed by permutation under the weighted estimator. This adjusts for who gets monitored under a monitoring-at-random-given-covariates assumption; it cannot rule out selection on unobservables (MNAR), which we state as a limitation.

Each system's demographics are attributed from the single nearest EJScreen block-group centroid (sjoin_nearest, 10-km cap), so one block group stands in for a potentially multi-block-group service area, an ecological-inference (modifiable-areal-unit) limitation that could bias the high/low split in unknown directions. To test sensitivity to this attribution, we recompute the test-region burden ratios under population-weighted areal apportionment. Each system's demographic value becomes a weighted mean over all TIGER 2023 block groups whose polygon intersects a buffer around the system. Each block group is weighted by its total population times the fraction of its area falling within the buffer (EPSG:5070; EJScreen 2023 shares). The single-nearest baseline reproduces the frozen burden ratios exactly, and the apportioned ratios are reported at 5-km and 10-km buffers (Supplementary Table 26).

The monitoring-inequity analysis treats monitoring allocation as the outcome. Among monitored systems, sampling intensity (n_samples) is compared between high-share (>80th percentile) and low-share (<50th percentile) systems for each EJScreen dimension via intensity ratios with permutation p-values, and via a linear regression of log sampling intensity on the standardized demographic indicator adjusting for population served (the dominant regulatory determinant of sampling frequency). Because the analysis is restricted to monitored systems, it measures inequity in monitoring *intensity*; selection into monitoring at all is governed by regulatory design (e.g., the UCMR5 >3,300-served eligibility threshold) and is reported as a scope limitation.

Data Availability

Most data sources are publicly downloadable from their respective federal and state agencies (Supplementary S1 lists URLs and access details); two are public records but not fully self-serve. New Jersey DEP chemical samples are public records under the New Jersey Open Public Records Act; because the WaterViewer portal sits behind a bot-protection layer, we collected them with a headed-browser scraper that reads the same public pages a browser would, with no authentication or access circumvention. Minnesota MDH compliance data are public records under the Minnesota Government Data Practices Act, provided on written request rather than bulk download (request route documented in docs/data_requests/mn_mdh_bulk_export.md); we hold them for analysis but redistribution requires the agency's confirmation, which we are pursuing. The Zenodo archive is therefore the

reproducible copy of record for the harmonized dataset; the Minnesota records are excluded from it pending the agency's confirmation, and the archive documents the request route so that others can request the same export and verify it against the pinned checksum. Per-source attributions, terms, and redistribution status are listed in docs/DATA_TERMS.md; the compiled data are distributed under CC BY 4.0 where source terms permit, chosen to maximize reuse with attribution (sources retain their original terms; Minnesota MDH redistribution is pending confirmation), while the accompanying code is licensed under the Apache License 2.0 (Code Availability). The curated, harmonized AquaContam dataset is archived on Zenodo (DOI: 10.5281/zenodo.22073200). Source data for all main-text figures are provided as Source Data files.

Code Availability

The AquaContam benchmark code (data harmonization, feature extraction, model training, and evaluation), together with the baseline model configurations needed to reproduce the reported results, is available at https://github.com/tjnewton/aquacontam under the Apache License 2.0. A Zenodo archive with a permanent DOI is deposited (DOI: 10.5281/zenodo.22073200). The reproducibility pipeline (scripts/reproduce.py) regenerates all results, figures, and tables from raw data downloads, plus the request-based Minnesota staging described in Data Availability, with a fixed random seed (42). Software versions are automatically recorded in software_versions.json alongside results. The per-system prediction export is git-ignored in the repository and is included, with the harmonized dataset, in the Zenodo archive. The tracked frozen archive is a slim snapshot (per-system prediction arrays are stripped; a slim national T1-PFOS risk surface is retained), sufficient to regenerate every table, every number-gate check, and the result-derived figures; the map figures additionally draw on the harmonized dataset, and the full prediction arrays are included in the Zenodo archive. The full software environment is specified in environment.yml (conda) and pyproject.toml (pip), which should be used for installation; the versions of the core scientific stack recorded at run time are archived in the frozen software_versions.json.

The committed paper gate (paper/final_gate.py) is a consistency and tamper-evidence check, not an independent re-derivation of the science: it verifies that every reader-facing number matches the frozen archive, that generated tables and figures regenerate deterministically, and that derived artifacts carry input-hash stamps; it does not re-run the pipeline. The manuscript sources are not distributed with the repository, so the gate's manuscript-consistency clauses (marker agreement, DOCX source manifests, claims pinning) run where the manuscript lives and report "not distributed" in the repository copy, which verifies the benchmark artifacts: generated tables, the leaderboard, input-hash stamps, archive checksums, and the per-figure Source Data. A full reproduction from raw downloads (scripts/reproduce.py --all) is a multi-day, GPU-dependent job (the leave-one-region-out and hyperparameter-optimization stages dominate the cost). A reviewer can instead verify those benchmark artifacts in minutes with python paper/final_gate.py --check (on Windows: PYTHONUTF8=1), and python paper/regenerate_leaderboard.py --check for the leaderboard, neither of which requires a pipeline run. On a fresh checkout a few unit tests assume artifacts from a prior full run and are skipped when run in isolation; the two gate checks above carry no such dependency. AquaContam is a research benchmark, not a regulatory or operational risk-assessment product.

References

1. Andrews, D. Q. & Naidenko, O. V. Population-wide exposure to per- and polyfluoroalkyl substances from drinking water in the United States. *Environ. Sci. Technol. Lett.* **7**, 931–936 (2020).

2. Hanna-Attisha, M., LaChance, J., Sadler, R. C. & Champney Schnepp, A. Elevated blood lead levels in children associated with the Flint drinking water crisis: a spatial analysis of risk and public health response. *Am. J. Public Health* **106**, 283–290 (2016).

3. Cornwell, D. A., Brown, R. A. & Via, S. H. National survey of lead service line occurrence. *J. Am. Water Works Assoc.* **108**, E182–E191 (2016).

4. Fenton, S. E. et al. Per- and polyfluoroalkyl substance toxicity and human health review: current state of knowledge and strategies for informing future research. *Environ. Toxicol. Chem.* **40**, 606–630 (2021).

5. Sunderland, E. M. et al. A review of the pathways of human exposure to poly- and perfluoroalkyl substances (PFASs) and present understanding of health effects. *J. Expo. Sci. Environ. Epidemiol.* **29**, 131–147 (2019).

6. Lanphear, B. P. et al. Low-level environmental lead exposure and children's intellectual function: an international pooled analysis. *Environ. Health Perspect.* **113**, 894–899 (2005).

7. U.S. Environmental Protection Agency. PFAS National Primary Drinking Water Regulation. 89 FR 32532 (2024).

8. U.S. Environmental Protection Agency. Seventh Drinking Water Infrastructure Needs Survey and Assessment. EPA 810-R-23-001 (2023).

9. Hu, X. C. et al. Detection of poly- and perfluoroalkyl substances (PFASs) in U.S. drinking water linked to industrial sites, military fire training areas, and wastewater treatment plants. *Environ. Sci. Technol. Lett.* **3**, 344–350 (2016).

10. Tokranov, A. K. et al. Predictions of groundwater PFAS occurrence at drinking water supply depths in the United States. *Science* **386**, 748–755 (2024).

11. Fernandez, N., Nejadhashemi, A. P. & Loveall, C. Large-scale assessment of PFAS compounds in drinking water sources using machine learning. *Water Res.* **243**, 120307 (2023).

12. McMahon, P. B. et al. Perfluoroalkyl and polyfluoroalkyl substances in groundwater used as a source of drinking water in the eastern United States. *Environ. Sci. Technol.* **56**, 2279–2288 (2022).

13. Stock, A., Gregr, E. J. & Chan, K. M. A. Data leakage jeopardizes ecological applications of machine learning. *Nat. Ecol. Evol.* **7**, 1743–1745 (2023).

14. Ploton, P. et al. Spatial validation reveals poor predictive performance of large-scale ecological mapping models. *Nat. Commun.* **11**, 4540 (2020).

15. Roberts, D. R. et al. Cross-validation strategies for data with temporal, spatial, hierarchical, or phylogenetic structure. *Ecography* **40**, 913–929 (2017).

16. Meyer, H. & Pebesma, E. Predicting into unknown space? Estimating the area of applicability of spatial prediction models. *Methods Ecol. Evol.* **12**, 1620–1633 (2021).

17. Kapoor, S. & Narayanan, A. Leakage and the reproducibility crisis in machine-learning-based science. *Patterns* **4**, 100804 (2023).

18. Koldasbayeva, D. et al. Challenges in data-driven geospatial modeling for environmental research and practice. *Nat. Commun.* **15**, 10700 (2024).

19. Phillips, S. J. et al. Sample selection bias and presence-only distribution models: implications for background and pseudo-absence data. *Ecol. Appl.* **19**, 181–197 (2009).

20. Fithian, W., Elith, J., Hastie, T. & Keith, D. A. Bias correction in species distribution models: pooling survey and collection data for multiple species. *Methods Ecol. Evol.* **6**, 424–438 (2015).

21. Sackett, D. L. Bias in analytic research. *J. Chronic Dis.* **32**, 51–63 (1979).

22. Lacoste, A. et al. GEO-Bench: toward foundation models for Earth monitoring. in *Proc. NeurIPS Datasets and Benchmarks* (2023).

23. Yeh, C. et al. SustainBench: benchmarks for monitoring the Sustainable Development Goals with machine learning. in *Proc. NeurIPS Datasets and Benchmarks* (2021).

24. Watson-Parris, D. et al. ClimateBench v1.0: a benchmark for data-driven climate projections. *J. Adv. Model. Earth Syst.* **14**, e2021MS002954 (2022).

25. U.S. Environmental Protection Agency. Safe Drinking Water Information System (SDWIS). https://www.epa.gov/ground-water-and-drinking-water/ safe-drinking-water-information-system-sdwis-federal-reporting (2024).

26. U.S. Census Bureau. 2020 ZIP Code Tabulation Areas (ZCTAs). TIGER/Line and Gazetteer Files (2023).

27. Grinsztajn, L., Oyallon, E. & Varoquaux, G. Why do tree-based models still outperform deep learning on typical tabular data? in *Proc. NeurIPS* (2022).

28. Shwartz-Ziv, R. & Armon, A. Tabular data: deep learning is not all you need. *Inf. Fusion* **81**, 84–90 (2022).

29. Lundberg, S. M. & Lee, S.-I. A unified approach to interpreting model predictions. in *Proc. NeurIPS* 4765–4774 (2017).

30. Salvatore, D. et al. Presumptive contamination: a new approach to PFAS contamination based on likely sources. *Environ. Sci. Technol. Lett.* **9**, 983–990 (2022).

31. Chernozhukov, V. et al. Double/debiased machine learning for treatment and structural parameters. *Econom. J.* **21**, C1–C68 (2018).

32. Peters, J., Bühlmann, P. & Meinshausen, N. Causal inference by using invariant prediction: identification and confidence intervals. *J. R. Stat. Soc. B* **78**, 947–1012 (2016).

33. Chouldechova, A. Fair prediction with disparate impact: a study of bias in recidivism prediction instruments. *Big Data* **5**, 153–163 (2017).

34. Kleinberg, J., Mullainathan, S. & Raghavan, M. Inherent trade-offs in the fair determination of risk scores. in *Proc. ITCS* (2017).

35. Mohai, P. & Saha, R. Which came first, people or pollution? A review of theory and evidence from longitudinal environmental justice studies. *Environ. Res. Lett.* **10**, 125011 (2015).

36. Bullard, R. D. *Dumping in Dixie: Race, Class, and Environmental Quality* (Westview Press, 3rd ed., 2000).

37. Tessum, C. W. et al. $PM_{2.5}$ polluters disproportionately and systemically affect people of color in the United States. *Sci. Adv.* **7**, eabf4491 (2021).

38. Liddie, J. M., Schaider, L. A. & Sunderland, E. M. Sociodemographic factors are associated with the abundance of PFAS sources and detection in U.S. community water systems. *Environ. Sci. Technol.* **57**, 7902–7912 (2023).

39. Banzhaf, S., Ma, L. & Timmins, C. Environmental justice: the economics of race, place, and pollution. *J. Econ. Perspect.* **33**, 185–208 (2019).

40. Martinez-Morata, I. et al. Nationwide geospatial analysis of county racial and ethnic composition and public drinking water arsenic and uranium. *Nat. Commun.* **13**, 7461 (2022).

41. Wadoux, A. M. J.-C., Heuvelink, G. B. M., de Bruin, S. & Brus, D. J. Spatial cross-validation is not the right way to evaluate map accuracy. *Ecol. Modell.* **457**, 109692 (2021).

42. Karasaki, S., Morello-Frosch, R. & Callaway, D. Machine learning for environmental justice: dissecting an algorithmic approach to predict drinking water quality in California. *Sci. Total Environ.* **951**, 175730 (2024).

43. Deng, J. et al. ImageNet: a large-scale hierarchical image database. in *Proc. IEEE CVPR* 248–255 (2009).

44. Wang, A., Singh, A., Michael, J., Hill, F., Levy, O. & Bowman, S. R. GLUE: a multi-task benchmark and analysis platform for natural language understanding. in *Proc. ICLR* (2019).

45. U.S. Environmental Protection Agency. Fifth Unregulated Contaminant Monitoring Rule (UCMR 5) occurrence data. https://www.epa.gov/dwucmr (2023).

46. U.S. Environmental Protection Agency. Third Unregulated Contaminant Monitoring Rule (UCMR 3) occurrence data. https://www.epa.gov/dwucmr (2016).

47. U.S. Environmental Protection Agency. Lead and Copper Rule Revisions (LCRR). 86 FR 4198 (2021).

48. U.S. Environmental Protection Agency. Facility Registry Service (FRS). https://www.epa.gov/frs (2024).

49. Dewitz, J. & U.S. Geological Survey. National Land Cover Database (NLCD) 2021 Products. U.S. Geological Survey data release. https://doi.org/10.5066/P9JZ7AO3 (2023).

50. U.S. Geological Survey. Principal Aquifers of the United States. https://water.usgs.gov/ogw/aquifer/map.html (2003).

51. U.S. Environmental Protection Agency. EJScreen: Environmental Justice Screening and Mapping Tool. Archived at https://web.archive.org/web/2024/https://www.epa.gov/ejscreen (2024).

52. Chen, T. & Guestrin, C. XGBoost: a scalable tree boosting system. in *Proc. KDD* 785–794 (2016).

53. Breiman, L. Random forests. *Mach. Learn.* **45**, 5–32 (2001).

54. Ke, G. et al. LightGBM: a highly efficient gradient boosting decision tree. in *Proc. NeurIPS* 3146–3154 (2017).

55. Prokhorenkova, L., Gusev, G., Vorobev, A., Dorogush, A. V. & Gulin, A. CatBoost: unbiased boosting with categorical features. in *Proc. NeurIPS* 6639–6649 (2018).

56. Hollmann, N. et al. TabPFN: a transformer that solves small tabular classification problems in a second. in *Proc. ICLR* (2023).

57. Hollmann, N. et al. Accurate predictions on small data with a tabular foundation model. *Nature* **637**, 319–326 (2025).

58. Tobin, J. Estimation of relationships for limited dependent variables. *Econometrica* **26**, 24–36 (1958).

59. Ganin, Y. et al. Domain-adversarial training of neural networks. *J. Mach. Learn. Res.* **17**, 1–35 (2016).

60. Arjovsky, M., Bottou, L., Gulrajani, I. & Lopez-Paz, D. Invariant risk minimization. Preprint at https://arxiv.org/abs/1907.02893 (2019).

61. Sagawa, S., Koh, P. W., Hashimoto, T. B. & Liang, P. Distributionally robust neural networks for group shifts: on the importance of regularization for worst-case generalization. in *Proc. ICLR* (2020).

62. Paszke, A. et al. PyTorch: an imperative style, high-performance deep learning library. in *Proc. NeurIPS* 8024–8035 (2019).

63. Pedregosa, F. et al. Scikit-learn: machine learning in Python. *J. Mach. Learn. Res.* **12**, 2825–2830 (2011).

64. Saito, T. & Rehmsmeier, M. The precision-recall plot is more informative than the ROC plot when evaluating binary classifiers on imbalanced datasets. *PLoS ONE* **10**, e0118432 (2015).

65. Vovk, V., Gammerman, A. & Shafer, G. *Algorithmic Learning in a Random World* (Springer, 2005).

66. Morello-Frosch, R. & Jesdale, B. M. Separate and unequal: residential segregation and estimated cancer risks associated with ambient air toxics in U.S. metropolitan areas. *Environ. Health Perspect.* **114**, 386–393 (2006).

Author Contributions

Tyler J. Newton: Conceptualization, Methodology, Software, Validation, Formal Analysis, Investigation, Data Curation, Writing, Review & Editing, Visualization, Project Administration.

Competing Interests
The author declares no competing interests.

Ethics Statement
This study uses exclusively public administrative data from federal and state environmental monitoring programs (EPA UCMR, SDWIS, FRS, EJScreen; state programs in MI, CA, OH, WA, MO, NJ, NC). No human subjects data were collected or used. Demographic data from EJScreen are aggregated at the Census block group level and cannot identify individuals. Water system identifiers (PWSIDs) are public records. The environmental justice analysis examines disparities in contamination exposure across demographic groups to inform equitable regulatory action, consistent with environmental justice principles that federal and state agencies have historically recognized.

Acknowledgements
We acknowledge the U.S. Environmental Protection Agency for making UCMR, SDWIS, FRS, and EJScreen data publicly available, and the USGS/EPA Water Quality Portal for providing nationwide water quality monitoring data. State-level data were obtained from the Michigan Department of Environment, Great Lakes, and Energy (MPART), California State Water Resources Control Board (GeoTracker GAMA), New Jersey Department of Environmental Protection, North Carolina Department of Environmental Quality, the Missouri Department of Natural Resources, the Ohio Environmental Protection Agency, and the Washington State Department of Health (DOH). This research received no external funding. This work was conducted independently using personal computing resources. We thank Gabrielle N. LaFayette for helpful discussion.

Figure Legends
Figure 1 | National-scale data integration. Map of the contiguous United States showing water system sampling locations from fifteen data sources. Federal sources (UCMR5, UCMR3, SDWIS, WQP; circles) provide national coverage across 95,223 water systems and ambient monitoring locations, while six state databases (MI MPART, CA GeoTracker, WA DOH, MO DNR, NJ DEP, MN MDH; triangles) provide complementary regional coverage. Points represent unique water system locations (n = 87,450 geocoded systems) colored by data source using a colorblind-safe palette. The dataset integrates over 4 million water quality records with standardized units (micrograms per liter) and explicit censoring flags. See Table 1 for per-source sample counts and analyte coverage.

Figure 2 | Two compounding confounds inflate reported skill. a, Spatial leakage: T1 (PFAS detection) AUPRC for XGBoost on the baseline proximity/demographic feature set under random versus geographically stratified splitting (0.744 vs 0.532; 1.40× inflation). **b**, Ascertainment, in two comparisons. First, T1 AUPRC with versus without detection-only data sources (0.760 → 0.343; prevalence-independent AUROC 0.838 → 0.714; n = 256 systems excluded). Second, T4 (lead action-level) AUPRC with versus without monitoring-intensity features (0.421 → 0.302, after removing a target-leakage artifact that had inflated the T4 baseline to 0.902). Together the two confounds inflate the evaluation and the learnable signal; the sections that follow decompose how much skill survives when both are removed. See Extended Data Table 4 for the full random-vs-geographic comparison and Extended Data Table 1 for category ablations.

Figure 3 | Models learn the monitoring process. Mean absolute SHAP value for the top 15 features of the T1 XGBoost model (SHAP computed on the n = 2,846 test systems). **a**, With the full feature set, data-source provenance proxies dominate: monitoring intensity (n_samples; mean |SHAP| 0.383) is the single largest feature, followed by the owner-type missingness

indicator (which database reported a system; 0.287) and the mean detection limit (0.045). **b**, With the ten provenance and monitoring features removed, attribution shifts to the substantive environmental drivers (system type, source water type, wetland fraction, land use, aquifer lithology). See Extended Data Fig. 2 for the adjusted-versus-correlational (DML) comparison and Extended Data Table 1 for feature-category ablation.

Figure 4 | Inequitable monitoring. a, Mean sampling intensity (samples per system) among monitored systems for high-share (>80th percentile) versus low-share (<50th percentile) systems on four EJScreen demographic dimensions, annotated with the high/low intensity ratio (systems serving communities of color are sampled 1.85× more; an infinite ratio indicates no low-share systems). **b**, Population-size-adjusted regression coefficients (log samples per 1 s.d. of the demographic indicator) with 95% confidence intervals; communities of color are over-sampled while low-income and low-education communities are under-sampled, all $p < 0.001$. Differential ascertainment biases both contamination estimates and the equity conclusions drawn from them. Test-set detection-burden ratios are reported in Extended Data Table 2.

Extended Data

Extended Data Figures

Extended Data Fig. 1: Geographic split map (EPA regions by train/val/test)

Map of the contiguous United States showing the geographic stratification used for all benchmark tasks. The 10 EPA regions are partitioned into training (Regions 1, 3, 4, 5, 6; blue), validation (Regions 2, 7; amber), and test (Regions 8, 9, 10; orange) sets, maintaining a 60/15/25 ratio. Split membership is derived from the PWSID state prefix. 1,818 systems are excluded from this map only, not from the benchmark: their geocoded coordinate falls inside a state belonging to a different EPA region than their PWSID prefix, which marks a wrong-ZIP geocoding artifact when judged against US Census state boundary polygons (Supplementary S7b).

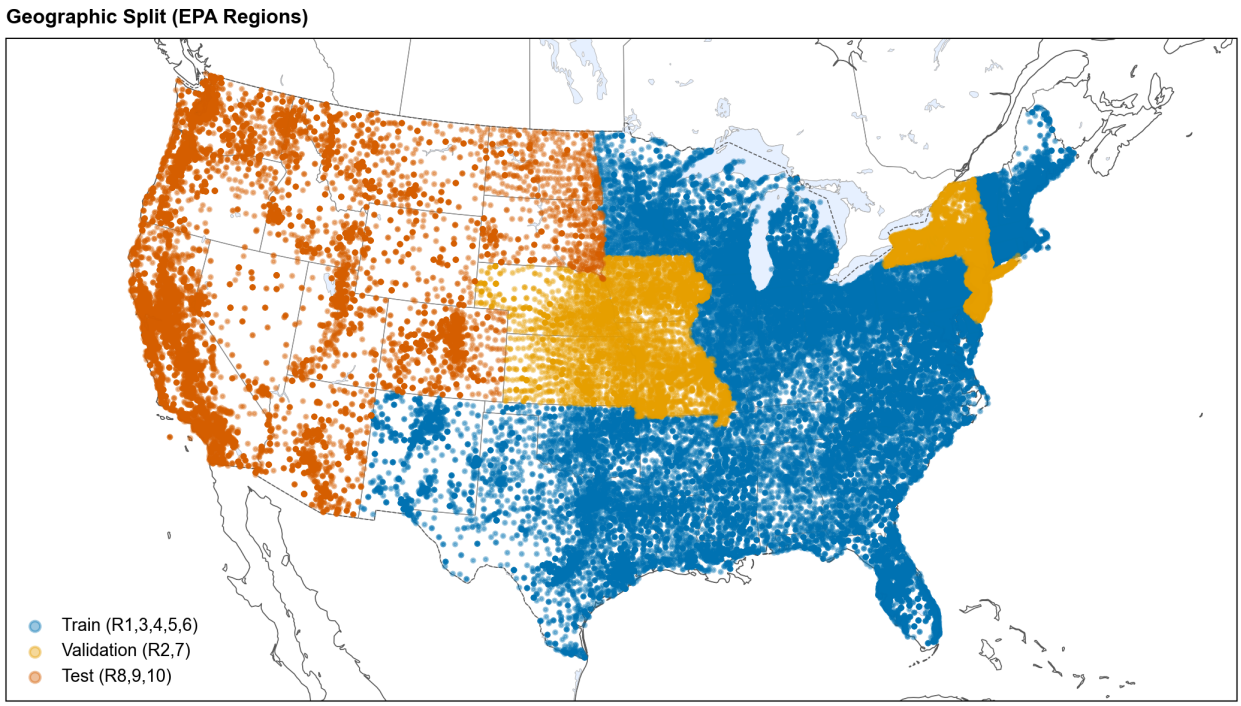

Extended Data Fig. 1

Extended Data Fig. 2: SHAP vs DML adjusted association comparison

Horizontal twin-bar chart comparing SHAP importance (correlational) and DML adjusted effects (standardized, per 1-s.d.) for the top 12 features in the T1 XGBoost model. The aggregate rank correlation between DML-adjusted and correlational feature rankings is modest but significant (Spearman ρ = 0.24, p = 0.032, n = 80), and a grouped permutation test finds no feature category displacing more than chance (Supplementary S14). Individual features nonetheless reorder substantially: 69 of 130 FDR-corrected DML coefficients are significant, and the largest displacements are environmental rather than demographic (pct_wetland_5km falls 48 positions). Among demographics, pct_less_hs_education and pct_people_of_color both retain significant adjusted associations once monitoring confounders are adjusted for (education SHAP rank 76 → DML rank 39; people-of-color standardized +0.022 per 1-s.d., p_FDR < 0.001), whereas pct_low_income does not (p_FDR = 0.54), consistent with its correlational signal being largely monitoring-mediated. Monitoring intensity shows the opposite pattern: high SHAP but smaller

adjusted effects, consistent with confounding. Industrial-proximity and Superfund-proximity features retain the strongest adjusted effects (p_FDR < 0.001), with airport, landfill, and WWTP distances also significant (p_FDR < 0.05), supporting mechanistic relevance.

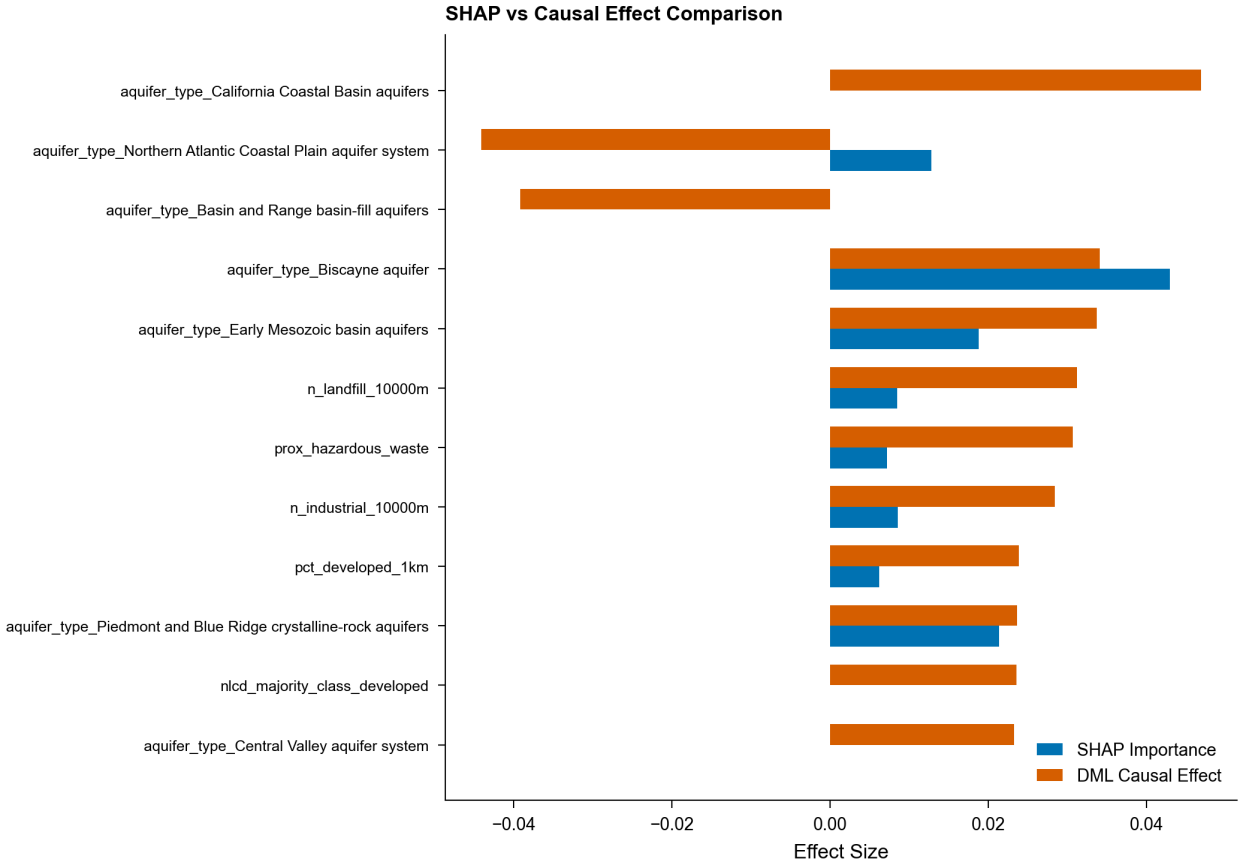

Extended Data Fig. 2

Extended Data Fig. 3: Conformal prediction per-region coverage

Per-EPA-region coverage of split conformal prediction sets at α = 0.05 (target 95%). Marginal coverage over the pooled test set is 0.910; per-region coverage varies from 0.878 (Region 9, n = 2,410) to 0.967 (Region 8, n = 538). Because calibration data come from the validation regions, coverage is guaranteed only marginally; per-region distribution-free guarantees are not claimed, and Region 9 under-covers at every significance level examined (Supplementary S6).

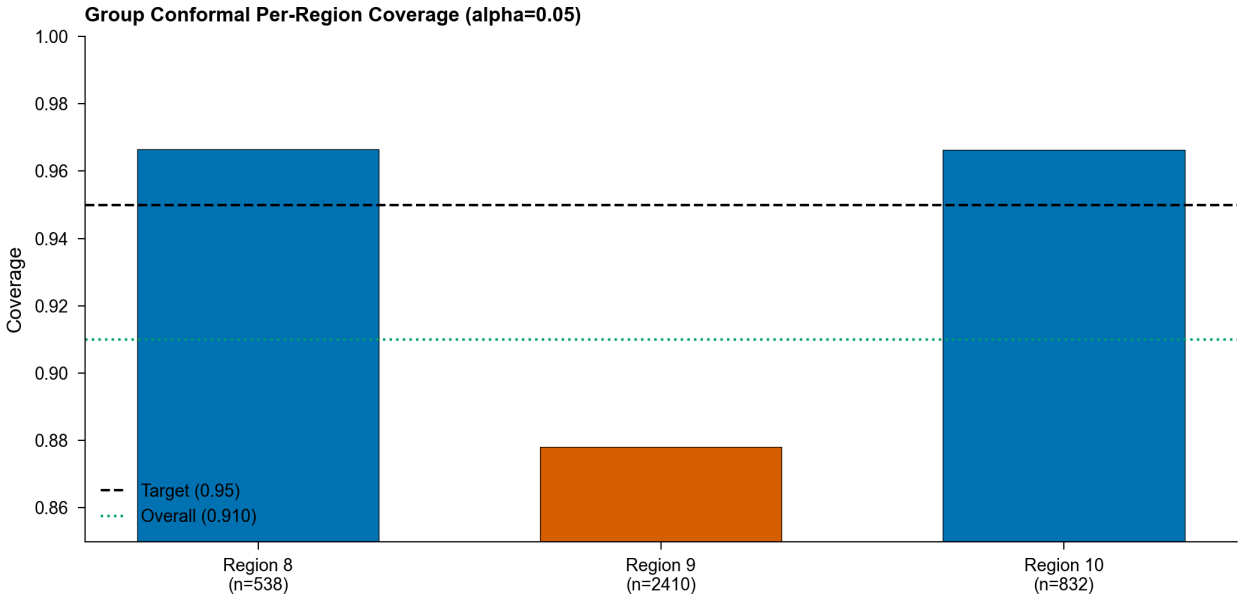

Extended Data Fig. 3

Extended Data Fig. 4: ICP training dynamics and metrics

a, Training dynamics of the Invariant Contamination Predictor showing task loss, adversary (monitoring-head) loss, and the λ_adv schedule over epochs. This is the training trace of the T1 ICP run captured through the canonical pipeline (seed 42); the same run reproduces the panel-b test AUROC, so panel a is the training history of the panel-b model rather than a separate re-fit. Task loss decreases steadily. After the warmup period λ_adv ramps to its maximum and the adversary's monitoring-prediction loss remains high and approximately flat, indicating the representation does not encode the targeted confounders. A held-out probe confirms that data-source provenance is also suppressed (Supplementary S17). **b**, ICP classification performance (AUROC, AUPRC) across benchmark tasks (T1 AUROC 0.731). See Table 3 for the full monitoring-invariance decomposition.

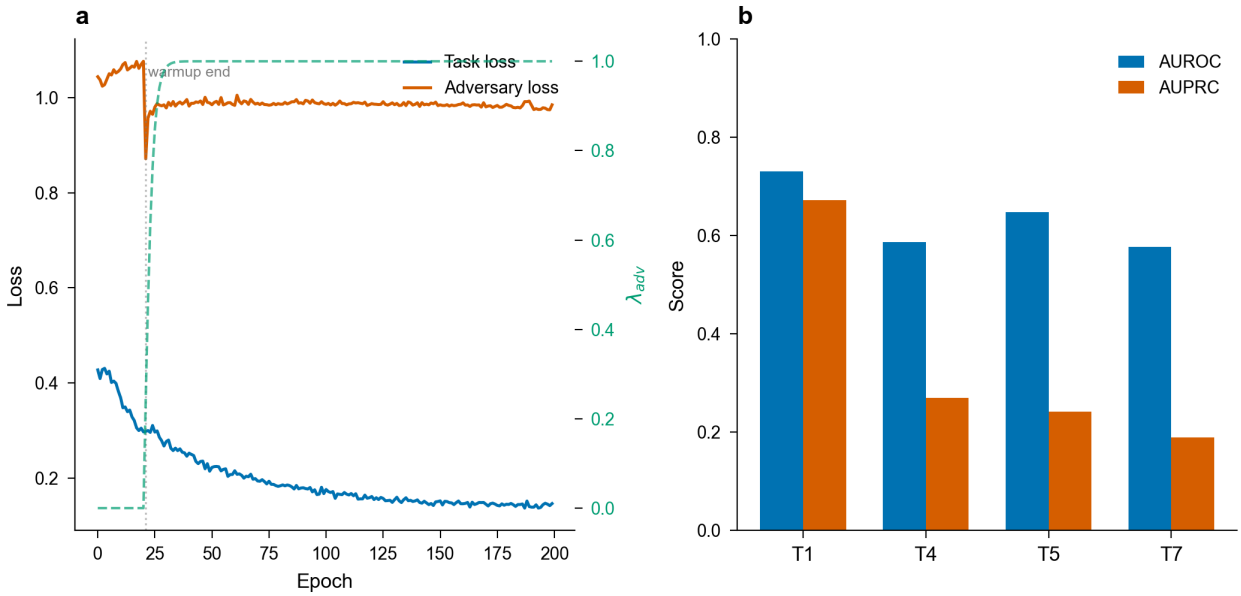

Extended Data Fig. 4

Extended Data Fig. 5: Benchmark performance overview

Test-set AUROC and AUPRC for the condensed model set on T1 (PFAS detection) and T4 (lead action-level exceedance) under geographic stratification, with 95% bootstrap confidence intervals. Companion visualization to Table 2; T4's nominally strong performance is monitoring-confounded (see Fig. 2 and Table 3).

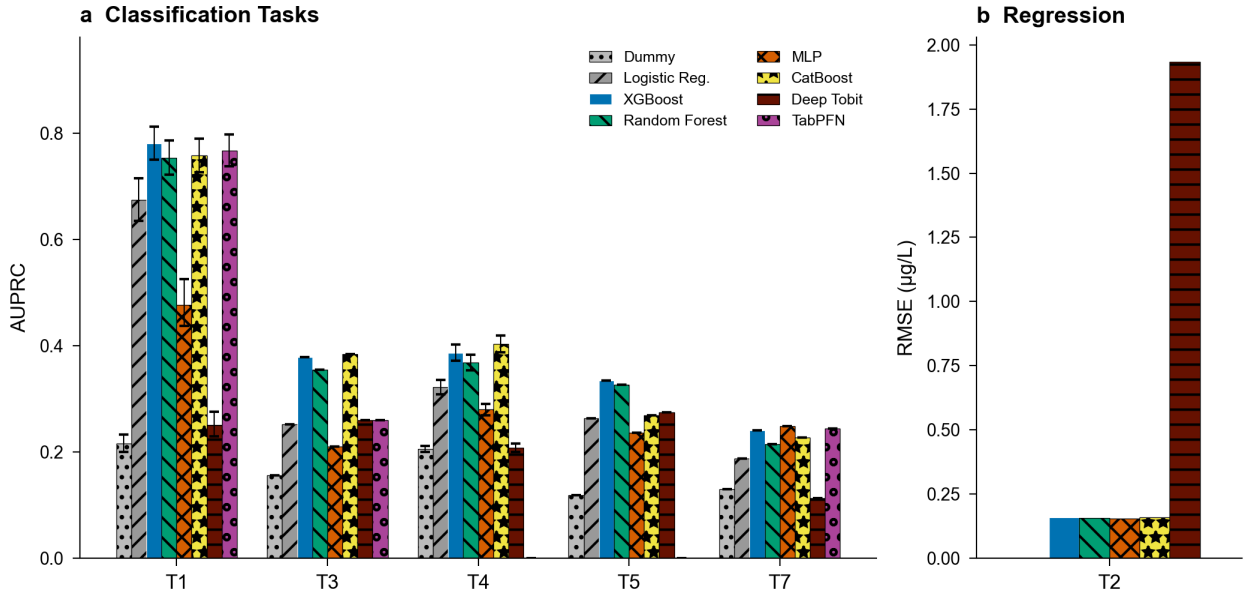

Extended Data Fig. 5

Extended Data Tables

Extended Data Table 1: Feature category ablation results

Drop-one-category ablation study for T1 (PFAS detection) and T4 (heavy metal action level) using XGBoost with train-only imputation. For each feature category, the number of features removed, baseline and ablated AUPRC, performance delta, and paired bootstrap p-value with Benjamini-Hochberg FDR correction (n = 1,000; T4 uses concatenated LORO out-of-fold predictions) are reported. On the small T1 geographic test set the monitoring-intensity ablation reduces AUPRC on both tasks, with a substantially larger and more robust effect for T4 once a target-leakage artifact inflating the T4 baseline is removed.

Task	Category	N Features	Baseline AUPRC	Ablated AUPRC	ΔAUPRC	p-value	p (FDR)
T1	all_features	0	0.665	0.665	0	—	—
T1	proximity	16	0.665	0.653	-0.0119	0.012	0.024
T1	land_use	28	0.665	0.667	0.0021	0.696	0.696
T1	hydrogeology	45	0.665	0.67	0.0042	0.368	0.421
T1	aquifer_type_only	43	0.665	0.656	-0.0098	0.038	0.061

Task	Category	N Features	Baseline AUPRC	Ablated AUPRC	ΔAUPRC	p-value	p (FDR)
T1	demographics	5	0.665	0.671	0.006	0.128	0.171
T1	n_samples_only	1	0.665	0.633	-0.0325	<0.001	<0.001
T1	monitoring_intensity	2	0.665	0.598	-0.0673	<0.001	<0.001
T1	system_characteristics	4	0.665	0.597	-0.0681	<0.001	<0.001
T4	all_features	0	0.421	0.421	0	—	—
T4	proximity	16	0.421	0.42	-0.0012	0.104	0.119
T4	land_use	28	0.421	0.418	-0.0031	<0.001	<0.001
T4	hydrogeology	55	0.421	0.418	-0.0036	<0.001	<0.001
T4	aquifer_type_only	53	0.421	0.419	-0.0022	<0.001	<0.001
T4	demographics	5	0.421	0.422	0.001	0.444	0.444
T4	n_samples_only	1	0.421	0.302	-0.1194	<0.001	<0.001
T4	monitoring_intensity	1	0.421	0.302	-0.1194	<0.001	<0.001
T4	system_characteristics	3	0.421	0.303	-0.1185	<0.001	<0.001

Extended Data Table 2: Equity analysis summary

Environmental justice burden ratios across three evaluable demographic dimensions (percent people of color, percent low income, education attainment). Linguistic isolation was excluded because no test-set systems fell below the 50th percentile (an empty reference group precludes burden ratio computation). The PFAS detection burden ratio along percent-people-of-color is 1.88 in the geographically stratified test set (EPA Regions 8, 9, 10; n_high = 618, n_ref = 1,544). Across the test set, inverse-propensity-of-monitoring weighting attenuates the people-of-color burden from 1.88 to 1.62 (still significant, permutation $p < 0.001$), so the disparity is not an ascertainment artifact; the LORO-weighted national mean is 1.48 (Supplementary Table 20). Permutation test p-values with Benjamini-Hochberg FDR correction. Per-group AUROC is similar across groups (0.799 high-burden vs 0.750 reference).

Demographic Group	Burden Ratio	Prediction Ratio	AUROC (High)	AUROC (Low)	N (High)	N (Low)	p-value	p-value (FDR)
People Of Color	1.88	1.19	0.799	0.75	618	1544	0.0001	0.0002
Low Income	1.4	1.37	0.797	0.768	618	1544	0.0003	0.0004

Demographic Group	Burden Ratio	Prediction Ratio	AUROC (High)	AUROC (Low)	N (High)	N (Low)	p-value	p-value (FDR)
Less Hs Education	1.54	1.13	0.827	0.76	621	1544	0.0001	0.0002

Extended Data Table 3: Literature comparison

Comparison of AquaContam (XGBoost, controlled configuration) with prior ML studies for water contamination prediction. Prior studies report high AUROC under random cross-validation without geographic holdout. In our controlled comparison the same XGBoost configuration (baseline feature set) yields AUROC 0.869 under random splitting and 0.699 under geographic stratification. A size-matched random control (training set subsampled to the geographic training-set size) reproduces the random-split result, so the drop reflects the evaluation protocol rather than model, feature, or training-set-size differences.

Study	Year	Dataset Size	Analytes	Geographic Scope	Split Method	Best AUROC	Best AUPRC	Feature Categories	Open Code
Hu et al.	2016	~4800 sites	6 PFAS	National (US)	N/A (spatial regression)	R^2=0.38-0.62	NR	Industrial proximity, land use, hydrology	No
Tokranov et al.	2024	~5000 wells	PFAS	National (US)	Random CV	~0.85	NR	Land use, hydrogeology, demographics	Partial
Fernandez et al.	2023	~4200 wells	6 PFAS	Michigan	10-fold stratified CV	>0.90	NR	Proximity, land use, demographics, hydrogeology	No
AquaContam (random split)*	2026	12136 systems	29 PFAS + heavy metals	National (US)	Random split	0.869	0.744	Proximity, land use, hydrogeology, demographics, system chars	Yes
AquaContam (geographic)*	2026	12136 systems	29 PFAS + heavy metals	National (US)	Geographic (EPA region)	0.699	0.532	Proximity, land use, hydrogeology, demographics, system chars	Yes

Extended Data Table 4: Random versus geographic split comparison

Controlled three-model × three-feature-set comparison (XGBoost, Random Forest, Logistic Regression × baseline, literature-equivalent, and full feature sets; 14,405 systems) of performance under random versus geographically stratified splits for T1 (PFAS detection). AUPRC inflation under random splitting reaches up to 58%, largest for logistic regression with the full feature set (0.723 random vs 0.457 geographic); the benchmark XGBoost/baseline cell inflates by 40% (0.744 vs 0.532). A size-matched random control preserves inflation of a similar magnitude (Supplementary Table 1), ruling out training-set size as the driver. The DeLong column reports a paired test of Full-feature versus Baseline-feature AUROC on the shared geographic test set, shown on the geographic/Full rows, together with the signed difference (ΔAUROC = Full minus Baseline). That difference is negative for logistic regression, whose Full-feature model performs significantly worse.

Model	Features	Split	AUROC	AUPRC	DeLong p
XGBoost	Fernandez	Geographic	0.699 [0.680-0.718]	0.499	—
XGBoost	Fernandez	Random	0.860 ± 0.011	0.722	—
RandomForest	Fernandez	Geographic	0.700 [0.682-0.719]	0.532	—
RandomForest	Fernandez	Random	0.862 ± 0.011	0.711	—
LogisticRegression	Fernandez	Geographic	0.629 [0.607-0.648]	0.451	—
LogisticRegression	Fernandez	Random	0.705 ± 0.013	0.427	—
XGBoost	Baseline	Geographic	0.699 [0.680-0.719]	0.532	—
XGBoost	Baseline	Random	0.869 ± 0.009	0.744	—
RandomForest	Baseline	Geographic	0.719 [0.702-0.738]	0.551	—
RandomForest	Baseline	Random	0.869 ± 0.010	0.718	—
LogisticRegression	Baseline	Geographic	0.736 [0.717-0.756]	0.559	—
LogisticRegression	Baseline	Random	0.749 ± 0.012	0.47	—
XGBoost	Full	Geographic	0.790 [0.774-0.806]	0.672	<0.001 (ΔAUROC +0.091)
XGBoost	Full	Random	0.901 ± 0.010	0.805	—
RandomForest	Full	Geographic	0.805 [0.788-0.820]	0.688	<0.001 (ΔAUROC +0.086)
RandomForest	Full	Random	0.889 ± 0.012	0.773	—
LogisticRegression	Full	Geographic	0.654 [0.635-0.674]	0.457	<0.001 (ΔAUROC -0.082)
LogisticRegression	Full	Random	0.873 ± 0.009	0.723	—

†DeLong p: paired test of Full-feature vs Baseline-feature AUROC on the shared geographic test set (reported on the geographic/Full rows); ΔAUROC = Full − Baseline, so a negative value means the Full feature set performs worse.

Extended Data Table 5: Cross-source and geographic external validation

T1 (PFAS detection) model performance evaluated on independent state databases. The fitted XGBoost model (trained on UCMR5/UCMR3 with geographic stratification) is applied to each state database separately. 95% bootstrap CIs (1,000 iterations) are reported for AUROC. For states whose EPA region overlaps the training set, overlapping PWSIDs are excluded.

Panel A: Cross-source validation (independent PWS databases within validation-region geography):

State DB	EPA Region	Split Role	n Systems	AUROC [95% CI]	AUPRC	Detection Rate
NJ DEP	R2	val	1,310	0.789 [0.765-0.812]	0.792	0.473
MO DNR	R7	val	1,208	0.829 [0.767-0.885]	0.281	0.052

Panel B: Geographic external validation (test-region geography, non-PWS monitoring domain):

State DB	EPA Region	Split Role	n Systems	AUROC [95% CI]	AUPRC	Detection Rate
CA GeoTracker	R9	test	1,421	0.813	0.707	0.297

†On the larger external sample the model performs above chance (DeLong test vs. AUROC = 0.5: $p < 0.001$).

Panel C: Detection-only databases (single-class data precludes AUROC). Two detection-only sources are retained for validation (MI MPART, WA DOH); Ohio EPA is excluded because its PWSIDs overlap SDWIS, and NC DEQ provides no usable records:

State DB	EPA Region	Split Role	n Systems	AUROC	AUPRC	Detection Rate
MI MPART	R5	train	153	—	—	100% (single-class)
WA DOH	R10	test	256	—	—	100% (single-class)
OH EPA	R5	—	—	—	—	Excluded (SDWIS PWSID overlap)
NC DEQ	R4	—	—	—	—	Unavailable

Supplementary Information

S1: Data Source Details

UCMR5 (Unregulated Contaminant Monitoring Rule, 5th cycle)

- **Period**: 2023
- **Samples**: 1,928,117 analytical results
- **Analytes**: 29 PFAS compounds + lithium (30 total)
- **Censoring**: 97.1% of results are non-detect (left-censored)
- **Source**: EPA UCMR5 occurrence data (https://www.epa.gov/dwucmr/occurrence-data-unregulated-contaminant-monitoring-rule)
- **Encoding**: Latin-1 (facility names contain accented characters)

UCMR3 (Unregulated Contaminant Monitoring Rule, 3rd cycle)

- **Period**: 2013-2015
- **Samples**: 1,069,174 analytical results
- **Analytes**: 38 contaminants including 6 PFAS (PFOS, PFOA, PFBS, PFHxS, PFHpA, PFNA)
- **Censoring**: 76.4% non-detect
- **Source**: EPA UCMR3 occurrence data

SDWIS (Safe Drinking Water Information System)

- **Systems**: ~150,000 public water systems
- **Analytes**: Lead, copper (from Lead and Copper Rule sampling)
- **Source**: EPA ECHO SDWIS downloads

EPA FRS (Facility Registry Service)

- **Facilities**: 40,828 PFAS-related facility sites
- **Classification**: SIC/NAICS codes + interest types (industrial, military, WWTP, airport, landfill)
- **Source**: EPA FRS national downloads

State Databases

State	Source	Analytes	Format
Michigan	MPART (ArcGIS REST)	5 PFAS	JSON/API
California	GeoTracker GAMA	29 PFAS	CSV
Ohio	EPA (ArcGIS REST)	6 PFAS	JSON/API

State	Source	Analytes	Format
Washington	DOH	14 PFAS	CSV
Missouri	DNR (ArcGIS REST)	29 PFAS	JSON/API
New Jersey	DEP (waterviewer REST)	25 PFAS	JSON/API
North Carolina	DEQ	GenX + 5 PFAS	Excel/CSV
Minnesota	MDH (manual bulk export)	27 PFAS	Excel

Minnesota MDH is a manually provided bulk export (no public API; request route in docs/data_requests/mn_mdh_bulk_export.md), parsed to 247,230 measurements across 1,357 public water systems (2005–2026, ~92% non-detect by substitution at the reporting limit). It enters the in-split benchmark population as a public-water-system compliance source. As an independent corroboration of the ascertainment confound, among the 194 Minnesota systems sampled for PFOS by both the federal UCMR cycles and MDH, 19 of the 180 (10.6%) that UCMR recorded as non-detect are detected once MDH's independent, longer-window monitoring is included. This is direct evidence that measured detection tracks who and how much a system is monitored, not only the underlying environment.

WQP (USGS/EPA Water Quality Portal)

- **Records**: 35,528 valid PFAS monitoring results
- **Analytes**: 13 PFAS compounds across 49 CONUS states
- **Censoring**: 38.7% non-detect
- **Source**: USGS/EPA Water Quality Portal REST API (https://www.waterqualitydata.us/)
- **Notes**: Monitoring locations are not public water systems; synthetic WQP_ identifiers used. API batches queries in groups of three characteristicName values.
- **Cross-source diagnostic**: applying the T1 model to WQP as an out-of-sample check yields a pooled AUROC of 0.42, below chance. This is a Simpson's-paradox artifact of pooling regions with very different detection base rates (four of five per-region AUROCs are above chance); it is a fair-transfer failure for ambient, non-PWS data rather than a model defect, and no reader-facing claim rests on it. Like the CA GeoTracker ambient result, it reinforces that geographic generalization to ambient sources remains undemonstrated.

TRI (Toxics Release Inventory)

- **Purpose**: PFAS release quantities from reporting industrial facilities
- **Source**: EPA TRI downloads (https://www.epa.gov/toxics-release-inventory-tri-program)
- **Usage**: Auxiliary data source for proximity feature engineering (facility distance/density)

DoD PFAS Sites

- **Sites**: 761 federal sites (724 DoD/military) with known or suspected PFAS contamination
- **Source**: EPA PFAS Analytic Tools database

- **Usage**: Auxiliary data source for proximity feature engineering (military installation distance)

Geospatial Data

Dataset	Source	Resolution	Purpose
NLCD 2021	USGS MRLC	30 m	Land use fractions
EJScreen	EPA (Zenodo archive)	Block group	Demographics
Principal Aquifers	USGS	Polygon	Hydrogeology
Census ZCTA	US Census Bureau	ZCTA	Geocoding

S2: Hyperparameter Configurations

All model hyperparameters are specified in configs/experiment.yaml. Default configurations used for all benchmark results:

XGBoost Classifier

```
n_estimators: 500
max_depth: 6
learning_rate: 0.05
subsample: 0.8
colsample_bytree: 0.8
min_child_weight: 5
scale_pos_weight: auto  # computed from class ratio
early_stopping_rounds: 50
eval_metric: aucpr
```

Random Forest Classifier

```
n_estimators: 500
max_features: sqrt
max_depth: null  # unlimited
min_samples_leaf: 5
class_weight: balanced
```

LightGBM Classifier

```
n_estimators: 500
num_leaves: 63
learning_rate: 0.05
subsample: 0.8
colsample_bytree: 0.8
min_child_samples: 20
is_unbalance: true
early_stopping_rounds: 50
```

CatBoost Classifier

```
iterations: 500
depth: 6
learning_rate: 0.05
auto_class_weights: Balanced
early_stopping_rounds: 50
```

MLP Classifier
hidden_sizes: [128, 64, 32]
dropout: 0.3
learning_rate: 0.001
epochs: 200
batch_size: 256
patience: 20

Voting Ensemble
voting: soft
base_models: [xgboost, random_forest, lightgbm, catboost]

Stacking Ensemble
final_estimator: logistic # LogisticRegression meta-learner
cv: 5
base_models: [xgboost, random_forest, lightgbm, catboost]

Symmetric Tuning Grids
Each model family receives symmetric hyperparameter tuning effort:

Model	Parameters Tuned	Grid Size
XGBoost	max_depth, learning_rate, n_estimators	18
Random Forest	n_estimators, max_depth, max_features	12
LightGBM	num_leaves, learning_rate, n_estimators	18
CatBoost	depth, learning_rate, iterations	18
MLP	hidden_sizes, learning_rate, dropout	18
CNN1D	n_filters, learning_rate, dropout	18

S3: Optuna Convergence Results
Bayesian hyperparameter optimization using Optuna Tree-Parzen Estimator (TPE) sampler was run for 50 trials per model family (XGBoost, Random Forest, LightGBM, CatBoost, MLP, CNN1D) on the T1 PFAS detection task. Results are saved to results/optuna_tuning.json.

The Optuna search spaces use broader ranges than grid search, enabling exploration of regions that grid search may miss. Key findings:

- Optuna trials converge within ~30 trials for tree-based models
- Final AUPRC improvements over grid search are typically modest (< 0.01)
- The TPE sampler with seed=42 ensures reproducibility

S4: CNN1D Feature Ordering Sensitivity
The CNN1D architecture treats tabular features as a 1D signal, applying convolutional filters across adjacent features. Since feature ordering is arbitrary in tabular data, we conducted a sensitivity analysis with seven orderings: alphabetical, domain-grouped (proximity → land use → hydrogeology → demographics), and five random permutations.

Results show that CNN1D performance is sensitive to feature ordering (AUROC mean 0.758 ± 0.022; AUPRC mean 0.566 ± 0.046). Alphabetical ordering achieves the highest AUROC (0.794), ahead of domain-grouped (0.776), with random orderings lower. This sensitivity confirms that convolutional architectures are not ideal for unstructured tabular data, and supports the benchmark result that tree-based models consistently outperform deep learning on AquaContam tasks.

S5: Model Calibration Details

We evaluate model calibration using Expected Calibration Error (ECE), Brier score, and reliability diagrams, then apply post-hoc calibration (isotonic regression, Platt scaling, and temperature scaling) to improve probability estimates. Pre-calibration ECE varies substantially across models: CNN1D exhibits the highest miscalibration (ECE = 0.288); the better-calibrated end includes CatBoost (0.238) and Logistic Regression (0.215). Among tree-based models, Random Forest (0.102), LightGBM (0.093), and XGBoost (0.038) are better calibrated, and XGBoost is the best-calibrated tree model out of the box; TabPFN is comparable (ECE = 0.035). Post-hoc calibration (isotonic regression) can further reduce ECE for miscalibrated models. We recommend isotonic regression for deployment. Pre-calibration reliability diagrams for T1 and T4 are shown in Supplementary Fig. 5.

S6: Conformal Prediction Coverage

We applied split conformal prediction to the T1 and T4 classification tasks, using the validation set for calibration and the test set for evaluation. Conformal prediction sets at nominal coverage levels of 90% and 95% were generated. At alpha = 0.05, XGBoost achieves empirical coverage of 0.949 with a mean prediction set size of 1.291 (out of 2 possible classes). At alpha = 0.10, per-model empirical coverage varies, with the linear model showing the most pronounced undercoverage. Split conformal prediction provides finite-sample coverage guarantees under the assumption that calibration and test data are exchangeable (i.e., drawn i.i.d. from the same distribution). Our geographic stratification (using EPA Regions 1, 3, 4, 5, 6 for training, 2, 7 for validation/calibration, and 8, 9, 10 for testing) partially violates this assumption, since calibration and test regions are spatially disjoint with potentially different feature distributions. However, three lines of evidence suggest this violation is modest in practice: (1) the empirical marginal coverage (0.910 at $\alpha = 0.05$, modestly below the 0.95 target) across the test set, (2) the per-region group conformal results below, where most test regions cover near nominal but Region 9 (California) materially under-covers (0.878 against the 0.95 target), and (3) the observation that PFAS contamination drivers (proximity to industrial sites, hydrogeology, land use) are qualitatively similar across US regions even if their distributions differ. Under distribution shift conformal sets can become either conservative or anti-conservative depending on the direction of the shift (Barber et al., 2023, “Conformal prediction beyond exchangeability”). Empirically we observe modest under-coverage rather than overcoverage, so we report these figures as observed coverage, not a delivered guarantee; the prediction sets average 1.328 out of 2 possible classes. For applications requiring stricter guarantees under covariate shift, weighted conformal methods could be applied using density ratio estimation between calibration and test distributions.

Key findings: - Empirical coverage closely matches nominal coverage (within a couple of percentage points) for all model families on T4 - T1 coverage is slightly below nominal for some models (e.g., CatBoost 0.912, LightGBM 0.944 at $\alpha = 0.05$), likely due to the severe class imbalance (~29% positive rate) and finite calibration set size - Conformal sets provide observed (approximate) coverage even for models with miscalibrated probability estimates

Conformal Prediction Coverage

Split conformal prediction provides a **marginal** coverage guarantee over the pooled test set. We report coverage broken out by EPA test region (8, 9, 10) to expose subpopulation behavior, but emphasize that the guarantee is marginal, not per-region: the calibration set comes from the validation regions, so each test region has zero in-region calibration points (n_calibration = 0) and the reliable_guarantee flag is false everywhere. At α = 0.05 (target 95%):

Region	Coverage	Avg Set Size	N
8	0.967	1.398	538
9	0.878	1.310	2,410
10	0.966	1.334	832
Overall (marginal)	**0.910**	**1.328**	**3,780**

Region 9 (Pacific) under-covers (0.878) at every significance level examined, illustrating why per-region distribution-free guarantees cannot be claimed without per-region calibration data. A true Mondrian (per-region) conformal predictor would require carving a calibration slice from each test region, which would change the headline test set; we therefore report marginal coverage and flag the per-region variation rather than over-claiming a regional guarantee.

S7: Sensitivity Analysis

To assess robustness to preprocessing choices, we evaluate T1 (XGBoost) across five NaN-drop thresholds (0.3, 0.4, 0.5, 0.6, 0.7; the fraction of missing values above which a feature column is dropped before imputation) and several proximity buffer-radius variants. All five thresholds produce an identical 135-column feature set with identical performance (AUROC 0.858, AUPRC 0.688): no feature column has a missingness fraction in the tested range, so the threshold does not bind and the model is exactly invariant to it. Restricting proximity features to a single buffer radius leaves performance essentially unchanged, confirming the model does not depend on any single radius choice.

S7b: Coordinate Source Breakdown and Perturbation Sensitivity

Of the 95,223 systems in the dataset, 87,450 are geocoded, most via ZCTA centroids and the remainder from original source coordinates. ZCTA centroid geocoding introduces roughly 5 km of spatial imprecision for a typical system.

To quantify the impact of this imprecision on model performance, we added uniform random noise (1, 5, 10 km) to all system coordinates and re-ran T1 XGBoost (5 seeds per perturbation level). Performance is robust: at 5-km perturbation both AUROC and AUPRC are essentially unchanged, and proximity features use 5–25 km buffers that are insensitive to small coordinate shifts (see paper/tables/table_coordinate_sensitivity.md). Extending the perturbation to the empirical error tail (coordinate_tail_sensitivity.json, magnitudes to 270 km, the upper tail of the geocoding-error distribution) shows no monotone degradation: test AUROC is 0.808 unperturbed and 0.820 at 270 km, flat within run-to-run noise. The environmental-feature signal is therefore not an artifact of precise coordinates: it survives tail-magnitude perturbation, so the measurement-precision asymmetry between exact monitoring features and imprecise environmental features does not, by itself, explain the environmental features' limited contribution.

The perturbation analyses above address random imprecision but not systematic mislocation. For a subset of systems the harmonized coordinate derives from an out-of-state mailing- or

operator-address ZIP code, which places the system deep inside a foreign EPA region. We flag every system whose PWSID-prefix EPA region disagrees with its coordinate-derived region, judging each coordinate against US Census cartographic state boundary polygons (a point maps to the state whose polygon covers it, or to the nearest state within a 3.0-degree tolerance for water-jittered centroids that no shoreline-clipped polygon covers): 1,818 of the 87,450 geocoded systems. The geographic split derives from the PWSID prefix, not the coordinate, so split membership is unaffected; the exposure is limited to wrong-place environmental features for the flagged systems, and these systems are excluded from the Extended Data Fig. 1 split map. To bound the modeling impact we re-ran the T1 and T4 XGBoost benchmarks on the canonical harness with all flagged systems removed end to end (training and evaluation): T1 test AUROC moves from 0.864 to 0.866 and T4 from 0.699 to 0.697 (frozen misgeocode_sensitivity_v2.json), so the headline results do not depend on the mis-geocoded systems.

S8: Evaluation Protocol Ablation

To quantify the impact of evaluation protocol on reported performance, we compared random 5-fold cross-validation against geographic stratification using a baseline proximity/demographic feature set comparable to those used in prior PFAS prediction studies (Hu et al. 2016, Fernandez et al. 2023, Tokranov et al. 2024).

Key findings: - Under random CV, XGBoost achieves AUROC 0.869 on the baseline feature set; under geographic holdout, it drops to 0.699 - A size-matched random control, with each fold's training set stratified-subsampled to the geographic training-set size (n = 7,930), reproduces the random-CV result, so the gap is an evaluation-protocol effect, not a training-set-size effect - The two evaluation sets differ in base rate (geographic test prevalence 0.285 versus 0.215 in the stratified random folds, pooled rate). The geographic set has the higher rate, so the prevalence asymmetry biases the AUPRC comparison against the leakage claim rather than inflating it. The prevalence-independent AUROC contrast is therefore the main-text headline (frozen split_prevalence.json) (Supplementary Table 1) - The direction is consistent across all nine model × feature-set cells (Extended Data Table 4) on AUROC: the geographic split scores below random CV on AUROC in every cell (two logistic-regression cells reverse on AUPRC, a prevalence artifact that biases against the leakage claim), with AUPRC inflation of up to 58%

The full feature set × split strategy comparison is available in paper/tables/table_brennan_comparison.md, and the random-versus-geographic performance is shown in Supplementary Fig. 6.

Supplementary Table 1: Size-matched random-split control

Random 5-fold CV with each fold's training set stratified-subsampled to the geographic training-set size (n = 7,930), for all nine model × feature-set cells of the split comparison. AUPRC inflation relative to the geographic split persists with and without size matching, ruling out the random arm's larger training set as the driver of the inflation.

See paper/tables/table_supp_split_sizematched.md for full results.

S9: Spatial Autocorrelation

Moran's I test for spatial autocorrelation in model residuals was performed using inverse-distance spatial weights over the k=10 nearest neighbors. Significant positive autocorrelation ($I > 0$, $p < 0.01$) was detected in residuals of all models on both T1 and T4, indicating that model errors are spatially clustered. For the headline XGBoost T1 model, residual Moran's I is 0.212 at 50 km, declining to 0.077 at 200 km; positive autocorrelation is present across all models (spatial_autocorrelation.json).

This finding justifies the use of geographic stratification for train/test splitting. It also means the i.i.d. bootstrap confidence intervals reported elsewhere are approximate, because residual errors are not independent.

Region-block bootstrap of the LORO headline

To check that the residual autocorrelation does not materially understate uncertainty in the headline LORO estimate, we re-estimated the T1 XGBoost LORO mean AUROC with a region-block bootstrap that resamples the ten EPA regions (the spatial-clustering scale) with replacement, recomputing the sample-size-weighted mean each iteration (10,000 iterations; spatial_block_bootstrap.json). The block-bootstrap 95% interval is [0.705, 0.860], modestly wider than the naive across-fold normal interval but qualitatively unchanged: the headline remains well above chance. Accounting for spatial clustering widens the interval modestly rather than overturning the result.

Buffered-boundary leave-one-region-out

A related concern is that systems straddling EPA-region seams could leak information across the held-out boundary. We re-ran the LORO sweep over all 10 EPA regions after excluding every training system within 50 km (EPSG:5070) of the held-out region (829–1,685 systems excluded per fold; loro_cv_buffered.json), with imputation aligned to the primary train-only path (an earlier three-region variant of this check imputed on the full dataset before subsetting and is superseded). Buffering reduces the unweighted provenance-reduced LORO mean modestly, from 0.694 to 0.661 (with-provenance 0.752), far from collapsing it: region-seam proximity contributes marginally to the estimate but does not drive the transportable signal.

S10: Software Versions

All experiments were run with the following software stack. Exact versions are recorded in results/software_versions.json during each pipeline run.

Package	Version
Python	3.10+
NumPy	1.24+
pandas	2.0+
scikit-learn	1.3+
XGBoost	2.0+
LightGBM	4.0+
CatBoost	1.2+
PyTorch	2.4+
GeoPandas	0.14+
SHAP	0.44+
Optuna	3.4+

Full environment specification: environment.yml (conda) and pyproject.toml (pip).

S11: Multi-Seed Stability Analysis

To verify that benchmark results are not artifacts of a single random seed, we evaluated T1 (PFAS detection) and T4 (heavy metal prediction) across five random seeds (42, 123, 456, 789, 2024) with three model families: XGBoost, CatBoost, and Logistic Regression. Each seed controls random initialization of model training and bootstrap sampling. For tree-based models, the training set size (7,930 systems for T1, 51,283 systems for T4) is sufficiently large that stochastic variation is minimal.

Results confirm moderate stability for T1 and high stability for T4. For T1, AUROC standard deviation across seeds is 0.003 (XGBoost) and 0.005 (CatBoost); for T4, standard deviation is negligible for all models. AUPRC standard deviation is likewise small, with T1 CatBoost at 0.006. Logistic Regression is fully deterministic (zero variance). The full seed-by-seed results are saved to results/multi_seed_stability.json.

Seed Inflation Check

To assess whether reporting a single seed (seed=42) inflates metrics relative to the multi-seed distribution, we computed z-scores: z = (reported − mean) / std for each task/model. The reported seed-42 headline metrics (Table 2) come from the full benchmark pipeline, whereas the multi-seed distribution is produced by a streamlined single-model stability harness. After correcting a region- assignment defect that had caused the two paths to evaluate different test populations (Methods; ~605 geocoded systems were previously dropped from the streamlined harness), the streamlined single-model harness runs modestly *below* the full benchmark rather than above it, so it does not inflate reported skill: for both T1 XGBoost and CatBoost the streamlined single-model harness runs modestly below the full benchmark (the streamlined harness omits the ensemble averaging and part of the feature set). Because the paper's honest out-of-region headline (LORO) uses XGBoost within a single harness, this cross-harness difference does not affect it. *Within* a fixed harness, seed-to-seed variability is small: the maximum across-seed optimism for any single model is 0.005 AUROC. T4 is near-deterministic across seeds, and Logistic Regression is fully deterministic. Full results are in results/seed_inflation_check.json.

Default-Hyperparameter Stability

Table 2 in the main text reports default (non-tuned) configurations at seed 42 for reproducibility; this subsection characterizes variability under those default configurations across seeds.

For T1, XGBoost and CatBoost show small across-seed AUROC s.d., confirming that seed-to-seed variability within a fixed harness is modest compared to the much larger differences between top tree models and neural networks. For T4, variability is negligible for all models, reflecting the stronger and more consistent signal in heavy metal prediction.

Supplementary Table 2: Multi-seed stability

See paper/tables/table_supp_multi_seed.csv for per-model, per-task mean +/- SD across five seeds.

S12: Per-Region Heterogeneity Analysis

LORO cross-validation reveals substantial variation in per-region AUROC for T1. To understand the sources of this heterogeneity, we analyzed per-region PFAS detection rates, feature distributions, and missing data patterns.

Region 4 (Southeast) underperforms with the lowest LORO AUROC, while Region 3 (Mid-Atlantic) is the strongest mainland region. Kolmogorov-Smirnov tests on the top SHAP features show significant distributional shifts between these best- and worst-performing regions for

wetland fraction (KS = 0.308, FDR p < 0.001) and monitoring intensity (n_samples; KS = 0.065, FDR p < 0.05); the data-source missingness indicators do not differ significantly. Region 4 also has higher missing rates for hydrogeological features due to sparser aquifer mapping coverage, reducing the discriminative signal available to environmental features.

These findings imply that practitioners deploying AquaContam models should expect lower performance in regions with fewer industrial contamination sources and should consider region-specific calibration. Full results are in results/region_heterogeneity.json.

S13: Deep Tobit Architecture

The Deep Tobit model is a censoring-aware neural network that explicitly models left-censored observations common in water quality data. The architecture is a 3-layer MLP (128-64-32 hidden units) with ReLU activations and dropout (0.3), identical to the standard MLP baseline. The key difference is the loss function: instead of binary cross-entropy, Deep Tobit uses a Tobit likelihood loss:

$$L = -\Sigma\ [d_i \cdot \log \varphi((y_i - \mu_i)/\sigma) - d_i \cdot \log \sigma + (1-d_i) \cdot \log \Phi((c_i - \mu_i)/\sigma)]$$

where d_i = 1 for detected (uncensored) samples, y_i is the observed concentration, c_i is the detection limit, μ_i is the predicted mean, σ is the learned noise scale, and φ/Φ are the standard normal PDF/CDF.

For binary classification tasks, the predicted latent concentration is compared against the detection limit: P(detected) = 1 - Φ((c - μ)/σ). The classification target is obtained by passing continuous concentration values (not binary labels) to the Tobit loss via _fit_extra kwargs, so the network learns the true concentration surface and derives detection probability from it. This yields T1 AUROC 0.602 (Table 2), well below the tree-based models, indicating that the censoring-aware loss does not competitively transfer to binary detection under the expanded dataset with geographic evaluation. The implementation includes gradient clipping, cosine learning rate scheduling, clamped log-sigma, and numerically stable truncated-mean prediction with asymptotic approximation for extreme z-values. For regression (T2), a log1p transform stabilizes the heavily skewed concentration distribution, and output clamping prevents overflow in the inverse Mills ratio. Despite modest T1 classification performance (AUROC 0.602), Deep Tobit achieves a T5 transfer AUROC of 0.729, the highest of any model family. The disconnect between T1 and T5 performance suggests that the censoring-aware loss captures some environmental signal relevant to cross-contaminant transfer, even when within-domain binary classification degrades.

S13b: Zero-Inflated Censored Regression Architectures

Three additional model families address the zero-inflated, left-censored structure of T2 concentration data (97% censored). Each decomposes the prediction problem differently, treating structural zeros and censored observations as distinct phenomena.

Hurdle (XGBoost two-part model). A two-stage decomposition separating the zero process from the positive-value process. Stage 1 (gate): an XGBoost binary classifier estimates P(detected) trained on all systems. Stage 2 (intensity): an XGBoost regressor estimates E[Y | detected] trained only on the ~3% detected subset, operating in log-space. The combined prediction is E[Y] = P(detected) × E[Y | detected]. Back-transformation from log-space uses the Duan (1983) smearing estimator to correct for retransformation bias, computing the empirical mean of exponentiated training residuals as the correction factor. This avoids the systematic underestimation inherent in naïve exponentiation of log-scale predictions.

XGBoost AFT (Accelerated Failure Time). Uses XGBoost's native survival:aft objective with interval-censored encoding to provide statistically proper left-censoring treatment. Detected

samples are encoded as point observations [log1p(y), log1p(y)], while censored samples are encoded as left-censored intervals [ε, log1p(DL)], where DL is the detection limit and ε is a small positive constant. The model estimates the conditional survival function S(t | X) via XGBoost's DMatrix label_lower_bound and label_upper_bound interface. Point predictions are obtained from the estimated log-normal location parameter. This approach respects the censoring mechanism without imputation or substitution of non-detects.

Zero-Inflated Deep Tobit (ZI-Tobit). A deep neural network with three output heads on a shared hidden trunk (two hidden layers, ReLU activations, dropout, batch normalization). The gate head produces P(structural_zero) via a sigmoid activation, distinguishing true zeros from censored observations. The μ head estimates the latent mean concentration. The log-σ head estimates the log-scale parameter with clamping for numerical stability. The loss function is a zero-inflated Tobit negative log-likelihood:

$$L = -\Sigma\,[z_i \cdot \log(\pi_i) + (1-z_i) \cdot \log(1-\pi_i) + (1-z_i) \cdot L\_Tobit(y_i, \mu_i, \sigma_i)]$$

where π_i = P(structural_zero), z_i indicates structural zeros, and L_Tobit is the standard Tobit log-likelihood from S13. A log-sum-exp trick ensures numerical stability when combining the zero-inflation and Tobit components.

Hurdle+AFT Ensemble. A simple average of the Hurdle and XGBoost AFT predictions, combining the two-part decomposition with the survival-based approach. This ensemble provides a complementary aggregation of structurally different censoring treatments without additional hyperparameter tuning.

S14: DML Adjusted Association Methodology and Results

To move beyond correlational feature importance (SHAP) toward adjusted estimates, we apply double machine learning (DML) to estimate the adjusted effect of each feature on PFAS detection probability, controlling for a pre-specified set of monitoring and system-size confounders (monitoring intensity n_samples, population served, log population served, and mean detection limit).

Algorithm

For each feature X_j:

1. **Cross-fitting**: Split data into K=5 folds (pooled KFold(shuffle=False), used only to avoid own-fold overfitting in the nuisance step, not as a generalization split)
2. **Nuisance estimation**: In each fold, train gradient-boosted models to predict (a) the outcome Y from the confounder set W, and (b) X_j from W
3. **Residualize**: Compute residuals $\tilde{Y} = Y - E[Y|W]$ and $\tilde{X}_j = X_j - E[X_j|W]$
4. **Adjusted estimate**: Regress $\tilde{Y}$ on $\tilde{X}_j$; the coefficient is the partially-linear DML estimate of X_j's association net of W

This procedure removes confounding from the monitoring/size confounder set W, yielding the association of X_j net of monitoring intensity rather than net of all other features (the estimand is "adjusted for monitoring", which is what the code residualizes against).

Key Results

- **Adjusted AUROC**: 0.729 (vs. original 0.835); ~13% of discrimination from feature confounding. Both are computed under the pooled 5-fold cross-fitting above, not the geographic holdout, so 0.835 is an in-sample pooled value distinct from the 0.864

geographic-split headline; the pair is a relative decomposition of the discrimination attributable to feature confounding, not a generalization estimate

- **Significant coefficients**: 69 of 130 features are significant after Benjamini-Hochberg FDR correction (p_FDR < 0.05; 59 at p_FDR < 0.01)
- **First-stage strength**: the treatment-residualization nuisance model has a negative cross-fitted R^2 for 109 of 130 features (it predicts them worse than their mean), i.e. most features are near-orthogonal to the monitoring confounders. The adjustment therefore removes little for these features not because it is mis-specified but because there is little monitoring confounding to remove, which strengthens rather than weakens the reading that the retained environmental signal is not a monitoring artifact
- **Largest displacements are environmental**: pct_wetland_5km falls 48 positions (of 80 ranked confounder-orthogonalized features)
- **Demographic features**: pct_less_hs_education is markedly upranked (SHAP rank 76 → DML rank 39) and retains a significant adjusted association; pct_people_of_color also retains a significant adjusted association (standardized coefficient +0.022 per 1-s.d., p_FDR < 0.001), whereas pct_low_income does not (p_FDR = 0.54), indicating its correlational signal is largely monitoring-mediated
- **Proximity features**: Industrial facility counts and Superfund proximity retain the strongest adjusted effects (p_FDR < 0.001); airport, landfill, and WWTP distances are also significant (p_FDR < 0.05), confirming mechanistic relevance
- **Monitoring intensity** (n_samples): SHAP importance rank 1, but smaller adjusted effect, consistent with confounding rather than direct causation

Limitations

DML assumes a partially linear model and no unmeasured confounders, both strong assumptions. Rare features (e.g., one-hot aquifer types with <100 systems) may yield unstable adjusted estimates. We report standard errors and p-values to flag unreliable estimates. The adjusted AUROC should be interpreted as a lower bound on genuine predictive signal.

Supplementary Table 3: DML adjusted association results

Top 15 features ranked by absolute DML adjusted effect. For each feature, the table reports SHAP importance (correlational), DML adjusted effect, standard error, p-value, and feature ranks in each method. Socioeconomic features show large rank displacements between DML and SHAP (e.g., pct_less_hs_education moves from SHAP rank 76 to DML rank 39), indicating genuine environmental risk pathways underattributed by correlational analysis. Original AUROC: 0.835; adjusted AUROC: 0.729 (~13% of discrimination from feature confounding). Coefficients are standardized (per 1 s.d.) so that rankings and sensitivity bounds are scale-invariant.

Feature	SHAP Importance	Causal Effect	Std Error	p-value	p-value (FDR)	DML Rank	SHAP Rank
aquifer_type_California Coastal Basin aquifers	0	0.0469	0.0034	0	0	—	—
aquifer_type_Northern Atlantic Coastal Plain	0.0128	-0.0441	0.0037	0	0	1	19

Feature	SHAP Importance	Causal Effect	Std Error	p-value	p-value (FDR)	DML Rank	SHAP Rank
aquifer system							
aquifer_type_Basin and Range basin-fill aquifers	0	-0.0391	0.0031	0	0	—	—
aquifer_type_Biscayne aquifer	0.043	0.0342	0.0033	0	0	2	4
aquifer_type_Early Mesozoic basin aquifers	0.0188	0.0337	0.0036	0	0	3	7
n_landfill_10000m	0.0085	0.0312	0.0036	0	0	4	42
prox_hazardous_waste	0.0072	0.0307	0.003	0	0	5	55
n_industrial_10000m	0.0086	0.0284	0.0041	0	1e-10	6	38
pct_developed_1km	0.0063	0.0239	0.0029	0	0	7	70
aquifer_type_Piedmont and Blue Ridge crystalline-rock aquifers	0.0214	0.0237	0.0036	0	2e-10	8	6
nlcd_majority_class_developed	0	0.0236	0.0031	0	0	—	—
aquifer_type_Central Valley aquifer system	0	0.0233	0.0031	0	0	—	—
nlcd_majority_class_agriculture	0.0053	-0.0232	0.0024	0	0	9	78
aquifer_type_Floridan aquifer system	0.0183	0.0224	0.0037	1e-09	5.3e-09	10	8
n_industrial_5000m	0.007	0.0218	0.0049	9.13e-06	2.89e-05	11	60

Original AUROC: 0.835, Adjusted AUROC: 0.729 Spearman rho = 0.24 across 80 features

Grouped Permutation Test for Category-Level Rank Displacements

The aggregate Spearman rank correlation between DML and SHAP is modest but significant ($\rho = 0.24$, $p = 0.032$), and we further tested whether individual feature categories show significantly larger mean absolute rank displacements than expected under random category assignment.

Method. For each of 5 feature categories (proximity n = 14, land use n = 22, hydrogeology n = 13, demographics n = 5, and other n = 23), we computed the observed mean absolute displacement (|SHAP rank − DML rank|). Monitoring intensity and system characteristics

features were not ranked because they serve as confounders in the DML analysis and are orthogonalized out. We generated a null distribution by permuting category labels across the ranked features (10,000 permutations) and computing the same per-category mean. The one-sided p-value is (count of null ≥ observed + 1) / (N + 1). P-values are FDR-corrected across categories using Benjamini-Hochberg.

Results. No feature category reaches significance after FDR correction: across the five categories (land use, demographics, proximity, hydrogeology, and other), mean absolute rank displacements are modest and similar, and every category's FDR-corrected permutation p-value is far from significance (dml_shap_rank_comparison.json).

The non-significance reflects the small number of features per category (especially demographics, n = 5) rather than the absence of category-level patterns. With only five socioeconomic features, even a sizeable mean rank displacement does not consistently exceed what random 5-feature subsets achieve by chance. The evidence for socioeconomic rank elevation therefore rests on the individual-feature FDR-corrected DML coefficients (69/130 significant) and the significant aggregate correlation, not on category-level permutation tests.

See results/category_displacement_test.csv for full results.

Spatially-aware permutation of the equity significance tests (M8b)

The headline monitoring-inequity ratios and the per-region burden significances were originally assessed with i.i.d. label-shuffle permutations, which ignore spatial autocorrelation and can be anti-conservative. We re-tested both under spatial nulls (spatial_permutation.json, 10,000 permutations). For the national monitoring-intensity ratios we permuted the demographic values only WITHIN EPA regions (stratified permutation), removing the between-region component from the null; the people-of-color sampling disparity (ratio 1.85x) remains significant, $p < 0.001$, and the low-income under-sampling likewise persists. For the per-region burden significances, because the frozen per-region burdens use held-out per-fold imputation that a single global-imputation assembly does not reproduce exactly, we compared the naive label shuffle against a spatial ROTATION null (circular shift over within-region k-means spatial-cluster order) on ONE common assembly, a valid comparison of the two permutation methods. On that assembly 5 regions are FDR-significant under the naive null but only 3 survive the spatial null, confirming that the naive per-region test is mildly anti-conservative and motivating the softened claim in the main text.

S15: Supplementary Figures

Supplementary Fig. 1: Cross-contaminant transfer results

Transfer learning results for T5 (lead-to-PFOS transfer). The Deep Tobit classifier achieves the highest transfer AUROC (0.729), superficially comparable to within-domain T1 models. However, ablation of system characteristics reduces XGBoost AUROC substantially toward chance for this negative-class-dominated task, demonstrating that shared monitoring patterns largely mediate the apparent cross-contaminant transfer. The residual signal above baseline suggests modest genuine geospatial commonality, but headline transfer numbers should not be interpreted as evidence of transferable environmental risk without proper ablation.

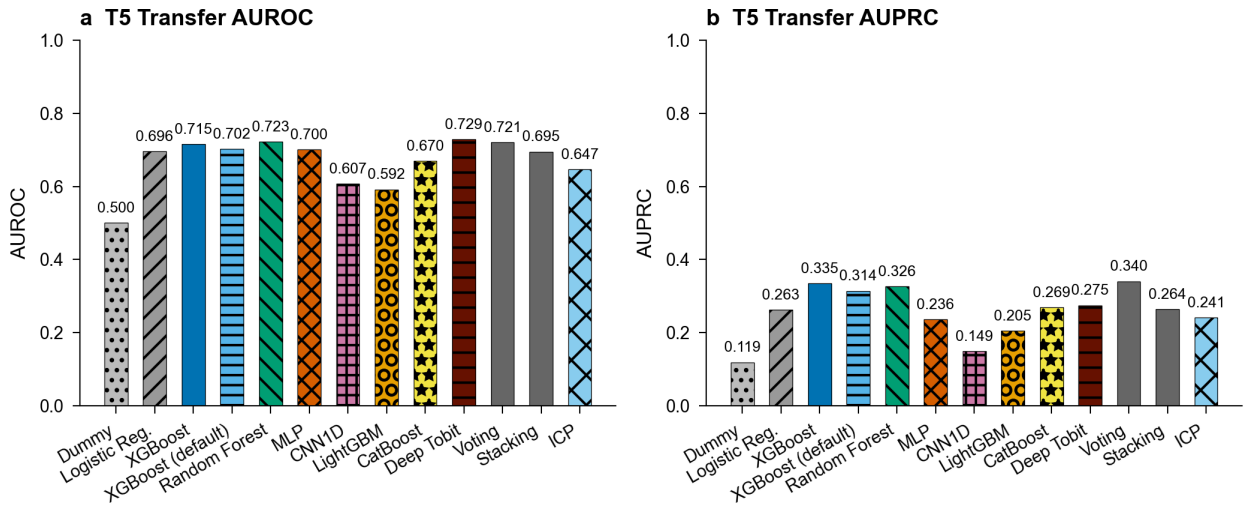

Supplementary Fig. 1

Supplementary Fig. 2: Temporal prediction performance

T7 temporal prediction results (UCMR3-to-UCMR5). XGBoost achieves the best AUROC of 0.664 (with TabPFN close behind). Analysis by system persistence reveals better performance on persistent systems (monitored in both periods) than newly monitored systems, suggesting historical monitoring features provide additional predictive signal.

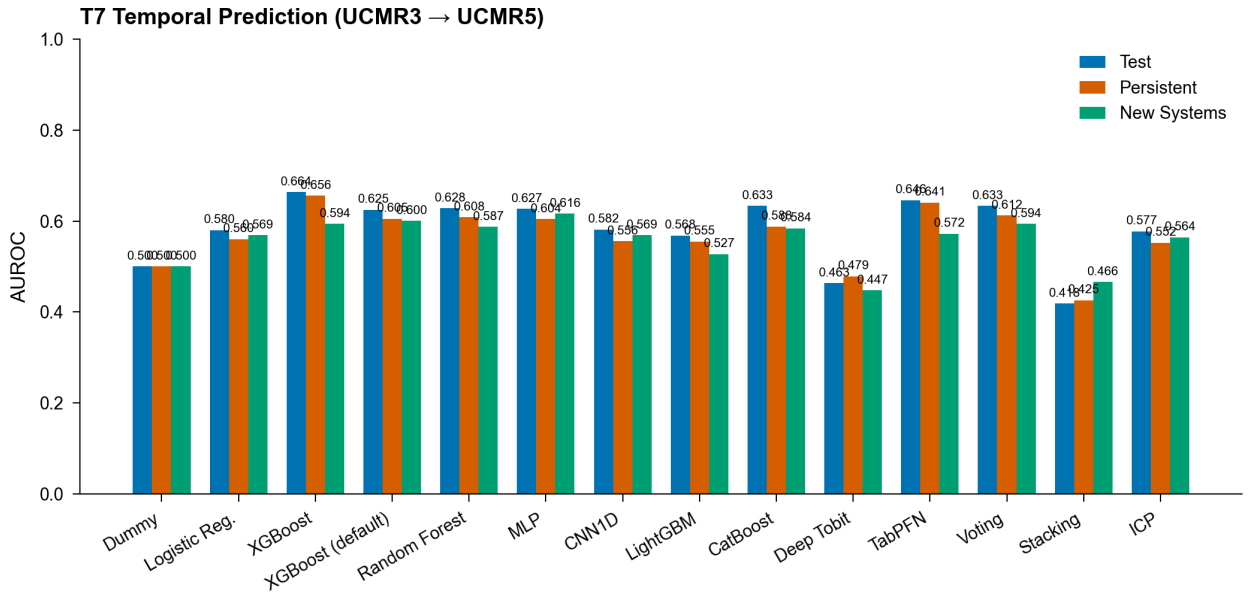

Supplementary Fig. 2

Supplementary Fig. 3: Complete feature correlation matrix

Pearson correlation matrix of the top 30 features (by variance) used in the AquaContam benchmark. Features are grouped by category: proximity, hydrogeology, land use, and demographics. Strong correlations between aquifer type indicators reflect mutually exclusive one-hot categories. Moderate positive correlations between facility proximity features and developed land use fractions are consistent with industrial co-location in urbanized areas.

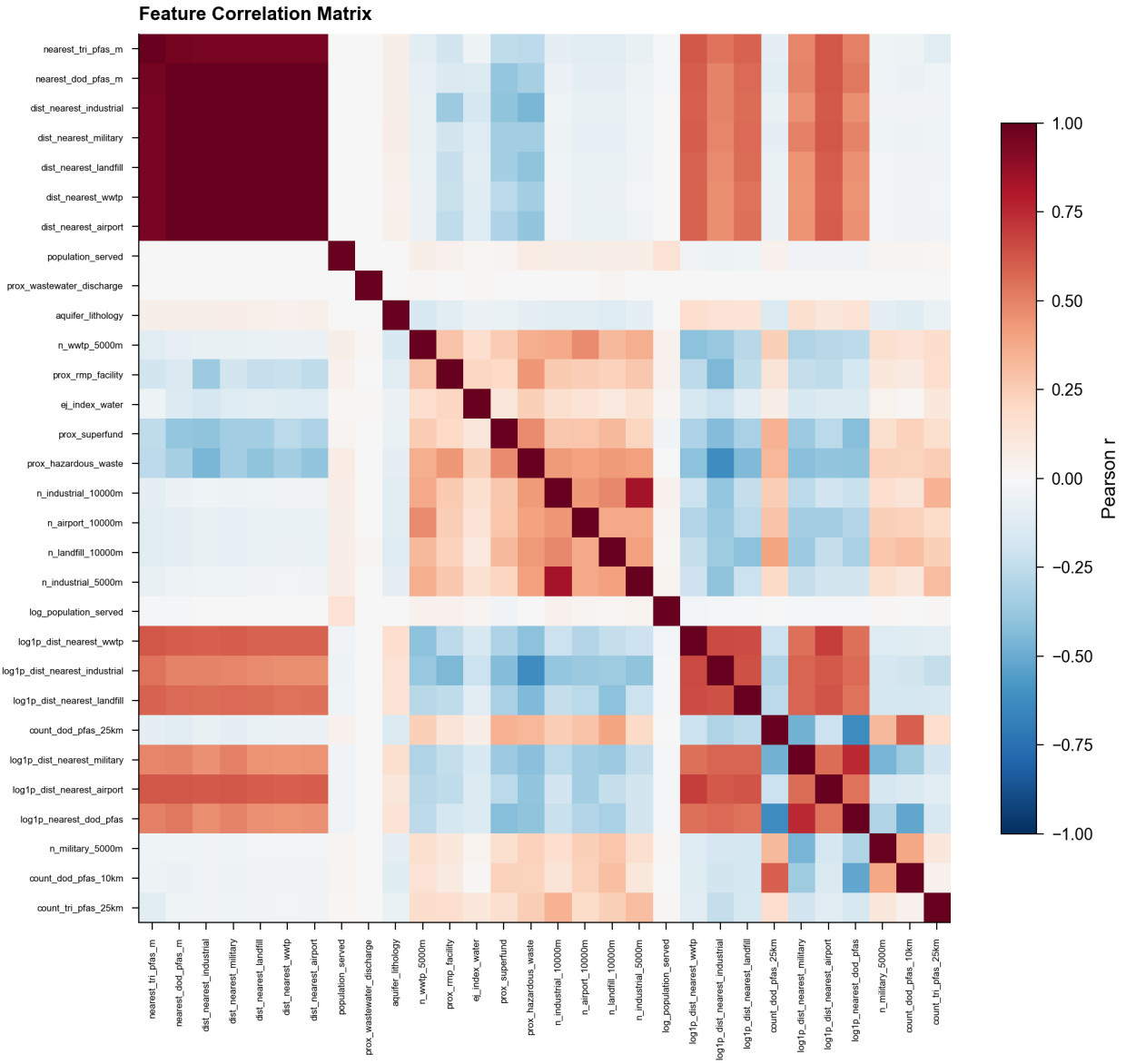

Supplementary Fig. 3

Supplementary Fig. 4: Per-analyte AUROC

Per-analyte AUROC for the T3 multi-PFAS profiling task across all model families (grouped bars, one group per analyte). The five target analytes vary substantially in prediction difficulty: PFOA is the most predictable, PFBS is markedly harder, and HFPO-DA is not evaluable because the geographic test regions (8, 9, 10) contain no HFPO-DA detections, leaving AUROC undefined (annotated in the figure).

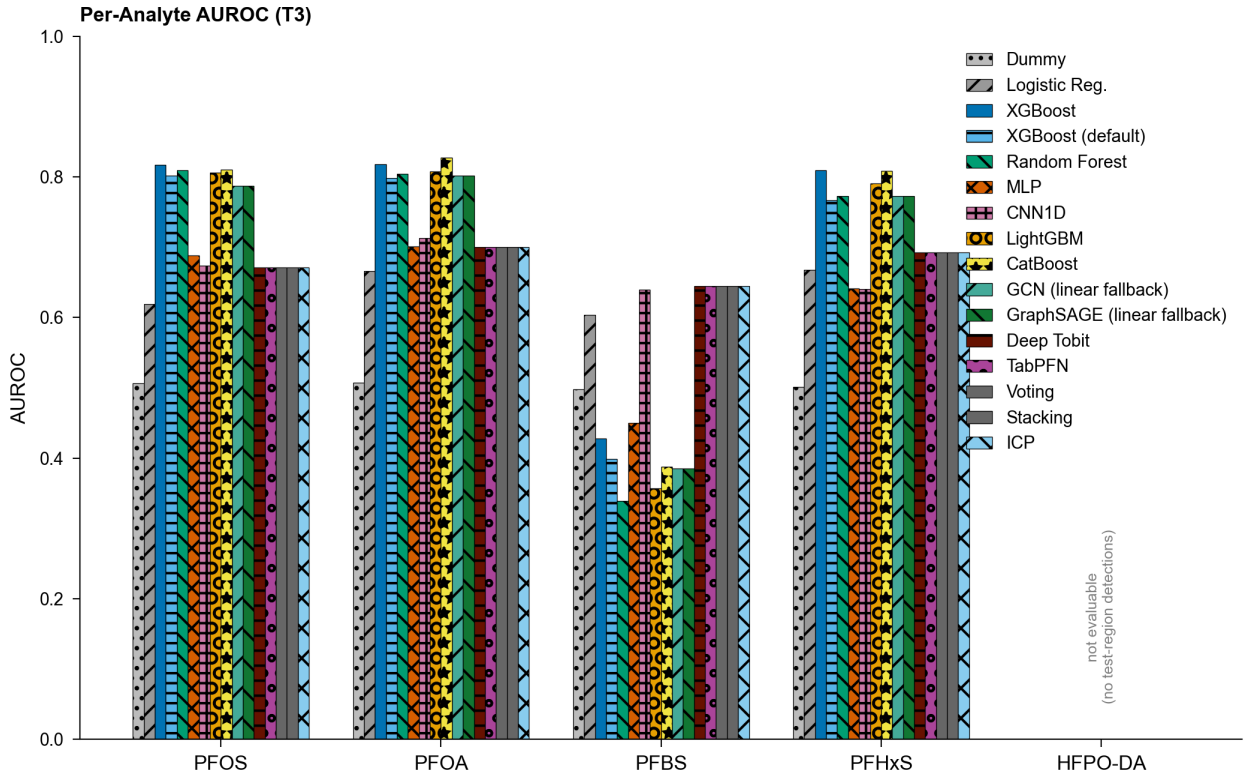

Supplementary Fig. 4

Supplementary Fig. 5: Reliability diagrams

Reliability diagrams for (a) T1 PFAS detection and (b) T4 lead action-level exceedance across model families (see Supplementary S5). Each curve plots the observed fraction of positives against the mean predicted probability per probability bin; models on the diagonal are perfectly calibrated, with deviations below or above the diagonal indicating over- or under-confidence. Expected calibration error (ECE) for each model is shown in the legend.

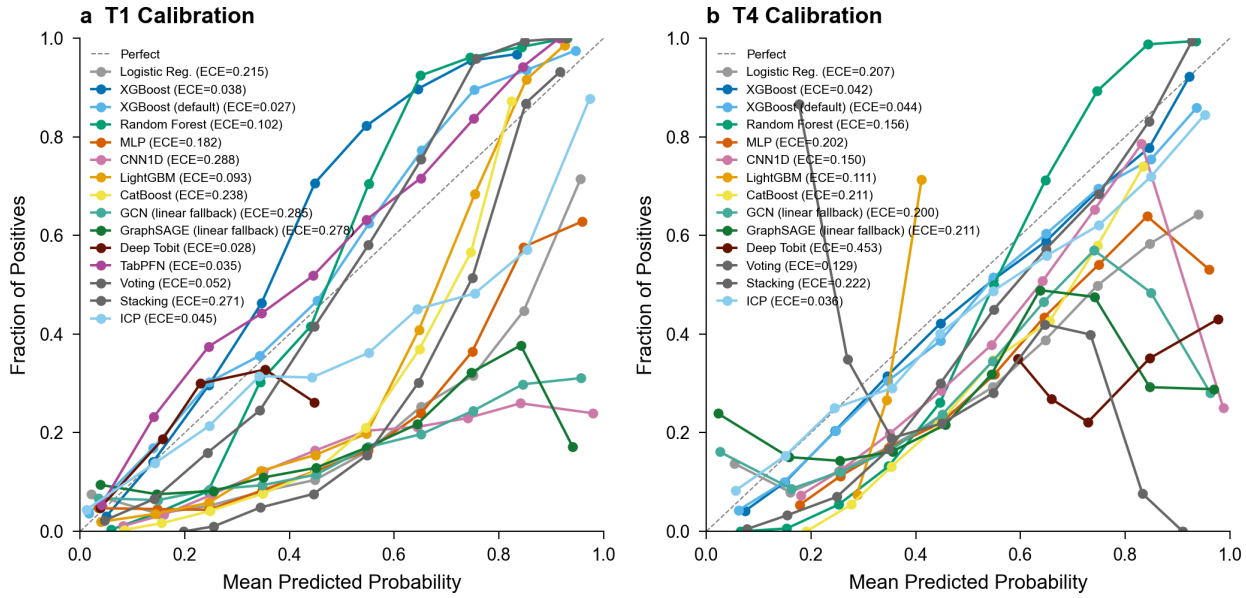

Supplementary Fig. 5

Supplementary Fig. 6: Evaluation protocol comparison

Performance comparison using a baseline proximity/demographic feature set under both random and geographic evaluation protocols (see Supplementary S8). Under random CV, XGBoost achieves AUROC 0.869 with the baseline feature set; under geographic holdout, performance drops to 0.699, demonstrating that evaluation protocol, not model or feature differences, drives the gap.

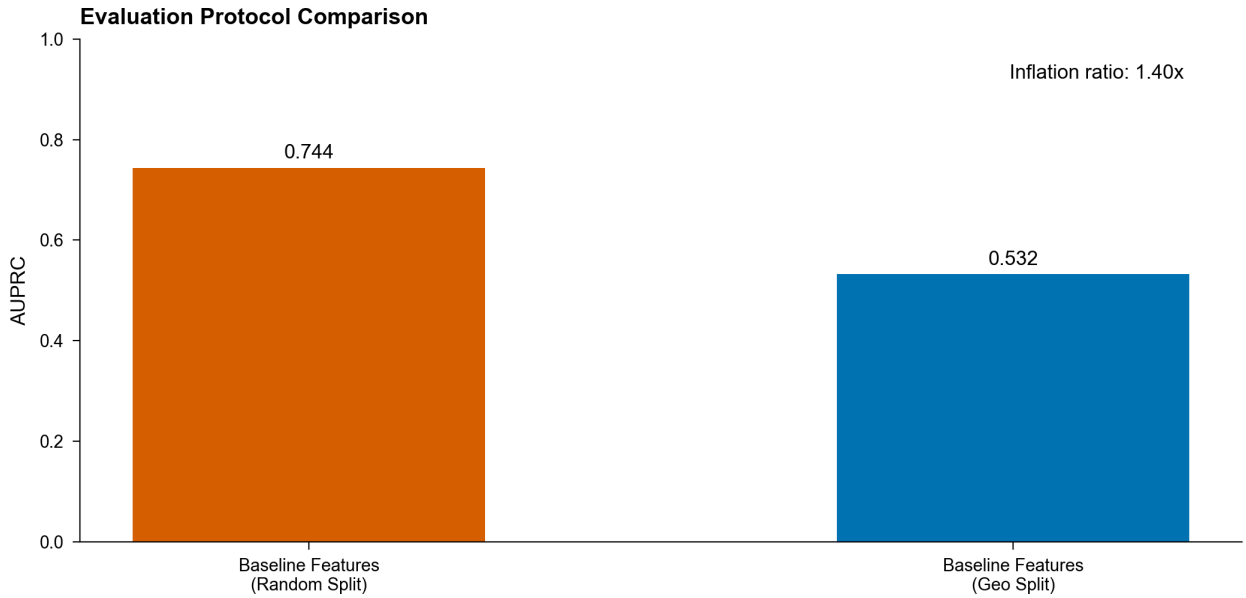

Supplementary Fig. 6

Supplementary Fig. 7: AUROC and AUPRC by model for T1 and T4

Per-model test-set AUROC and AUPRC summary bars for T1 (PFAS binary detection) and T4 (heavy metal prediction) across all model families, regenerated from the frozen benchmark metrics (the frozen archive deliberately strips per-system prediction arrays, so ROC/PR curves are not reconstructable from tracked inputs; see Code Availability). The divergence between AUROC and AUPRC underscores why AUPRC is the primary benchmark metric for imbalanced water quality classification. (Relocated from Extended Data to stay within the ten-item Extended Data limit.)

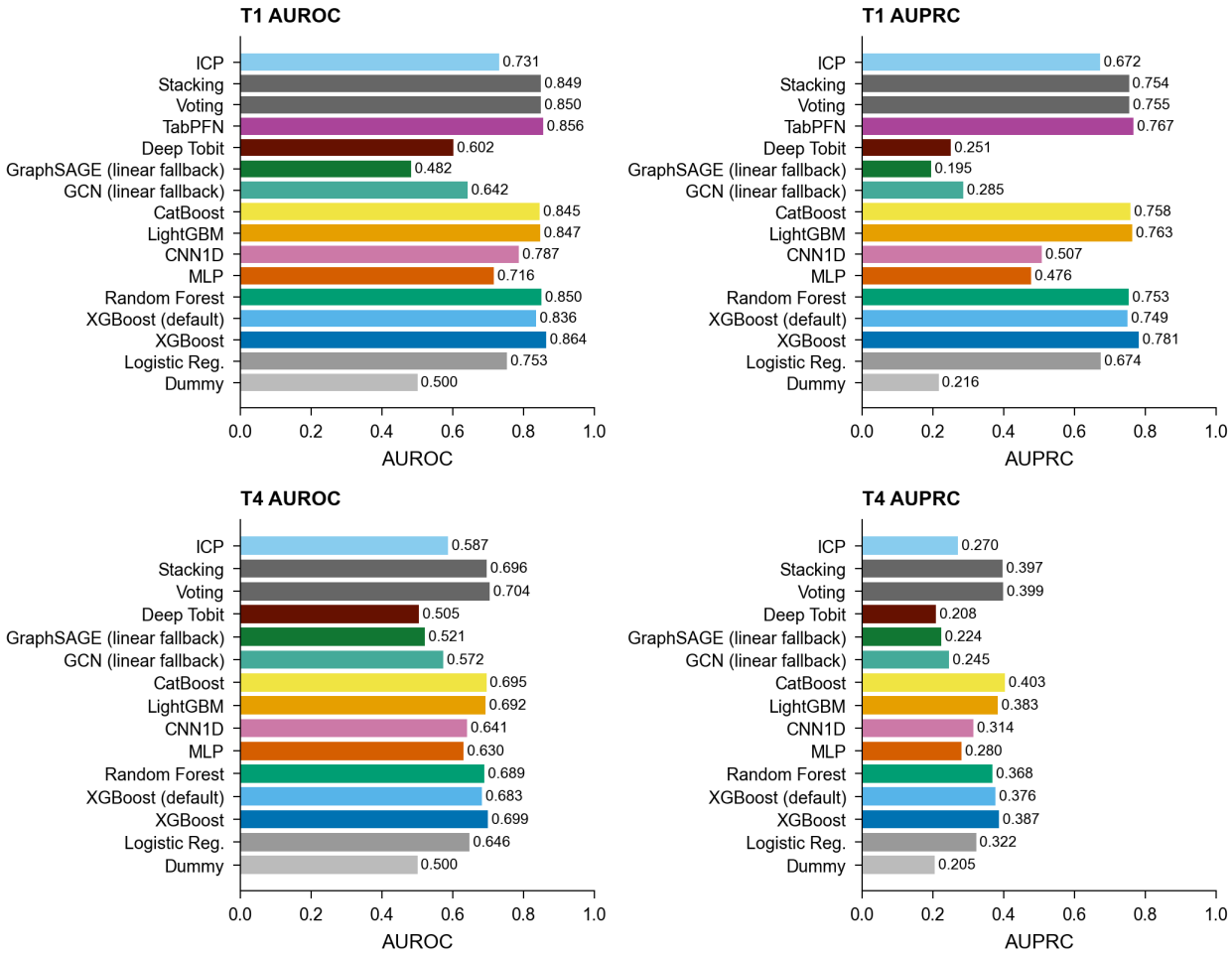

Supplementary Fig. 7

Supplementary Fig. 8: Data distribution and contamination patterns

Distribution of PFAS detection rates across analytes and monitoring periods. UCMR5 exhibits 97.1% overall censoring, with individual analyte detection rates in the low single digits (highest for PFOS). UCMR3 shows 76.4% censoring with higher detection limits. Heavy metal detection rates from SDWIS are substantially higher. Concentration distributions for detected samples are right-skewed across all contaminant classes. (Relocated from Extended Data.)

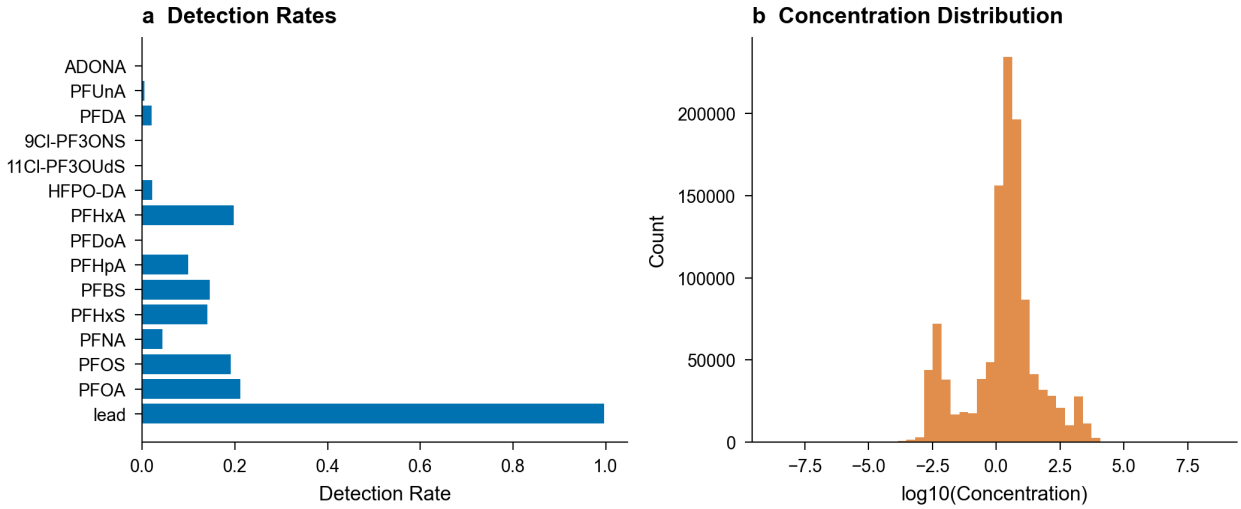

Supplementary Fig. 8

Supplementary Fig. 9: National PFAS (PFOS) risk surface

Predicted T1 PFOS detection risk for 15,268 public water systems across the contiguous United States (XGBoost national inference; quantile-based color scale). This is the same per-system risk surface served by the interactive risk-screening web application (Code Availability), regenerated from the slim prediction export in the frozen archive (predictions_slim.json). Risk scores support monitoring prioritization within the monitored population and inherit the transportability limits quantified in the main text (out-of-region performance, Table 2); systems plotted here include mis-geocoded coordinates discussed in Supplementary S7b.

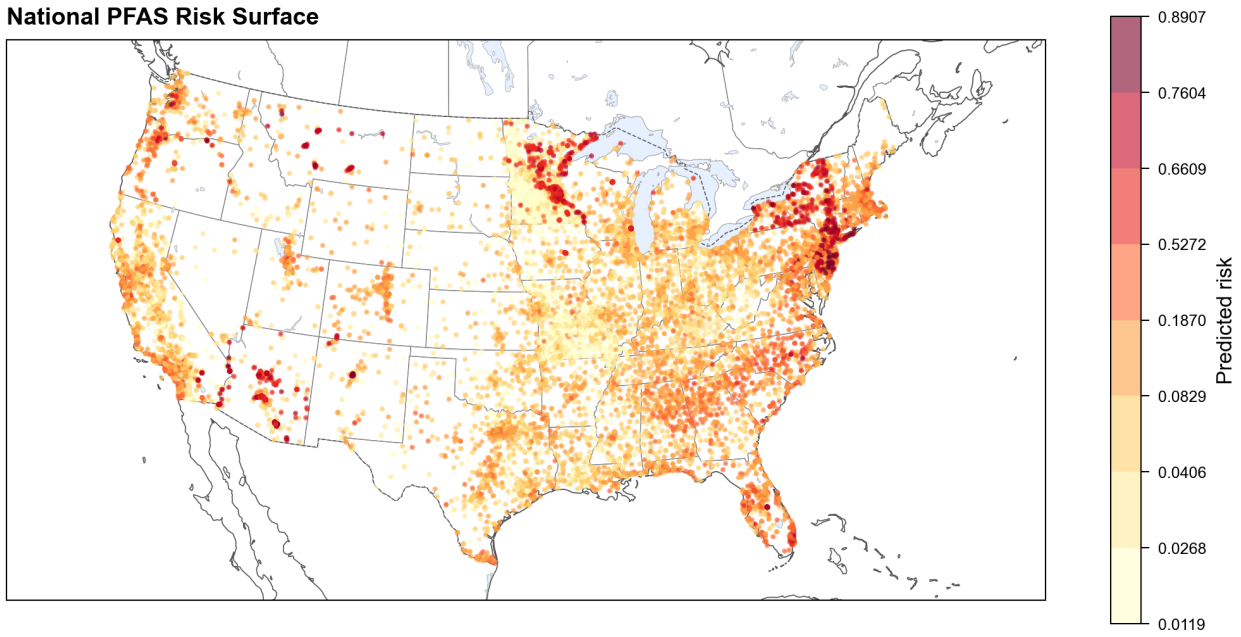

Supplementary Fig. 9

S16: Supplementary Tables (Relocated from Extended Data)

Supplementary Table 4: Benchmark results by task (representative analyte)

Benchmark results for the classification tasks and model families, one row per model-task pair with each task's representative target analyte (e.g., PFOS for T1). The table reports AUROC, AUPRC, F1, precision, and recall, plus macro-averaged AUROC and AUPRC for the T3 multilabel task. The genuine per-analyte disaggregation is Supplementary Fig. 4 (T3 per-analyte AUROC); per-label, micro-averaged, and regression-task (T2) metrics are provided in the accompanying CSV.

Model	Task	Analyte	auroc	auprc	f1	precision	recall	macro _auprc
dummy_classifier	T1	PFOS	0.5	0.216	0	0	0	
logistic_regression	T1	PFOS	0.753	0.674	0.576	0.551	0.603	
xgboost_classifier	T1	PFOS	0.864	0.781	0.682	0.981	0.523	
xgboost_default	T1	PFOS	0.836	0.749	0.67	0.869	0.545	
random_forest_classifier	T1	PFOS	0.85	0.753	0.637	0.767	0.545	
mlp_classifier	T1	PFOS	0.716	0.476	0.525	0.458	0.615	
cnn1d_classifier	T1	PFOS	0.787	0.507	0.474	0.339	0.788	
lightgbm_classifier	T1	PFOS	0.847	0.763	0.625	0.581	0.677	
catboost_classifier	T1	PFOS	0.845	0.758	0.534	0.402	0.792	
gnn_gcn_classifier	T1	PFOS	0.642	0.285	0.486	0.405	0.609	
gnn_sage_classifier	T1	PFOS	0.482	0.195	0.12	0.108	0.134	
deep_tobit_classifier	T1	PFOS	0.602	0.251	0	0	0	
tabpfn_classifier	T1	PFOS	0.856	0.767	0.674	0.943	0.525	
voting_ensemble	T1	PFOS	0.85	0.755	0.654	0.801	0.553	
stacking_ensemble	T1	PFOS	0.849	0.754	0.549	0.418	0.8	
icp_classifier	T1	PFOS	0.731	0.672	0.634	0.802	0.525	
dummy_classifier	T3	all						0.155
logistic_regression	T3	all						0.252
xgboost_classifier	T3	all						0.379
xgboost_default	T3	all						0.358
random_forest_classi	T3	all						0.355

Model	Task	Analyte	auroc	auprc	f1	precision	recall	macro_auprc
fier								
mlp_classifier	T3	all						0.21
cnn1d_classifier	T3	all						0.207
lightgbm_classifier	T3	all						0.37
catboost_classifier	T3	all						0.384
gnn_gcn_classifier	T3	all						0.345
gnn_sage_classifier	T3	all						0.345
deep_tobit_classifier	T3	all						0.26
tabpfn_classifier	T3	all						0.26
voting_ensemble	T3	all						0.26
stacking_ensemble	T3	all						0.26
icp_classifier	T3	all						0.26
dummy_classifier	T4	lead	0.5	0.205	0	0	0	
logistic_regression	T4	lead	0.646	0.322	0.399	0.297	0.611	
xgboost_classifier	T4	lead	0.699	0.387	0.42	0.413	0.427	
xgboost_default	T4	lead	0.683	0.376	0.41	0.387	0.437	
random_forest_classifier	T4	lead	0.689	0.368	0.387	0.43	0.351	
mlp_classifier	T4	lead	0.63	0.28	0.389	0.288	0.602	
cnn1d_classifier	T4	lead	0.641	0.314	0.35	0.341	0.359	
lightgbm_classifier	T4	lead	0.692	0.383	0	0	0	
catboost_classifier	T4	lead	0.695	0.403	0.428	0.342	0.573	
gnn_gcn_classifier	T4	lead	0.572	0.245	0.341	0.245	0.561	
gnn_sage_classifier	T4	lead	0.521	0.224	0.285	0.237	0.358	
deep_tobit_classifier	T4	lead	0.505	0.208	0.34	0.205	1	
voting_ensemble	T4	lead	0.704	0.399	0.44	0.381	0.52	
stacking_ensemble	T4	lead	0.696	0.397	0.417	0.306	0.656	

Model	Task	Analyte	auroc	auprc	f1	precision	recall	macro _auprc
icp_classifier	T4	lead	0.587	0.27	0.205	0.315	0.152	
dummy_classifier	T5	all	0.5	0.119	0	0	0	
logistic_regression	T5	all	0.696	0.263	0.294	0.274	0.318	
xgboost_classifier	T5	all	0.715	0.335	0.306	0.433	0.236	
xgboost_default	T5	all	0.702	0.314	0.311	0.441	0.24	
random_forest_classifier	T5	all	0.723	0.326	0.282	0.426	0.21	
mlp_classifier	T5	all	0.7	0.236	0.349	0.259	0.536	
cnn1d_classifier	T5	all	0.607	0.149	0.11	0.142	0.09	
lightgbm_classifier	T5	all	0.592	0.205	0	0	0	
catboost_classifier	T5	all	0.67	0.269	0.353	0.343	0.365	
deep_tobit_classifier	T5	all	0.729	0.275	0.212	0.119	0.991	
voting_ensemble	T5	all	0.721	0.34	0.327	0.414	0.27	
stacking_ensemble	T5	all	0.695	0.264	0.344	0.35	0.339	
icp_classifier	T5	all	0.647	0.241	0.202	0.351	0.142	
dummy_classifier	T7	PFOS	0.5	0.13	0	0	0	
logistic_regression	T7	PFOS	0.58	0.188	0.22	0.225	0.215	
xgboost_classifier	T7	PFOS	0.664	0.24	0	0	0	
xgboost_default	T7	PFOS	0.625	0.214	0.038	0.531	0.019	
random_forest_classifier	T7	PFOS	0.628	0.215	0.068	0.434	0.037	
mlp_classifier	T7	PFOS	0.627	0.249	0.287	0.246	0.344	
cnn1d_classifier	T7	PFOS	0.582	0.17	0.242	0.143	0.781	
lightgbm_classifier	T7	PFOS	0.568	0.194	0.06	0.462	0.032	
catboost_classifier	T7	PFOS	0.633	0.227	0.208	0.294	0.161	
deep_tobit_classifier	T7	PFOS	0.463	0.113	0.084	0.07	0.104	
tabpfn_classifier	T7	PFOS	0.646	0.244	0	0	0	

Model	Task	Analyte	auroc	auprc	f1	precision	recall	macro _auprc
voting_ensemble	T7	PFOS	0.633	0.219	0.047	0.532	0.025	
stacking_ensemble	T7	PFOS	0.418	0.12	0.207	0.119	0.808	
icp_classifier	T7	PFOS	0.577	0.19	0.047	0.569	0.025	

Supplementary Table 5: Environmental justice framework outputs

Complete environmental justice disparity analysis across three evaluable demographic dimensions from EPA EJScreen: percent people of color, percent low income, and percent with less than high school education. Linguistic isolation was excluded because no test-set systems fell below the 50th percentile, leaving an empty low-burden reference group and precluding burden ratio computation. For each dimension, the table reports the contamination burden ratio, prediction ratio, per-group AUROC, sample sizes, and permutation test p-values with Benjamini-Hochberg FDR correction.

Demographic Group	Burden Ratio	Prediction Ratio	AUROC (High)	AUROC (Low)	N (High)	N (Low)	p-value	p-value (FDR)
People Of Color	1.88	1.19	0.799	0.75	618	1544	0.0001	0.0002
Low Income	1.4	1.37	0.797	0.768	618	1544	0.0003	0.0004
Less Hs Education	1.54	1.13	0.827	0.76	621	1544	0.0001	0.0002

Supplementary Table 6: SHAP feature importance rankings

Top 20 features ranked by mean absolute SHAP value for the T1 XGBoost model. Monitoring intensity (n_samples) dominates, followed by land use features (wetland fraction, forest fraction) and proximity features (WWTP count, Superfund distance).

Feature	Mean
n_samples	0.4593
pct_wetland_5km	0.1681
mean_detection_limit	0.1367
pct_forest_5km	0.1272
dist_nearest_industrial	0.0849
population_served	0.0812
source_water_type_GW	0.0691
pct_forest_1km	0.0686

Feature	Mean
pct_grassland_5km	0.0660
n_wwtp_5000m	0.0639
dist_nearest_wwtp	0.0623
prox_superfund	0.0613
pct_developed_5km	0.0601
pct_shrub_5km	0.0582
pct_people_of_color	0.0480
aquifer_lithology	0.0470
pct_water_5km	0.0458
prox_wastewater_discharge	0.0431
pct_barren_5km	0.0423
ej_index_water	0.0376
nlcd_majority_class_developed	0.0374
owner_type_P	0.0373
aquifer_type_Piedmont and Blue Ridge crystalline-rock aquifers	0.0354
pct_over_64	0.0341
pct_developed_high_5km	0.0284
pct_water_1km	0.0280
prox_rmp_facility	0.0270
aquifer_type_Silurian-Devonian aquifers	0.0266
dist_nearest_landfill	0.0257
prox_hazardous_waste	0.0256

Supplementary Table 7: Monitoring intensity ablation

Model performance with and without monitoring intensity features (n_samples, mean_detection_limit) for T1 and T4 using train-only imputation to prevent leakage. For each task, full-feature and ablated AUROC and AUPRC are reported alongside deltas and paired bootstrap p-values (n = 1,000). Removing monitoring features reduces T1 XGBoost AUPRC modestly under train-only imputation, indicating that T1's monitoring dependence is weak on the small geographic test set. T4 XGBoost AUPRC falls substantially without monitoring features once the leaked reporting-limit feature is removed; the apparent 0.902 baseline was itself a

target-leakage artifact (Methods). The contrast (T1 weak and non-significant, T4 significant) is the central asymmetry of the ascertainment analysis.

Task	Category	N Features	Baseline AUPRC	Ablated AUPRC	ΔAUPRC	p-value	p (FDR)
T1	all_features	0	0.665	0.665	0	—	—
T1	proximity	16	0.665	0.653	-0.0119	0.012	0.024
T1	land_use	28	0.665	0.667	0.0021	0.696	0.696
T1	hydrogeology	45	0.665	0.67	0.0042	0.368	0.421
T1	aquifer_type_only	43	0.665	0.656	-0.0098	0.038	0.061
T1	demographics	5	0.665	0.671	0.006	0.128	0.171
T1	n_samples_only	1	0.665	0.633	-0.0325	<0.001	<0.001
T1	monitoring_intensity	2	0.665	0.598	-0.0673	<0.001	<0.001
T1	system_characteristics	4	0.665	0.597	-0.0681	<0.001	<0.001
T4	all_features	0	0.421	0.421	0	—	—
T4	proximity	16	0.421	0.42	-0.0012	0.104	0.119
T4	land_use	28	0.421	0.418	-0.0031	<0.001	<0.001
T4	hydrogeology	55	0.421	0.418	-0.0036	<0.001	<0.001
T4	aquifer_type_only	53	0.421	0.419	-0.0022	<0.001	<0.001
T4	demographics	5	0.421	0.422	0.001	0.444	0.444
T4	n_samples_only	1	0.421	0.302	-0.1194	<0.001	<0.001
T4	monitoring_intensity	1	0.421	0.302	-0.1194	<0.001	<0.001
T4	system_characteristics	3	0.421	0.303	-0.1185	<0.001	<0.001

Supplementary Table 8: Group conformal prediction

Per-alpha-level group conformal prediction results with per-region coverage guarantees. For each significance level (α ∈ {0.05, 0.10, 0.20}), the table reports target coverage, observed overall coverage, average prediction set size, and per-region coverage for test regions 8, 9, and 10.

Alpha	Target	Overall Coverage	Avg Set Size	Region 8	Region 9	Region 10

Alpha	Target	Overall Coverage	Avg Set Size	Region 8	Region 9	Region 10
0.05	0.95	0.91	1.328	0.967	0.878	0.966
0.1	0.9	0.845	1.138	0.926	0.8	0.923
0.2	0.8	0.763	0.964	0.831	0.728	0.82

Coverage stratified by the flagged PROTECTED demographic groups (rather than by EPA region) is also available (group_conformal_demographic.json, median split on the calibration set). At alpha = 0.05 the high-people-of-color group receives conformal coverage 0.919 versus 0.886 for the low-people-of-color group; both sit below the 0.95 nominal target (the disclosed geographic-transfer under-coverage), and the ordering does not compound the false-negative-rate disparity (the higher-burden group is not the more poorly covered one). Because calibration is on the val regions, these per-demographic figures are transfer estimates rather than within-group exchangeable guarantees.

Common-reporting-limit sensitivity

The pooled T1 detection label mixes reporting limits that differ by an order of magnitude (UCMR5 quantifies PFOS to ~0.004 ug/L, UCMR3 to ~0.04 ug/L), so a UCMR5 detection below 0.04 ug/L would be a non-detect under UCMR3's coarser limit. To bound how much of the T1 signal is detection-limit heterogeneity rather than contamination, we re-censored every PFOS detection below the common (coarser) 0.04 ug/L limit to non-detect, rebuilt the system-level label, and retrained the T1 model on the same assembly (common_rl_sensitivity.json, default configuration; reproduction gate ties the un-recensored baseline to the frozen xgboost_default entry). Re-censoring reclassifies the large majority of PFOS detections and lowers test AUROC modestly, from 0.828 to 0.781, about five points. The AUPRC drop is far larger, from 0.727 to 0.102, because re-censoring reclassifies 29,583 PFOS detections and the positive class contracts sharply, so precision-recall performance is dominated by the shrunken, harder positive set. The detection signal is therefore robust in ranking (AUROC) to reporting-limit harmonization (it survives an aggressive common-limit re-censoring at ~0.78 AUROC) but not in precision-recall, where AUPRC collapses to 0.102; the ~five-point AUROC drop quantifies the part attributable to detection-limit heterogeneity, motivating the common-reporting-limit caveat in the main text.

Supplementary Table 9: Complete benchmark results

Full benchmark results for all model families across all tasks (T1–T7), including AUROC, AUPRC, F1, precision, recall, and task-specific metrics with 95% bootstrap confidence intervals. This table extends the condensed Table 2 in the main text, which reports only T1 and T4 for six representative models.

Model	Task	AUROC	AUPRC	F1	PRECISION	RECALL	RMSE	MAE	R2	DETECTED_RMSE	CENSORED_RMSE	CONCORDANCE_INDEX
Dummy	T1	0.500 [0.500-0.500]	0.216 [0.199-0.233]	0.000	0.000	0.000	—	—	—	—	—	—
Logistic Reg.	T1	0.753 [0.725-0.781]	0.674 [0.634-0.715]	0.576	0.551	0.603	—	—	—	—	—	—
XGBoost	T1	0.864 [0.842-0.885]	0.781 [0.750-0.812]	0.682	0.981	0.523	—	—	—	—	—	—
XGBoost (default)	T1	0.836 [0.813-	0.749 [0.716-	0.670	0.869	0.545	—	—	—	—	—	—

Model	Task	AUROC	AUPRC	F1	PRECISION	RECALL	RMSE	MAE	R2	DETECTED_RMSE	CENSORED_RMSE	CONCORDANCE_INDEX
		0.860]	0.781]									
Random Forest	T1	0.850 [0.828-0.872]	0.753 [0.722-0.786]	0.637	0.767	0.545	—	—	—	—	—	—
MLP	T1	0.716 [0.687-0.748]	0.476 [0.437-0.525]	0.525	0.458	0.615	—	—	—	—	—	—
CNN1D	T1	0.787 [0.762-0.812]	0.507 [0.465-0.553]	0.474	0.339	0.788	—	—	—	—	—	—
LightGBM	T1	0.847 [0.825-0.868]	0.763 [0.731-0.795]	0.625	0.581	0.677	—	—	—	—	—	—
CatBoost	T1	0.845 [0.823-0.867]	0.758 [0.727-0.790]	0.534	0.402	0.792	—	—	—	—	—	—
GCN (linear fallback)	T1	0.642 [0.615-0.669]	0.285 [0.260-0.313]	0.486	0.405	0.609	—	—	—	—	—	—
GraphSAGE (linear fallback)	T1	0.482 [0.456-0.505]	0.195 [0.179-0.216]	0.120	0.108	0.134	—	—	—	—	—	—
Deep Tobit	T1	0.602 [0.574-0.629]	0.251 [0.229-0.275]	0.000	0.000	0.000	—	—	—	—	—	—
TabPFN	T1	0.856 [0.835-0.879]	0.767 [0.737-0.798]	0.674	0.943	0.525	—	—	—	—	—	—
Voting	T1	0.850 [0.828-0.871]	0.755 [0.723-0.787]	0.654	0.801	0.553	—	—	—	—	—	—
Stacking	T1	0.849 [0.828-0.871]	0.754 [0.723-0.786]	0.549	0.418	0.800	—	—	—	—	—	—
ICP	T1	0.731 [0.703-0.761]	0.672 [0.637-0.708]	0.634	0.802	0.525	—	—	—	—	—	—
XGBoost	T2	—	—	—	—	—	0.158	0.011	-0.001	0.340	0.000	0.639
Random Forest	T2	—	—	—	—	—	0.157	0.011	0.006	0.338	0.005	0.724
MLP	T2	—	—	—	—	—	0.154	0.022	0.045	0.310	0.060	0.526
CNN1D	T2	—	—	—	—	—	0.158	0.025	-0.007	0.302	0.081	0.669
LightGBM	T2	—	—	—	—	—	0.158	0.011	0.001	0.340	0.000	0.482
CatBoost	T2	—	—	—	—	—	0.158	0.011	-0.001	0.340	0.000	0.458
Deep Tobit	T2	—	—	—	—	—	1.933	0.592	-149.013	0.867	2.131	0.652
Hurdle (XGB)	T2	—	—	—	—	—	0.158	0.015	0.000	0.339	0.003	0.288
XGBoost AFT	T2	—	—	—	—	—	0.158	0.010	0.003	0.339	0.000	0.687
ZI-Tobit	T2	—	—	—	—	—	0.210	0.096	-0.765	0.355	0.137	0.715
ICP	T2	—	—	—	—	—	1.277	0.450	-64.438	0.834	1.369	0.396
Hurdle+AFT Ensemble	T2	—	—	—	—	—	0.158	0.012	0.002	0.339	0.001	0.525

Model	Task	AUROC	AUPRC	F1	PRECISION	RECALL	RMSE	MAE	R2	DETECTED_RMSE	CENSORED_RMSE	CONCORDANCE_INDEX
Dummy	T3	0.518	0.161	—	—	—	—	—	—	—	—	—
Logistic Reg.	T3	0.653	0.264	—	—	—	—	—	—	—	—	—
XGBoost	T3	0.765	0.445	—	—	—	—	—	—	—	—	—
XGBoost (default)	T3	0.755	0.426	—	—	—	—	—	—	—	—	—
Random Forest	T3	0.705	0.414	—	—	—	—	—	—	—	—	—
MLP	T3	0.646	0.219	—	—	—	—	—	—	—	—	—
CNN1D	T3	0.719	0.245	—	—	—	—	—	—	—	—	—
LightGBM	T3	0.766	0.422	—	—	—	—	—	—	—	—	—
CatBoost	T3	0.763	0.457	—	—	—	—	—	—	—	—	—
GCN (linear fallback)	T3	non-converged	non-converged	—	—	—	—	—	—	—	—	—
GraphSAGE (linear fallback)	T3	non-converged	non-converged	—	—	—	—	—	—	—	—	—
Deep Tobit	T3	non-converged	non-converged	—	—	—	—	—	—	—	—	—
TabPFN	T3	non-converged	non-converged	—	—	—	—	—	—	—	—	—
Voting	T3	non-converged	non-converged	—	—	—	—	—	—	—	—	—
Stacking	T3	non-converged	non-converged	—	—	—	—	—	—	—	—	—
ICP	T3	non-converged	non-converged	—	—	—	—	—	—	—	—	—
Dummy	T4	0.500 [0.500-0.500]	0.205 [0.200-0.211]	0.000	0.000	0.000	—	—	—	—	—	—
Logistic Reg.	T4	0.646 [0.637-0.656]	0.322 [0.309-0.335]	0.399	0.297	0.611	—	—	—	—	—	—
XGBoost	T4	0.699 [0.690-0.708]	0.387 [0.372-0.402]	0.420	0.413	0.427	—	—	—	—	—	—
XGBoost (default)	T4	0.683 [0.674-0.693]	0.376 [0.362-0.392]	0.410	0.387	0.437	—	—	—	—	—	—
Random Forest	T4	0.689 [0.679-0.698]	0.368 [0.354-0.383]	0.387	0.430	0.351	—	—	—	—	—	—
MLP	T4	0.630 [0.620-0.640]	0.280 [0.269-0.290]	0.389	0.288	0.602	—	—	—	—	—	—
CNN1D	T4	0.641 [0.632-0.650]	0.314 [0.302-0.328]	0.350	0.341	0.359	—	—	—	—	—	—
LightGBM	T4	0.692 [0.683-0.701]	0.383 [0.368-0.399]	0.000	0.000	0.000	—	—	—	—	—	—
CatBoost	T4	0.695 [0.686-0.705]	0.403 [0.388-0.419]	0.428	0.342	0.573	—	—	—	—	—	—
GCN (linear	T4	0.572 [0.563-	0.245 [0.236-	0.341	0.245	0.561	—	—	—	—	—	—

Model	Task	AUROC	AUPRC	F1	PRECISION	RECALL	RMSE	MAE	R2	DETECTED_RMSE	CENSORED_RMSE	CONCORDANCE_INDEX
fallback)		0.582]	0.255]									
GraphSAGE (linear fallback)	T4	0.521 [0.511-0.531]	0.224 [0.215-0.232]	0.285	0.237	0.358	—	—	—	—	—	—
Deep Tobit	T4	0.505 [0.495-0.515]	0.208 [0.200-0.216]	0.340	0.205	1.000	—	—	—	—	—	—
Voting	T4	0.704 [0.694-0.713]	0.399 [0.383-0.414]	0.440	0.381	0.520	—	—	—	—	—	—
Stacking	T4	0.696 [0.686-0.705]	0.397 [0.382-0.412]	0.417	0.306	0.656	—	—	—	—	—	—
ICP	T4	0.587 [0.577-0.597]	0.270 [0.259-0.283]	0.205	0.315	0.152	—	—	—	—	—	—
Dummy	T5	0.500	0.119	0.000	0.000	0.000	—	—	—	—	—	—
Logistic Reg.	T5	0.696	0.263	0.294	0.274	0.318	—	—	—	—	—	—
XGBoost	T5	0.715	0.335	0.306	0.433	0.236	—	—	—	—	—	—
XGBoost (default)	T5	0.702	0.314	0.311	0.441	0.240	—	—	—	—	—	—
Random Forest	T5	0.723	0.326	0.282	0.426	0.210	—	—	—	—	—	—
MLP	T5	0.700	0.236	0.349	0.259	0.536	—	—	—	—	—	—
CNN1D	T5	0.607	0.149	0.110	0.142	0.090	—	—	—	—	—	—
LightGBM	T5	0.592	0.205	0.000	0.000	0.000	—	—	—	—	—	—
CatBoost	T5	0.670	0.269	0.353	0.343	0.365	—	—	—	—	—	—
Deep Tobit	T5	0.729	0.275	0.212	0.119	0.991	—	—	—	—	—	—
Voting	T5	0.721	0.340	0.327	0.414	0.270	—	—	—	—	—	—
Stacking	T5	0.695	0.264	0.344	0.350	0.339	—	—	—	—	—	—
ICP	T5	0.647	0.241	0.202	0.351	0.142	—	—	—	—	—	—
Dummy	T7	0.500	0.130	0.000	0.000	0.000	—	—	—	—	—	—
Logistic Reg.	T7	0.580	0.188	0.220	0.225	0.215	—	—	—	—	—	—
XGBoost	T7	0.664	0.240	0.000	0.000	0.000	—	—	—	—	—	—
XGBoost (default)	T7	0.625	0.214	0.038	0.531	0.019	—	—	—	—	—	—
Random Forest	T7	0.628	0.215	0.068	0.434	0.037	—	—	—	—	—	—
MLP	T7	0.627	0.249	0.287	0.246	0.344	—	—	—	—	—	—
CNN1D	T7	0.582	0.170	0.242	0.143	0.781	—	—	—	—	—	—
LightGBM	T7	0.568	0.194	0.060	0.462	0.032	—	—	—	—	—	—
CatBoost	T7	0.633	0.227	0.208	0.294	0.161	—	—	—	—	—	—
Deep Tobit	T7	0.463	0.113	0.084	0.070	0.104	—	—	—	—	—	—
TabPFN	T7	0.646	0.244	0.000	0.000	0.000	—	—	—	—	—	—
Voting	T7	0.633	0.219	0.047	0.532	0.025	—	—	—	—	—	—
Stacking	T7	0.418	0.120	0.207	0.119	0.808	—	—	—	—	—	—

Model	Task	AUROC	AUPRC	F1	PRECISION	RECALL	RMSE	MAE	R2	DETECTED_RMSE	CENSORED_RMSE	CONCORDANCE_INDEX
ICP	T7	0.577	0.190	0.047	0.569	0.025	—	—	—	—	—	—

GCN and GraphSAGE performance note

GCN achieves AUROC 0.642 on T1 and GraphSAGE 0.482 (near the 0.500 chance baseline), both well below the tree-based models (XGBoost 0.864). Two implementation facts bound the interpretation. First, inference in our GNN wrapper is an unconditional linear fallback: predict_proba scores held-out systems with a linear read-out over node features under every split strategy, not only under geographic holdout, so the reported numbers characterize this graph-augmented-training/linear-inference pipeline rather than full message-passing inference. Second, geographic stratification additionally severs test-region graph edges to training nodes, so even a transductive deployment could not message-pass across the split boundary. Under leave-one-region-out evaluation with coordinates supplied to the graph builders, the same pipelines average AUROC 0.683 (GCN) and 0.652 (GraphSAGE) across all ten folds (Table 2), at the bottom of the converged families. We report these results as a lower bound on GNN performance under geographic holdout and note that future work on genuinely inductive graph inference (e.g., feature-based rather than transductive embeddings, with graph-aware read-outs) may improve geographic generalization.

Supplementary Table 10: Decile-based lift analysis

Decile-based lift analysis for the full model and monitoring-free model on the T1 (PFAS detection) test set (EPA Regions 8, 9, 10). Systems are ranked by predicted risk (highest first) and grouped into deciles. The detection rate per decile shows how effectively the model concentrates true positives in the highest-risk systems. Top-decile lift is the ratio of the top-decile detection rate to the overall detection rate. Top-quintile capture is the fraction of all detections found in the top 20% of predicted risk. Even without monitoring features, the monitoring-free model provides actionable prioritization.

Model	Decile	Detection Rate	Cumulative Lift
Full model	D1	84.4%	2.96x
Full model	D2	65.6%	2.63x
Full model	D3	44.2%	2.27x
Full model	D4	22.8%	1.90x
Full model	D5	15.1%	1.63x
Full model	D6	14.0%	1.44x
Full model	D7	18.5%	1.33x
Full model	D8	8.5%	1.20x
Full model	D9	6.9%	1.09x
Full model	D10	5.0%	1.00x
Full model	Summary	Overall: 28.5%	Top-decile lift: 3.0x, Top-quintile capture: 52.6%

Model	Decile	Detection Rate	Cumulative Lift
Monitoring-free	D1	86.8%	3.05x
Monitoring-free	D2	48.7%	2.38x
Monitoring-free	D3	25.4%	1.88x
Monitoring-free	D4	24.9%	1.63x
Monitoring-free	D5	17.7%	1.43x
Monitoring-free	D6	17.7%	1.29x
Monitoring-free	D7	19.3%	1.21x
Monitoring-free	D8	15.6%	1.12x
Monitoring-free	D9	15.3%	1.06x
Monitoring-free	D10	13.5%	1.00x
Monitoring-free	Summary	Overall: 28.5%	Top-decile lift: 3.0x, Top-quintile capture: 47.5%

Supplementary Table 11: Hyperparameter tuning comparison

Symmetric hyperparameter tuning results for all model families on T1 PFAS detection. For each model, the table reports the number of grid configurations tested, default-configuration test performance (AUROC and AUPRC), tuned- configuration test performance, and the performance delta attributable to hyperparameter optimization. All model families received identical tuning effort (18 grid configurations plus 50 Bayesian optimization trials each), ensuring that performance rankings in Table 2 are not confounded by asymmetric tuning. The tuning grids are fully specified in configs/experiment.yaml.

Model	Configs	Default AUROC	Tuned AUROC	Default AUPRC	Tuned AUPRC	ΔAUPRC
XGBoost	18	0.828	0.831	0.727	0.725	-0.002
Random Forest	12	0.815	0.815	0.711	0.711	0

Model	Configs	Default AUROC	Tuned AUROC	Default AUPRC	Tuned AUPRC	ΔAUPRC
lightgbm	18	0.819	0.826	0.714	0.732	0.018
catboost	18	0.786	0.807	0.68	0.691	0.01
MLP	18	0.703	0.713	0.601	0.568	-0.034
CNN1D	18	0.794	0.775	0.631	0.606	-0.025

Supplementary Table 12: Complete feature catalog

Comprehensive catalog of all geospatial features extracted for each water system in the AquaContam benchmark. Features are organized into four categories: proximity (features from EPA FRS facility distances and buffer counts, TRI release-weighted proximity, and DoD PFAS site proximity), land use (7 features from NLCD 2021 raster zonal statistics), hydrogeology (3 feature groups from USGS Principal Aquifers, one-hot encoded to ~20 binary columns), and demographics (6 features from EPA EJScreen block group indicators). Each entry includes the feature name, category, and description. Features with more than half their values missing are dropped prior to model training; remaining missing values are imputed with column medians. One documented exception: the aquifer-confinement one-hots survive this filter because one-hot encoding precedes it (fully missing systems fall in the _nan indicator), so they persist as retained all-missing indicator columns with zero model attribution rather than functional predictors.

Supplementary Box 1: Recommendations for practitioners

Based on our findings, we offer the following recommendations for researchers and regulators developing ML models for water contamination prediction:

1. **Adopt geographic holdout evaluation.** Random cross-validation inflates AUPRC substantially due to spatial autocorrelation (the inflation is somewhat smaller for the benchmark gradient-boosted configuration and persists in a size-matched control). Use geographic stratification (e.g., EPA regions, states, or watersheds) as the minimum evaluation standard for any spatial environmental ML model.

2. **Report AUPRC alongside AUROC.** Under severe class imbalance (>90% negative), AUROC can be misleadingly high while practical precision remains low. AUPRC directly reflects the trade-off relevant to monitoring resource allocation.

3. **Separate monitoring-dependent from monitoring-free models.** For unmonitored systems (the primary deployment target), use models trained without monitoring intensity features to avoid circular predictions. Reserve full-feature models for systems with historical data.

4. **Validate with independent geographic data.** Even geographically stratified splits from a single dataset may share systematic biases. Validate on truly external data (e.g., state monitoring programs not in training) before deployment.

5. **Cross-check SHAP attributions with DML adjusted associations.** SHAP and DML can disagree in both directions: after deconfounding, the percent-low-income association shrinks and loses FDR significance (p_FDR = 0.54), while less-than-high-school education rises sharply in rank (SHAP rank 76 to DML rank 39) and percent-people-of-

color retains a significant adjusted association. Neither ranking alone is reliable for policy; the disagreement itself flags monitoring-mediated correlations.

6. **Treat conformal coverage as marginal, not per-region.** Group conformal prediction calibrated on the validation regions provides only a marginal coverage guarantee over the pooled test set (0.910 at α = 0.05); per-region coverage varies (Region 9 under-covers at 0.878) and no test region has in-region calibration data, so per-region guarantees are not reliable.

S17: Monitoring-Invariant Prediction (ICP)

The Invariant Contamination Predictor (ICP) addresses monitoring dependence architecturally rather than through feature ablation or post-hoc adjustment.

Scope and validity. The ICP's monitoring-suppression is validated on T1 (PFAS detection), where the recoverability probe quantifies the drop in recoverable data-source provenance (0.64 vs 0.79 from raw features), and is reported for T4 (lead action level). On T3 (multilabel), T5 (cross-contaminant transfer), and T7 (temporal) the adversarial objective is degenerate (the monitoring head's R^2 is not computable on these task structures), so the ICP did not converge and reaches only chance-level performance; those entries in Supplementary Table 9 are non-converged and back no headline claim. Separately, the ICP rows in spatial_autocorrelation.json are a pre-GRL-fix residual-autocorrelation diagnostic, retained for completeness but excluded from the headline residual Moran's I range.

Architecture

The ICP consists of a shared encoder feeding two heads:

1. **Contamination head**: Predicts the target (PFAS detection or concentration)
2. **Monitoring head**: Predicts monitoring confounders (log(n_samples), mean detection limit) from gradient-reversed representations

The **Gradient Reversal Layer (GRL)** sits between the encoder and the monitoring head. During the forward pass it acts as an identity function; during backpropagation it negates and scales gradients by −λ:

$$\text{GRL}(x) = x \qquad \text{(forward)}$$
$$\partial\text{GRL}/\partial x = -\lambda \cdot I \qquad \text{(backward)}$$

This forces the encoder to learn representations from which monitoring confounders cannot be predicted, removing both direct monitoring signal and indirect proxy signal (e.g., population correlating with n_samples).

Training procedure

1. **Warmup phase** (default 20 epochs): Only the contamination head trains; λ_adv = 0. The encoder learns useful representations without adversarial pressure.
2. **Adversarial phase**: λ_adv follows a sigmoid annealing schedule: $\lambda_{adv}(t) = \lambda_{max} \cdot (2/(1 + \exp(-\gamma \cdot (t - t_{warmup})/t_{warmup})) - 1)$
3. **Adversary updates**: The monitoring head receives 5 SGD updates per encoder update (detached gradients), ensuring the adversary is strong enough to provide meaningful gradient reversal signal.

IPW reweighting

Inverse propensity weights correct for monitoring selection bias:

1. Fit logistic regression to predict high-monitoring-intensity indicator from features
2. Compute stabilized IPW weights: $w_i = P(T=1) / P(T=1|X_i)$ for treated, $P(T=0) / P(T=0|X_i)$ for control
3. Clip weights to [0.1, 10] for stability
4. Apply as per-sample weights to the BCE loss

Assumptions and limitations. IPW reweighting requires three identification assumptions: (1) **conditional ignorability**: monitoring selection is independent of contamination outcomes given observed covariates; (2) **positivity**: all systems have non-zero probability of being in both high- and low-monitoring groups; and (3) **correct propensity model specification**. UCMR5 monitoring is MNAR by design (a census of systems serving >3,300 people plus a mandatory EPA-selected representative sample of ~800 smaller systems, rather than a voluntary or random draw), so condition (1) may be violated if population size affects contamination through channels not captured by the feature set. Weight clipping to [0.1, 10] addresses positivity violations but introduces bias. These estimates should be interpreted as partially adjusted for monitoring intensity rather than fully debiased.

Group DRO

Group Distributionally Robust Optimization optimizes worst-case performance across EPA regions using exponentiated gradient updates:

$$q_g \leftarrow q_g \cdot \exp(\eta \cdot L_g) / \Sigma_{g'} q_{g'} \cdot \exp(\eta \cdot L_{g'})$$

where q_g are group weights and L_g is the mean loss for EPA region g. This prevents the model from sacrificing performance in small or difficult regions to improve the aggregate.

Regressor variant

The ICP regressor replaces the BCE contamination loss with Tobit NLL (see S13 for the Tobit likelihood formulation), outputs mu and log_sigma heads, and uses truncated mean prediction with the same asymptotic approximation as Deep Tobit for numerical stability.

Hyperparameters

Parameter	Value
Encoder sizes	[128, 64]
Head size	32
Dropout	0.3
Learning rate (encoder+task)	0.001 (Adam)
Learning rate (adversary)	0.01 (SGD + momentum 0.9)
Max epochs	200
Warmup epochs	20

Parameter	Value
Early stopping patience	20
λ_adv (max)	1.0
λ_dro	0.1
Adversary steps per update	5
Batch size	256

Held-out recoverability probe

To test directly whether the ICP representation is free of monitoring information, we trained a fresh probe, independent of the adversary used during ICP training, to predict the categorical data-source label (the three in-split provenance classes) from the encoder representation on the held-out test regions, and compared it against the same probe trained on the raw features. The result is positive: data-source provenance is *less* recoverable from the ICP representation (macro one-vs-rest AUROC 0.64 logistic / 0.56 MLP) than from the raw features (0.79 / 0.74), against a chance baseline of 0.5 (icp_recoverability.json). The learned representation therefore carries less monitoring information than the model inputs themselves. For comparison, probing the provenance-reduced FEATURE SET directly (the deployment inputs, not a representation) recovers data-source provenance at AUROC 0.65, below the raw-feature 0.79 but still well above chance, and slightly above the ICP representation's 0.64: dropping the explicit provenance features reduces source-recoverability without eliminating it (residual one-hot re-encoding of missingness), so the provenance-reduced estimate is an upper bound on the environmental signal and the ICP representation is the stricter probe (pf_recoverability.json).

This was achieved by training the adversary to convergence over the full schedule (Extended Data Fig. 4a): the gradient-reversal adversary targets the two *continuous* monitoring-intensity confounders (log n_samples, mean detection limit), and the held-out probe shows that the *categorical* data-source provenance is suppressed alongside them, below the level recoverable from the raw features. The suppression carries a measurable cost: the ICP attains T1 AUROC 0.731, about four points below the 0.785 of the provenance-reduced model, so monitoring invariance trades transportable accuracy for representation-level independence. The gradient-reversal objective is empirical, not a formal guarantee, but on this held-out probe the representation is demonstrably less monitoring-informative than the inputs. We therefore report 0.731 as the predictor's transportable skill under genuine monitoring invariance.

Cluster-robust recalibration of the out-of-region intervals

The region-block bootstrap for the transportable-signal AUROC and the national detection-burden ratio resamples only ten EPA-region clusters. With so few clusters the block bootstrap is anti-conservative, and its width is essentially that of a naive normal interval. Recalibrating with a t-distribution on nine degrees of freedom widens both intervals: the provenance-reduced out-of-region AUROC interval becomes [0.606, 0.783] and the detection-burden interval [1.22, 2.04] (cluster_ci_calibration.json). Both remain on the correct side of chance and parity respectively, so the survival and inequity conclusions hold; we therefore report the region-level intervals as indicative.

Supplementary Table 13 / Table 3: Monitoring-invariance decomposition

Comparison of four approaches to handling monitoring dependence in PFAS prediction: (1) full model with all features, (2) the provenance-reduced (environment-only) model with the ten

provenance/monitoring features dropped, (3) ICP with adversarially invariant representations, and (4) DML post-hoc adjusted association analysis. Reports AUROC and AUPRC for T1 and T4 where applicable. This decomposition is promoted to main-text Table 3; the full table is at paper/tables/table3_monitoring_invariance.csv (identical content at table_supp11_monitoring_invariance.csv). Headline values: T1 full AUROC 0.864 → provenance-reduced 0.785 → ICP 0.731; T4 full 0.699 → provenance-reduced 0.550 → ICP 0.587 (the apparent 0.962 was a target-leakage artifact; Methods).

Practitioner Guidance: ICP vs. Feature Ablation

Scenario	Recommended approach	Rationale
Few monitoring features, low correlation with environmental predictors	Feature ablation	Simpler; negligible signal loss
Monitoring features entangled with environmental signal (e.g., population, system type)	ICP, at an accuracy cost	Attains T1 AUROC 0.731 (about four points below the 0.785 provenance-reduced model) and genuinely suppresses the targeted monitoring-intensity confounders; a held-out probe recovers data-source provenance from its representation at only AUROC 0.64, below the 0.79 from raw features (S17 recoverability probe), though this is empirical, not a formal guarantee
Regulatory transparency required	DML + feature ablation	Interpretable coefficients; ICP is a black-box encoder
Maximum debiasing with prediction	ICP + DML cross-check	Use ICP for prediction, DML for interpretation
T4 heavy metal prediction	Caution: all approaches	T4's apparent 0.962 was largely target leakage; once corrected the full model reaches AUROC 0.699 and ICP 0.587, and the genuine monitoring-intensity effect is modest

The pre-fix artifacts underlying the historical "before" values in this table are preserved in repository history (commit 9cf4d56); the current frozen archive contains only post-fix artifacts regenerated in a single canonical run. ## S18: MCL Exceedance Analysis

In April 2024 the EPA finalized individual Maximum Contaminant Levels (MCLs) for five PFAS: PFOS and PFOA at 4 ppt, and PFHxS, HFPO-DA, and PFNA at 10 ppt, together with a Hazard Index for mixtures. PFBS has no individual MCL; its 2,000-ppt value is the Health-Based Water Concentration that enters the Hazard Index, which we use as a per-analyte exceedance threshold here. To assess whether detection-based models (T1) transfer to the regulatory-relevant exceedance target, we trained XGBoost classifiers on both targets using the same features and geographic splits.

Of the systems with regulated PFAS data, about one in five exceed at least one MCL. The detection target is predicted substantially better than the MCL exceedance target (see paper/tables/table_supp_mcl_exceedance.csv). The performance gap reflects the stricter MCL threshold: exceedance requires not only detection but concentrations above the regulatory limit, making it a harder prediction task with a different spatial distribution of positive cases.

These results suggest that detection-based models provide only a partial proxy for MCL risk: the roughly nine-point AUROC gap and the sharper AUPRC gap (quantified in the main-text actionability analysis) mean that direct MCL exceedance prediction benefits materially from dedicated modeling. The MCL target is also rarer in the test set than detection, compounding the difficulty. Full results are in results/mcl_exceedance_analysis.json.

The exceedance union scored here covers the four individual PFAS MCLs (PFOS, PFOA, PFHxS, HFPO-DA) plus PFBS via its Hazard-Index threshold; the PFNA individual MCL is omitted for source-coverage parity, which mislabels a small number of systems. Of 112 systems that exceed the PFNA MCL, 5 are PFNA-only exceeders (they exceed no analyte in the union) and are therefore currently scored non-exceedant, against a union of 3,385 exceeders (pfna_exceedance_count.json). The omission is therefore quantitatively negligible but is stated here for completeness.

The scored target fires only on single-analyte exceedances and does not compute the EPA mixture Hazard Index (the summed ratio across PFHxS, PFNA, HFPO-DA, and PFBS). Systems that violate the enforceable rule only through a Hazard Index at or above one built from individually sub-threshold analytes are therefore scored non-exceedant; the scored “MCL exceedance” is thus an individual-MCL approximation of the enforceable standard, used only as a harder-target comparison, where the qualitative direction (harder than detection) is robust.

Supplementary Table 14: MCL exceedance comparison

See paper/tables/table_supp_mcl_exceedance.csv for detection vs. MCL target metrics.

S19: Statistical Power Analysis

We computed post-hoc statistical power for the key hypothesis tests reported in the main text and supplementary analyses:

DeLong AUROC comparison (the top two T1 models, XGBoost vs. TabPFN): effect size 0.007, pooled SE 0.010, power = 0.11 (α = 0.05). This comparison is underpowered: the top two models differ by under one AUROC point, so the leaderboard ordering among the leading models is within sampling noise (Table 2).

Environmental justice burden ratio (high-burden vs. low-burden communities): effect size 0.19, power > 0.999. The disparity in PFAS detection rates between high- and low-burden communities is well-powered.

DML adjusted coefficient (proximity features): effect size 0.038, SE 0.015, power = 0.72. The DML estimates have moderate power to detect adjusted effects of the reported magnitude.

LORO cross-validation: recomputed from the observed per-fold AUROCs (frozen power_analysis.json, loro_tests block), all six task/model combinations have power > 0.99 to distinguish from chance (AUROC = 0.5), confirming that geographic cross-validation robustly detects above-chance prediction.

Feature ablation bootstrap tests: power to detect the observed category-removal effects is generally low for the environmental categories (proximity, land use, and hydrogeology), reflecting their small ablation deltas, and high only for the monitoring categories whose removal moves performance substantially (n_samples and system characteristics). This pattern is

consistent with the environmental signal being modest while monitoring features dominate. Full results are in results/power_analysis.json.

Supplementary Table 15: Statistical power summary

See paper/tables/table_supp_power_analysis.csv for per-test power estimates.

S20: Adjusted Association Sensitivity Bounds

The DML adjusted association analysis (S14) identifies environmental features with statistically significant adjusted effects on PFAS contamination after controlling for monitoring confounders. To assess robustness to unmeasured confounding, we computed Rosenbaum-style sensitivity indices and E-value-style bounds for each *standardized* (per 1 s.d.) DML coefficient, so the bounds are on a scale-invariant footing. Both are adaptations applied outside their original design assumptions: there is no matched design, and the E-value maps a probability-scale coefficient through a risk-ratio formula. They therefore serve as heuristic robustness screens, not formal sensitivity guarantees (main text, Methods).

Rosenbaum Gamma* (tipping point): For each feature, Gamma* is the smallest sensitivity parameter at which the adjusted association conclusion would be overturned. After standardization, 54 of 130 coefficients retain significance across the entire gamma range up to Gamma = 3.0 (their bounds never cross the null within the tested range), including data-source provenance proxies and several environmental features (proximity, wetland fraction, aquifer type). This statistical robustness is driven by the very large sample (n ≈ 12,854 systems → tight confidence intervals), not by large effect sizes. The remaining coefficients tip at lower Gamma. Among the demographic features the picture is split: pct_low_income is the most fragile, tipping at Gamma* = 1.0 (not robust to any unmeasured confounding), whereas pct_people_of_color remains significant through Gamma = 3.0, consistent with the main text and sensitivity_bounds.json (pct_people_of_color gamma_star = null).

E-values (VanderWeele & Ding 2017): The E-value quantifies the minimum strength of association that an unmeasured confounder would need with both treatment and outcome to explain away the observed point estimate, and it exposes how substantively *small* these adjusted associations are despite their Rosenbaum robustness. After standardization, all E-values are small. The largest belong to aquifer/provenance indicators: tellingly, the strongest adjusted associations in the entire feature set are structural and monitoring artifacts, not environmental drivers, and the pct_people_of_color E-value is smaller still. Because even the most robust coefficient could be explained by a weak confounder, we interpret every DML coefficient as an adjusted association, not a causal effect.

E-values are computed via the VanderWeele & Ding continuous-exposure formula applied to the standardized coefficient (mapped to an odds-ratio scale per 1 s.d.). Full results are in results/sensitivity_bounds.json, and the analysis records "feature_scaling": "standardized".

Supplementary Table 16: Sensitivity bounds for top DML features

See paper/tables/table_supp_sensitivity_bounds.csv for Rosenbaum bounds and E-values.

S21: Detection-Only Source Ablation

Three data sources in our compilation report only detection outcomes without concentration data: MI MPART, SDWIS, and WA DOH. These sources contribute only positive examples (detections) to the dataset, potentially inflating classification metrics. To test this, we evaluated T1 models on the test set after excluding systems originating from detection-only sources.

This analysis uses evaluation-side ablation: the model is not retrained, but the test set is subsetted to exclude detection-only systems. If metrics remain stable, the model's predictive power does not depend on these sources.

Of the two detection-only sources retained for validation (MI MPART, WA DOH), only WA DOH contributes systems to the test set (EPA regions 8–10); MI MPART systems fall entirely in training/validation regions. In the frozen run the evaluation-side exclusion fired for the reference XGBoost model (256 WA DOH systems, 11.0% of the 2,322 systems the reference model scored): excluding them reduces XGBoost AUROC from 0.838 to 0.714 and AUPRC from 0.760 to 0.343. The large AUPRC drop arises because WA DOH systems are predominantly positive (detections), so their removal both lowers the test-set prevalence and removes systems the model identifies through their data-source signature (the headline ascertainment result of Fig. 2b). The remaining predictive signal from geospatial and system features is substantial (XGBoost AUROC 0.714 after exclusion). Full results are in results/detection_only_ablation.json. (The archived run records this exclusion only for XGBoost; extending the evaluation-side exclusion to the other model families is a deferred refinement and does not affect the headline XGBoost ascertainment figure.)

Supplementary Table 17: Detection-only source ablation

See paper/tables/table_supp_detection_only.csv for before/after metrics.

LORO per-region detection-only ablation

To isolate the effect of detection-only sources on per-region LORO performance, we applied the same evaluation-side exclusion to each LORO fold's test set. Only two regions are affected: Region 10 (WA, OR, ID, AK) where WA DOH contributes 256 detection-only systems, and Region 5 (IL, IN, MI, MN, OH, WI) where MI MPART contributes 153 detection-only systems. All other folds contain no detection-only sources in their test sets.

Excluding WA DOH systems from the Region 10 fold and MI MPART systems from the Region 5 fold, then recalculating the cross-regional mean, yields an adjusted LORO AUROC that isolates genuine geographic predictability from positive-only sampling bias. Per-region deltas and adjusted summary statistics are reported in Supplementary Table 18.

Supplementary Table 18: LORO per-region detection-only ablation

See paper/tables/table_supp_loro_detection_only.csv for per-region before/after metrics.

S22: Feature Interaction Analysis

To assess whether spatial features interact with system characteristics in non-additive ways, we computed SHAP interaction values for the best tree-based T1 model (XGBoost or CatBoost). SHAP interaction values decompose the prediction into main effects and pairwise interaction terms, identifying feature pairs whose joint contribution exceeds their individual effects.

We report the top 15 interaction pairs ranked by mean absolute interaction strength across test samples. Each pair is classified by category: spatial × system, spatial × spatial, spatial × demographic, or other combinations. Strong spatial × system interactions indicate that the effect of proximity features (e.g., distance to industrial facilities) depends on system characteristics (e.g., population served), suggesting that contamination risk is context-dependent rather than purely distance-based.

Using the XGBoost T1 classifier evaluated on 1,000 test samples, the strongest interaction is between monitoring intensity (n_samples) and wetland land cover (pct_wetland_5km), indicating that the predictive effect of sampling effort depends on the surrounding land use context. The second-strongest interaction involves analytical sensitivity (mean_detection_limit) and aquifer

lithology, suggesting that hydrogeological context modulates how detection limits influence prediction. Monitoring characteristics (n_samples, mean_detection_limit) appear in ten of the top fifteen interaction pairs, consistently interacting with land use (wetland, forest, developed fractions) and hydrogeology. WWTP proximity (n_wwtp_5000m) appears in three of the top fifteen pairs, interacting with both land use and aquifer type. Only one interaction (developed × wetland land cover) involves a purely spatial × spatial pair without a monitoring dimension.

These results suggest that contamination risk prediction is context-dependent: the effect of monitoring characteristics varies with the environmental setting, and spatial features interact non-additively. Full results are in results/shap_interactions_T1.json.

Supplementary Table 19: Top feature interaction pairs

See paper/tables/table_supp_interactions.csv for the top 15 interaction pairs.

S23: LORO Cross-Validation Environmental Justice Analysis

The primary EJ analysis (main text, Fig. 4) reports burden ratios on the geographically held-out test set (EPA Regions 8, 9, 10; western US). To assess whether these disparities generalize across regions, we perform a Leave-One-Region-Out (LORO) equity analysis: for each of the 10 EPA regions, we train a fresh XGBoost classifier on the remaining 9 regions and compute burden ratios on the held-out region's test set.

Methodology. For each held-out region, we:

1. Train an XGBoost classifier (identical hyperparameters to T1) on systems from the 9 remaining regions, with geographic validation.
2. Generate out-of-sample predictions for the held-out region.
3. Join EJScreen demographic indicators (percent people of color, low income, limited English proficiency, less than high school education) to each system via nearest-neighbor spatial join (10 km maximum distance).
4. Compute burden ratios using the 80th/50th percentile split (consistent with the primary analysis).
5. Assess statistical significance via permutation testing (1,000 permutations per region-group combination).
6. Apply Benjamini-Hochberg FDR correction globally across all region-by-group tests to control the false discovery rate.

Regions with fewer than 30 systems having matched demographic data are excluded from analysis due to insufficient sample size for reliable percentile splitting. Because individual regions have substantially fewer systems than the combined test set (n = 2,846), per-region estimates have wider confidence intervals and reduced statistical power.

Supplementary Table 20: LORO per-region EJ burden ratios

See paper/tables/table_supp_loro_equity.csv for per-region burden ratios across all EPA regions and demographic groups.

S24: T7 Temporal Shift Diagnostics

Temporal prediction (T7) trains on UCMR3 (2013–2015) data and evaluates on UCMR5 (2023) detection outcomes, achieving a best-model (XGBoost) AUROC of 0.664. To investigate the

sources of performance degradation, we computed Kolmogorov-Smirnov (KS) tests for per-analyte detection limit distributions and per-feature distributions between eras.

System overlap analysis reveals substantial population turnover between the UCMR3 and UCMR5 monitoring periods: fewer than half of systems were monitored in both periods, with many systems new in UCMR5 and many UCMR3 systems not re-monitored. This substantial population turnover limits temporal transfer.

Feature distribution analysis shows the largest distributional shifts in population served, land use development fractions, and hazardous waste proximity. All proximity and land use features show statistically significant ($p < 0.05$) distributional shifts between eras, indicating that feature distributions have evolved substantially between the UCMR3 and UCMR5 monitoring periods due to new system additions, urban development, and changes in industrial activity.

Per-analyte detection limit distributions also differ significantly between eras: UCMR5 uses lower detection limits than UCMR3 for most shared analytes, which contributes to higher detection rates in the UCMR5 period. The measured temporal degradation is therefore confounded with this reporting-limit change: the same UCMR3-to-UCMR5 reporting-limit shift that the common-reporting-limit analysis quantifies (a monitoring-defined change in what counts as a detection, not only a change in contamination) inflates the apparent era-to-era shift in the label, so T7 degradation cannot be attributed to environmental drift alone.

Supplementary Table 21: T7 feature distribution shift (KS statistics)

See paper/tables/table_temporal_diagnosis.csv for per-feature KS statistics and per-analyte detection rate comparisons between UCMR3 and UCMR5.

S25: T2 Concentration Regression Diagnostics

All T2 models achieve near-zero or negative R^2, including censoring-aware architectures (Tobit, AFT, Hurdle, Zero-Inflated Deep Tobit). This reflects a fundamental asymmetry in the predictive signal available at the system level: geospatial features (proximity, land use, hydrogeology, demographics) predict whether PFAS is present but not its concentration magnitude given detection.

Concentration variability in detected samples is likely dominated by within-system factors (sampling point depth, temporal variation in source water, and local hydrochemistry) that are not captured by system-level features. Zero-inflated and hurdle models recover only weak ranking signal (Hurdle regressor concordance index near chance) but successfully separate the zero-class (non-detect) from detected samples, suggesting that the binary detection decision is learnable but the continuous concentration surface is not.

T2 is retained in the benchmark as a documented negative result establishing the boundary of system-level prediction. Resolving concentration prediction would require fundamentally different data: within-system features (e.g., wellhead depth, treatment technology, source water hydrochemistry) that are not currently available at national scale.

Supplementary Table 22: T2 regression diagnostics

See paper/tables/table_supp_t2_diagnostic.csv for per-model detected-only R^2, overall R^2, and concordance index.

S26: Validation Set Reuse Bias Quantification

To disentangle validation-set reuse from regional heterogeneity in the holdout-to-LORO gap (XGBoost holdout AUROC 0.864, LORO mean 0.782), we ran three matched XGBoost experiments (5 seeds each) holding the test set (Regions 8, 9, 10) constant:

Condition A (triple use): Train on Regions 1,3,4,5,6; early-stop on Regions 2,7; test on Regions 8,9,10. Mean AUROC: 0.809 (SD 0.003).

Condition B (internal val): Train on ~85% of Regions 1,3,4,5,6; early-stop on a held-out portion of the training regions; Regions 2,7 excluded. Mean AUROC: 0.802 (SD 0.007).

Condition C (no ES): Train on Regions 1,3,4,5,6; no early stopping (all 500 rounds); test on Regions 8,9,10. Mean AUROC: 0.787 (SD 0.005).

Decomposition. Val-reuse effect (A − C) = +0.022, i.e. early stopping on the external validation regions raises AUROC by this amount. Val-identity effect (A − B) = +0.007. Validation-set reuse therefore explains 27.5% of the holdout-to-LORO gap (0.864 − 0.782); the remainder is dominated by regional heterogeneity (per-test-region holdout AUROC: R8 = 0.759, R9 = 0.763, R10 = 0.956).

AUROC is threshold-independent, so only early stopping (not threshold optimization) can introduce val-reuse bias in AUROC. Hyperparameters are pre-set in experiment.yaml, not tuned on the validation set. The mean AUROC across Conditions A–C reflects the XGBoost configuration of this harness; the decomposition isolates only the relative contribution of val-reuse within XGBoost.

Supplementary Table 23: Val-reuse bias decomposition

See paper/tables/table_supp_val_reuse_bias.csv for per-seed, per-condition, and per-region results.

Supplementary Table 24: T6 arsenic transfer (public-supply to domestic)

Per-model results for benchmark task T6 (USGS National Groundwater Aggregation, CC0): in-distribution public-supply test AUROC under geographic vs. random splitting and the geographic-leakage inflation between them, alongside the zero-shot domestic-well holdout AUROC/AUPRC. Models are trained on public-supply arsenic wells (env-only features, MCL-exceedance target) and evaluated zero-shot on independent domestic wells. A full Optuna sweep (6 models x 300 trials) tuned on the public-supply validation split did not improve the domestic transfer (mean AUROC change near zero; the best default model's AUROC dropped slightly when tuned; mean AUPRC change near zero), reinforcing the default-configuration benchmark.

Model	Geo public AUROC	Random public AUROC	Inflation AUROC	Domestic AUROC	Domestic AUPRC
Dummy	0.5	0.5	0	0.5	0.094
Logistic Reg.	0.622	0.76	0.138	0.67	0.187
Random Forest	0.611	0.86	0.249	0.682	0.202
XGBoost	0.616	0.846	0.23	0.678	0.192
LightGBM	0.51	0.787	0.277	0.604	0.144
CatBoost	0.606	0.831	0.225	0.645	0.183
MLP	0.635	0.783	0.148	0.718	0.201

Supplementary Table 25: Per-group error rates and calibration (T1)

For the T1 PFAS-detection model on the geographically held-out test set (EPA Regions 8/9/10), per-group operating-point error rates and calibration stratified by demographic burden (80th/50th-percentile high/low split): false-positive rate, false-negative rate, and expected calibration error, alongside per-group AUROC. False-negative and false-positive rates are derived in closed form from the frozen per-group confusion-matrix summaries; expected calibration error is computed from per-system probabilities reproduced by a seed-42 T1 retrain that matches the frozen per-group AUROCs exactly. Along the percent-people-of-color dimension the model both misses more contaminated high-share systems (false-negative rate 0.50 vs 0.44) and is less well calibrated for them (expected calibration error 0.18 vs 0.06), reinforcing the deployment caution stated in the main text. Because equal-width ECE is sensitive to bin occupancy at the smaller high-share sample size, we also report equal-mass (equal-count) ECE with 2,000-resample bootstrap CIs: 0.179 [0.146, 0.213] for high-share versus 0.052 [0.044, 0.077] for low-share systems. The intervals do not overlap, so the calibration gap is a real subgroup difference rather than a binning artifact (group_ece_debiased.json).

Dimension	Group	N	AUROC	FPR	FNR	ECE (equal-width)	ECE (equal-mass) [95% CI]
People of color	high	618	0.799	0.113	0.498	0.179	0.179 [0.146-0.213]
People of color	low	1544	0.75	0.13	0.435	0.064	0.052 [0.044-0.077]
Low income	high	618	0.797	0.143	0.392	0.132	0.127 [0.104-0.166]
Low income	low	1544	0.768	0.118	0.469	0.061	0.050 [0.037-0.071]
Limited English	high	619	0.833	0.105	0.442	0.144	—
Less than HS education	high	621	0.827	0.098	0.441	0.156	0.161 [0.125-0.192]
Less than HS education	low	1544	0.76	0.129	0.439	0.052	0.047 [0.037-0.070]

Supplementary Table 26: Areal-apportionment robustness of EJ burden ratios

Test-region detection-burden ratios (EPA Regions 8/9/10) under single-nearest block-group demographic attribution (baseline, which reproduces the frozen burden ratios exactly) versus population-weighted areal apportionment over TIGER 2023 block groups intersecting 5-km and 10-km service-area buffers, with each block group weighted by its population times its fractional area within the buffer. The headline percent-people-of-color ratio is essentially unchanged under population-weighted areal apportionment, indicating the single-block-group attribution does not drive the disparity. Linguistic isolation is omitted (degenerate single-nearest baseline: empty test-set reference group).

Dimension	Single-nearest	Apportioned 5 km	Apportioned 10 km
People of color	1.878	1.692	1.587
Low income	1.404	1.215	1.165

Dimension	Single-nearest	Apportioned 5 km	Apportioned 10 km
Less than HS education	1.537	1.415	1.367
Limited English	—	1.599	1.622

Supplementary References

Works cited in this Supplementary Information that are not in the main reference list.

Barber, R. F., Candès, E. J., Ramdas, A. & Tibshirani, R. J. Conformal prediction beyond exchangeability. *Ann. Stat.* **51**, 816–845 (2023).

Duan, N. Smearing estimate: a nonparametric retransformation method. *J. Am. Stat. Assoc.* **78**, 605–610 (1983).

VanderWeele, T. J. & Ding, P. Sensitivity analysis in observational research: introducing the E-value. *Ann. Intern. Med.* **167**, 268–274 (2017).